

**Investigating the physical mechanisms that impact electric
fields in the atmosphere**

by

Greg M. Lucas

B.S., University of Wisconsin, 2010

M.S., University of Wisconsin, 2010

A thesis submitted to the
Faculty of the Graduate School of the
University of Colorado in partial fulfillment
of the requirements for the degree of
Doctor of Philosophy
Department of Aerospace Engineering Sciences

2017

This thesis entitled:
Investigating the physical mechanisms that impact electric fields in the atmosphere
written by Greg M. Lucas
has been approved for the Department of Aerospace Engineering Sciences

Prof. Jeffrey Thayer

Dr. Wiebke Deierling

Prof. Jeffrey Forbes

Prof. Robert Marshall

Prof. Katja Friedrich

Date _____

The final copy of this thesis has been examined by the signatories, and we find that both the content and the form meet acceptable presentation standards of scholarly work in the above mentioned discipline.

Lucas, Greg M. (Ph.D., Aerospace Engineering)

Investigating the physical mechanisms that impact electric fields in the atmosphere

Thesis directed by Prof. Jeffrey Thayer

The underlying physics and dynamics of the atmosphere drive electric currents and establish electric fields in a phenomenon known as the global electric circuit (GEC). The GEC has been observed and modeled with limiting assumptions and parameterizations in previous research. This thesis describes the incorporation of a physics-based GEC modeling scheme into a sophisticated climate model to describe the evolution of GEC currents, ground-ionosphere potential, electric fields, and conductivity within the atmosphere. Supporting measurements of atmospheric electric fields over time were used to describe the impact of local meteorological changes and assess the GEC contribution to near-surface electric fields.

The source currents within the GEC are generated by a global distribution of electrified clouds. The produced currents lead to a potential difference between the ground and ionosphere. This potential difference produces return currents that are dependent on the global conductivity distribution. Realistic physics and dynamics produced within the climate model are used to generate the conductivity of the atmosphere. The conductivity calculation includes a 3-D spatial and temporal determination of ion production from radon, galactic cosmic rays, and solar proton events and ion losses from recombination, clouds, and aerosols. To validate the model, several data sets from Antarctica and an array of measurements from Kennedy Space Center were utilized. The use of these data sets required new statistical methods to be developed to better understand how local meteorological processes affect electric fields including the wind direction, clouds, and the local sunrise.

Coupling the conductivity and sources together within the model produces new insights into the GEC efficiency of electrical storms. Storms near the equator tend to be strong but inefficient, while storms at mid-latitude are weaker and more efficient. This leads to the global source current

distribution shifting more poleward. The model is also used to simulate changes in the GEC caused by volcanic eruptions and the solar cycle. Although the GEC is global in nature, diurnal, seasonal, and annual variations in electric field measurements from the model are highly location dependent.

Acknowledgements

I appreciate all of the love and support that my family and friends have shown me throughout this process. In particular I'd like to thank my parents Ray and Carol Lucas for instilling in me a desire to continually learn, my aunt and uncle Lisa and Randy Tuomala for inviting me over to their home during holidays, my girlfriend Allison Dean for being a part of so many fun adventures, and the Dean family for inviting me over for so many family meals and events.

I wish to thank my advisor Prof. Jeffrey Thayer for allowing me to be a part of his research group and showing me what it means to be a great advisor and mentor.

I am indebted to all of the time and effort my committee and work colleagues have given me during my studies. The list includes Andreas Baumgaertner, Wiebke Deierling, Robert Marshall, Jeff Forbes, Katja Friedrich, Scott Palo, Art Richmond, Astrid Maute, Wenbin Wang, Victor Pasko, Jaroslav Jánský, and Mike Mills.

Thank you to all my friends who have been a big help in taking my mind away from school when I needed a break. Particularly Mike Croteau, Dimitri Krattiger, Mack Jones, Ryan McGranaghan, Vu Nguyen, Vicki Hsu, Robert Stillwell, Rory Barton-Grimley, Nick Rainville, Alice Bradley, Tevis Nichols, and Roger Laurence III.

This work was supported by NSF Award AGS-1135446 to the University of Colorado under the Frontiers in Earth System Dynamics Program (FESD).

Contents

Chapter

Executive Summary	1	
1	Introduction	4
1.1	Background	5
1.2	Theory	7
1.3	Research Questions	8
2	Meteorological Influences on Observational Data	12
2.1	Instrumentation	13
2.2	Electric Field Data	14
2.2.1	Antarctica	15
2.2.2	Kennedy Space Center	15
2.3	Local Model	17
2.3.1	Potentials in the atmosphere	18
2.3.2	Representative solution	20
2.3.3	Example of space charge and conductivity perturbations	22
2.4	Local Observations	24
2.4.1	Clustering Data	25
2.4.2	Spatial variations from wind direction	27
2.4.3	Temporal variations in the electric fields	30

2.4.4	Clouds in the GEC	34
2.4.5	Sunrise enhancement	38
2.5	Summary	41
3	Electrical Processes	42
3.1	Conductivity	44
3.1.1	Ion Production	45
3.1.2	Ion Losses	54
3.1.3	Ion Concentration	61
3.1.4	Cloud Current Convergence/Divergence	62
3.2	Current Sources	67
3.2.1	Storm Horizontal Extent	68
3.2.2	GEC Current Contribution	71
3.2.3	Global Distribution	74
3.3	Summary	85
4	Global Electric Circuit Model (WACCM-GEC)	86
4.1	Model Description	87
4.2	Calculation of Potentials	88
4.3	Non-uniform Boundary Conditions	92
4.4	Summary	96
5	WACCM-GEC Model Results	97
5.1	Influence of Magnetospheric Currents on GEC Properties	97
5.2	Antarctica Observations and Magnetospheric Influences	100
5.3	WACCM-GEC Evaluation	104
5.4	Solar Cycle Influences on the GEC	107
5.5	Volcanic Eruptions Influences on the GEC	112

5.6	Seasonal Variations	123
5.7	Summary	130
6	Conclusions	131
6.1	Major Findings	132
6.2	Future Advancements	135
	Bibliography	137

Tables**Table**

2.1	Summary of publicly available electric field data.	14
3.1	GCR ion production rate parameterization values during solar minimum [Tinsley and Zhou, 2006].	47
3.2	GCR ion production rate equations for any altitude [Tinsley and Zhou, 2006].	47

Figures

Figure

1.1 Carnegie curve	5
1.2 Global electric circuit processes	8
2.1 Field mill components	14
2.2 Kennedy Space Center Instrumentation	16
2.3 Model produced space charge and conductivity variations in the atmosphere	23
2.4 Diurnal variations of the Kennedy Space Center Field Mills	26
2.5 Wind direction variations in local electric fields	28
2.6 Wavelet analysis of Kennedy Space Center electric fields	31
2.7 Seasonal variation of electric fields at Kennedy Space Center	32
2.8 Long-term trend in electric fields at Kennedy Space Center	34
2.9 Overhead clouds impact on local electric fields	36
2.10 Model simulation of electric fields within clouds	37
2.11 Sunrise peak in the electric field	39
2.12 Sunrise peak in relation to relative humidity and wind speed	40
3.1 GCR altitude profile	48
3.2 GCR ionization vs latitude	49
3.3 GCR ionization vs latitude	50
3.4 Radon distribution	51

3.5	Radon concentration near the surface	53
3.6	Ion-aerosol attachment rates	57
3.7	Ion-cloud attachment rates	60
3.8	Vertical profile of conductivity	62
3.9	Current convergence/divergence around clouds	63
3.10	Cirrus cloud currents	64
3.11	Stratus cloud currents	65
3.12	Current distribution from a single storm	69
3.13	Currents exiting the domain from a single storm	70
3.14	Potentials from a dipole source current	73
3.15	Estimated currents from the TRMM satellite	75
3.16	Annual convective precipitation rate	76
3.17	Resistance ratio (storm efficiency)	78
3.18	Storm base height	79
3.19	Mean storm heights in the atmosphere	80
3.20	Frequency of storms	81
3.21	Annual GEC current contribution	82
3.22	Latitudnal distribution of current factors	83
3.23	Diurnal variation of current within the model	84
4.1	Schematic of electrical processes	87
4.2	Schematic of current contribution	90
4.3	Schematic of conductivity and resistance	91
4.4	Schematic of GEC system	92
4.5	Magnetospheric potential	94
4.6	Schematic of magnetospheric currents	95
5.1	Percent change due to the magnetospheric potential	100

5.2	Model results from Vostok and Concordia	101
5.3	Maximum diurnal variation of magnetospheric potential	103
5.4	Magnetospheric potential at in-phase and out-of-phase locations	104
5.5	Model comparison to Vostok and Concordia data	106
5.6	Conductivity for different solar conditions	108
5.7	Total resistance for different solar conditions	109
5.8	Current variation for different solar conditions	110
5.9	Percent change in GEC parameters from solar min to solar max	111
5.10	Variations in attachment rate due to Pinatubo	113
5.11	Latitudinal variations in attachment rate due to Pinatubo	114
5.12	Difference in total resistance from Pinatubo	116
5.13	Difference in the GEC current from Pinatubo	117
5.14	Changes in resistance from different volcanic aerosol amounts	119
5.15	Changes in GEC current from different volcanic aerosol amounts	120
5.16	Changes in GEC potential from different volcanic aerosol amounts	122
5.17	Column resistance seasonal variations	124
5.18	Current density seasonal variations	125
5.19	Electric field seasonal variations	126
5.20	Column resistance seasonal variations in 1997	127
5.21	Current density seasonal variations in 1997	128
5.22	Electric field seasonal variations in 1997	129

Executive Summary

This thesis focuses on the interpretation and understanding of electric fields within the atmosphere. Most people think of lightning and strong thunderstorms when talking about electric fields in the atmosphere, however, there are electric fields present at all times and everywhere in the atmosphere. Electric fields that are far away from thunderstorms are so-called fair-weather electric fields. Electrified clouds and thunderstorms act as generators within the atmosphere. The global integration of the generators creates a potential difference between the ionosphere and Earth. The potential difference between the ionosphere and ground drives the currents and electric fields in the fair-weather return path of the global electric circuit (GEC).

The first truly global model of the GEC was developed in the late 1970s by Hays and Roble [1979]. This model was based on spherical harmonics and required several assumptions to satisfy the equations, yet, it has been the gold-standard for over 30 years. With advances in modern computing power and the development of global climate models, the time is right for the development of a new GEC model.

This thesis describes the development of a new GEC model, which is available an open-source for the community. The model is incorporated into a preexisting community climate model that drives the atmospheric dynamics, which will be continually updated with new physics-based models of the atmosphere. This allows the GEC model to better represent the electric fields in the atmosphere without needing to develop new code. After development of the new GEC model, it is then utilized in the investigation of several open questions.

Publicly available electric field data sets were obtained from several locations to validate the model results. Kennedy Space Center (KSC) has an array of electric field mills that show a distinct spatial pattern in electric fields near the surface. The field mills closest to the ocean were measuring a 50 V/m enhancement in the electric field relative to the mills located inland when the wind was blowing from the ocean. This indicated that the air mass over the ocean is inherently unique from the air mass over land. A new statistical analysis method for understanding such long term data from an array of field mills is developed in this thesis. Using this analysis method provides a way to quantify the effects from the local sunrise and overhead clouds. With the knowledge gained from the impact of local meteorology on the measurements of electric fields, the global signature could be deduced from the local effects.

The global electric field signatures determined from the electric field mill measurements were used to validate the model output and investigate some of the new findings. Measurements from Vostok and Concordia, two sites in Antarctica, have shown that the overhead magnetospheric current system imposes different potentials at the two sites, which shows up in the electric field measurements [Burns et al., 2012]. Incorporating the magnetospheric potential into the GEC model showed that Vostok and Concordia do have different responses to the overhead magnetospheric potential and that it causes the diurnal variation of electric fields to be phase shifted relative to one another.

In previous models of the GEC, storms have been parameterized to produce a global current directly, unlike the new model, which utilizes the resistivity between the charge centers of the storm to identify how efficient a storm is at generating a global current. This was found to be a significant factor that has been overlooked and led to the realization that the strongest storms near the equator are less efficient at producing a global current compared to higher latitude storms. The new method of using the resistivity between the charge centers still produces most of the current near the equator, but storms closer to the poles contribute more current per storm in comparison to storms in the tropics. This shows that the model predicts mid-latitude storms to be weaker on average, but more efficient in generating a global current.

The new GEC model was run for multiple years over solar minimum and maximum conditions and during active volcanic periods to identify what affect these conductivity changes may have on the atmospheric electric fields. During these periods of solar extremes, there was a 20Ω change in total atmospheric resistance that occurs out of phase with the solar cycle. The total current in the circuit was much more variable during these times and showed little dependence on the solar cycle. The current and resistance changes together lead to a nearly 10% change in the near-surface electric fields throughout the solar cycle. When the new GEC model was run during the time of the volcanic eruption of Pinatubo in 1991 to determine the influence of a major volcano on the GEC, the volcanic eruption changed the timing of the seasonal variations in the electric fields but had little impact on the overall magnitude of the electric fields. It was found that increasing the aerosol load by a factor of 50 to simulate an extremely large eruption would double the total resistance of the atmosphere. However, this is neglecting any microphysical feedbacks from the aerosols that were shown to have a major impact on the interpretation of GEC results.

The development of the WACCM-GEC has opened up new avenues of research for the global electric circuit community. The use of the model provides new scientific insights into several problems discussed above. It is the hope of the author that these new insights and findings will lead to more investigations into these phenomena by future researchers, aided by continued use of the new GEC model.

Chapter 1

Introduction

This thesis will describe the development of several numerical models, supported by observations, to determine the electric fields and currents within the atmosphere. There are multiple sources and losses of ions within the atmosphere that determine how conductive the atmosphere is at a given location. Modeling all of the production and loss terms has relied upon parameterizations and climatologies in many previous studies, while this thesis focuses on the use of atmospheric physics and chemistry models to generate, advect, and consume ions within a realistic atmosphere. Weather and climate models currently incorporate physical, dynamical, and chemical processes, but do not consider the electrical processes within the atmosphere.

During this research project, novel numerical models that compute atmospheric electric fields in a physics-based framework have been developed. These models are integrated into numerical weather and climate models to generate a realistic representation of the electric field in the atmosphere. In order to test and verify these model simulations, an emphasis in this thesis will be to study electric field measurements by employing surface electric field mills at different locations around the globe. These field mill measurements are sensitive to both the global and local environment and require an understanding of the instrument and the environment within which it is operating.

1.1 Background

The global electric circuit (GEC) represents the electrical pathway by which charge is exchanged between the conductive surface of the Earth and the highly conductive ionosphere, which are held at different potentials by the currents produced from electrified clouds. Inherently atmospheric, this circuit is dependent on many of the physical and chemical processes that can affect charge and its transport in the atmosphere, both spatially and temporally. Indications of this global circuit were first measured by the Carnegie expedition documenting temporal variations of surface fair-weather vertical electric fields [Harrison, 2013]. These measurements were correlated with diurnal variations of global thunder days in universal time, suggesting that a global circuit exists with thunderstorms and electrified clouds acting as generators. These generators drive currents capable of influencing the electric field behavior around the globe [Whipple, 1938]. Figure 1.1 shows the thunder day measurements in comparison to the measured electric field on the Carnegie ship.

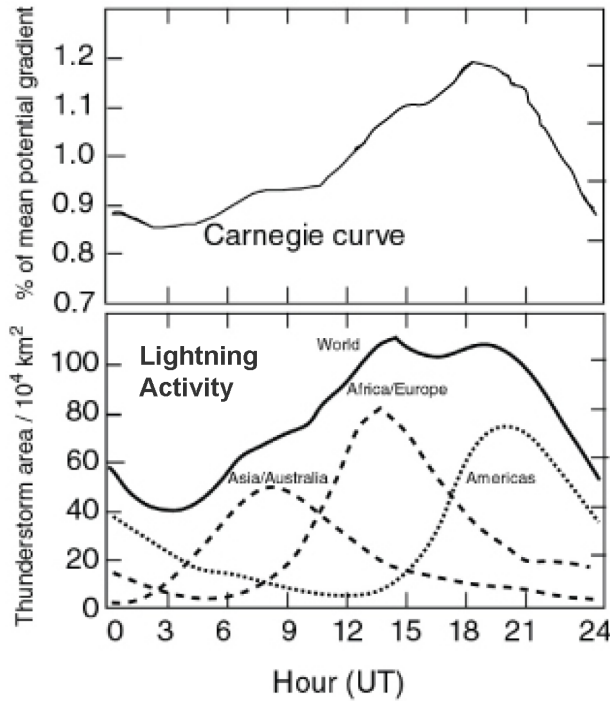


Figure 1.1: The top figure shows the ratio of the potential gradient to the daily mean, and the bottom figure shows the diurnal variation of thunderstorm area. Figure adapted from Whipple [1938].

The source currents produced by electrified clouds produce a potential difference (PD) between the ground and ionosphere of around 250 kV. The potential difference leads to an average fair weather return current density of a few pA/m². Many reviews have been written on the GEC discussing the generation and approximate values of these parameters, such as Rycroft et al. [2008]; Liu et al. [2010a]; Williams and Mareev [2014].

The first global numerical model to address the complexities of the GEC was developed by Hays and Roble [1979]. They made several assumptions on the conductivity and source distributions to represent the solution for the electric potential with analytic spherical harmonic functions in several distinct domains, but nonetheless were able to determine how currents were distributed throughout the atmosphere. In a separate paper, Roble and Hays [1979a] included large-scale horizontal potentials maintained by the ionospheric dynamo and magnetospheric convection and broadly discussed their influence on the GEC.

Since this first model, several other efforts have been undertaken, generally focusing on advancing conductivity formulations or source formulations independently. Several of these models have advanced conductivity perturbations to the system [Tinsley and Zhou, 2006; Odzimek et al., 2010]. The resulting conductivity distributions can then be used to solve for the electrical properties of the circuit by solving for vertical resistances and equivalent circuit elements. The conductivity distributions are parameterized with many assumptions such as the background aerosol content. These assumptions on the parameterizations and lack of integration with dynamical forcing provides an excellent opportunity for improvement.

Within GEC models the conductivity modeling has received the most attention, with source currents generally being parameterized with some relationship to lightning and storm frequencies [Hays and Roble, 1979; Kalb et al., 2016]. This parameterization of storm frequency and total lightning count to produce a current assumes that the contribution current is independent of conductivity within the domain.

1.2 Theory

There have been many papers describing correlations between solar and atmospheric dynamics and atmospheric electric fields with several outstanding questions addressed in recent review articles [Williams and Mareev, 2014; Markson, 2007]. Specifically, there are correlations to solar phenomena imposing variations on atmospheric microphysics [Tinsley, 1996, 2010]. These correlations generally have a fundamental physical description underlying them that is often theorized or proposed and often involves many linked processes that must be investigated as a coupled system rather than individually. Quantifying the affects of the underlying physical mechanisms is often extremely difficult because of the integrated nature of atmospheric electric fields. The electric fields can be generated by both global and local phenomena and decoupling these features is often difficult in practice.

The models discussed in section 1.1 were models that calculated the electrical parameters of the circuit from a parameterized atmosphere [Hays and Roble, 1979; Tinsley and Zhou, 2006]. There was no coupling of the dynamics to the electrical processes, rather there were background prescriptions of the underlying variables. Within the last 20 years there have been significant advancements in computing power and global model development. There are now free community developed models to drive the dynamics and microphysics of the atmosphere.

Utilizing these new community models provides a method to consistently treat the underlying physics behind the global electric circuit. The correlations that are theorized in the literature can be investigated with the use of these models due to their inherent coupling of many different processes in the atmosphere.

Figure 1.2 is an illustration of the physical mechanisms that drive the electrical processes within the atmosphere including the production and loss of ions, the generation of source current, and also the incorporation of other current systems at the boundaries. All of these processes are coupled together in the model to allow for a full incorporation of physical mechanisms behind the GEC.

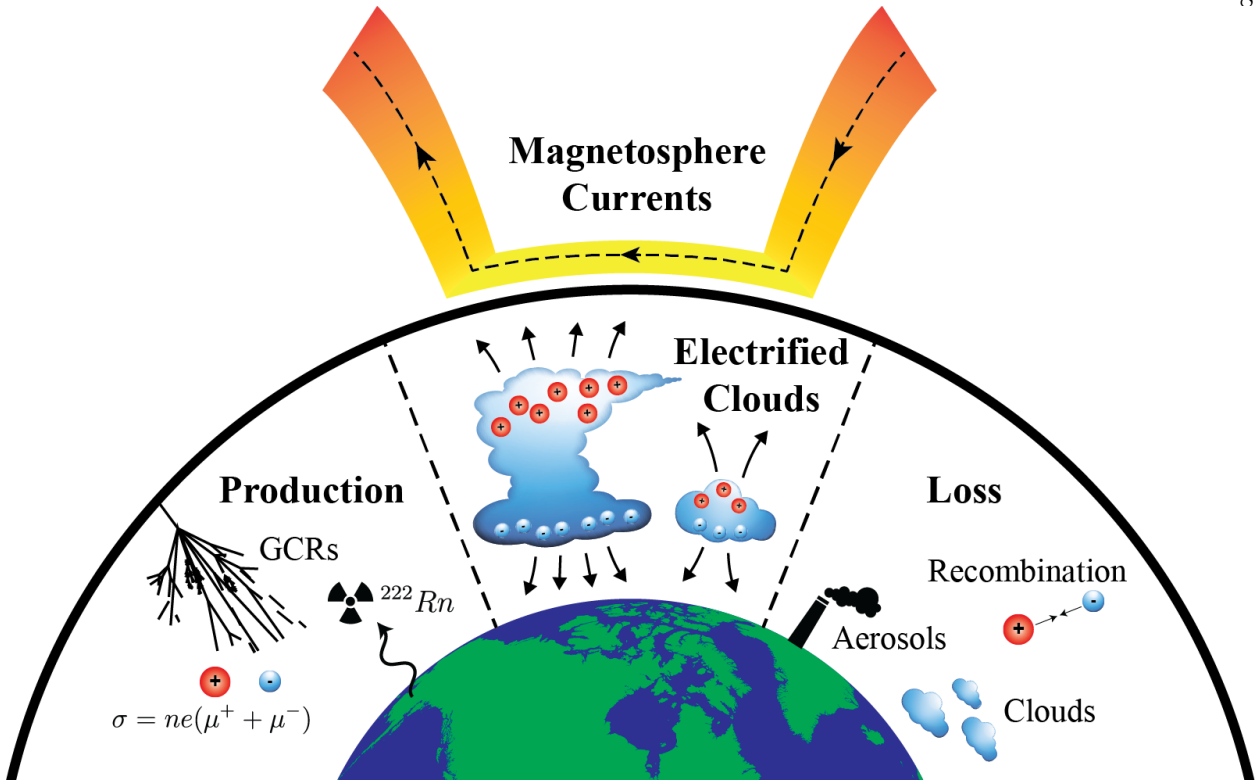


Figure 1.2: A representation of the major physical mechanisms that drive the electrical processes within the atmosphere including conductivity, sources and magnetospheric currents.

Developing more realistic representations of the current sources and conductivity within a physics-based framework provides a better understanding of how electric fields are created and evolve in the atmosphere. Several fundamental questions are addressed within this thesis that help develop an understanding of the coupling between physical processes and electrical processes in the atmosphere.

1.3 Research Questions

Initial investigation into the previous numerical models discussed in section 1.1 showed several areas of research that could be improved upon through the development of new numerical models and techniques for analysis of observational data. The overarching hypothesis addressed within this thesis is that: **Utilizing physical and dynamical processes within general circulation**

models will lead to better representations of electric fields and currents within the atmosphere. To address the hypothesis, the following specific science questions are addressed.

(1) What impact do local meteorological processes have on the measurement of the fair-weather atmospheric electric field?

Observational measurements of the electric field have been utilized for lightning detection and measurement, and the long-term averaging of these data sets to view the global electric circuit. The long measurement duration to view the GEC is needed to average out the short-term variations produced by various local meteorological influences. Data from Antarctica and from an array of over 30 field mills from Kennedy Space Center were obtained to investigate the local meteorological influences on the measured electric fields. This was accomplished in chapter 2 by creating new methodologies for looking at arrays of electric field mills in conjunction with local meteorological measurements.

(2) How does the global conductivity and source distribution influence the local atmospheric electric field measurements?

Measurements of the atmospheric electric field have shown that there is a distinct universal time signature that is observed globally. Several global models have been developed to investigate these relationships, but have had to make major assumptions on the conductivity or source distribution to obtain a solution [Hays and Roble, 1979; Tinsley and Zhou, 2006; Odzimek et al., 2010]. A new physics-based model, called WACCM-GEC, is incorporated into the Whole Atmosphere Community Climate Model (WACCM) in chapter 4. This new model calculates the global conductivity and source distribution to determine a realistic representation of the atmospheric electric field.

(3) How does the magnetospheric current system influence atmospheric electric fields in the global electric circuit?

Previous studies have shown that measurements in the Antarctic region are influenced by the potentials imposed at high latitudes by the solar-wind dynamo [Burns, 2005; Reddell et al., 2004; Corney et al., 2003]. The work within this thesis focuses on understanding these observations and related empirical relationships by exercising the WACCM-GEC model and imposing the potentials from the solar-wind dynamo generated in a global climate model onto the specific observational locations in Antarctica (Vostok and Conrodia stations). The agreement between the measurements in Antarctica and WACCM-GEC are discussed in section 5.2.

(4) What impact do strong conductivity perturbations have on the global electric circuit?

Atmospheric electric fields have been analyzed for over a century and long-term trends have been identified within these data sets. These have been theorized to be due to solar cycle variations modifying the galactic cosmic ray ionization rate and volcanic eruptions modifying the atmospheric aerosol concentration. The model developed within this thesis was run during solar minimum and maximum conditions to find that there is little solar cycle dependence on electric fields in the atmosphere as discussed in section 5.4. The influence of volcanic eruptions on the GEC was investigated by running the model over the Pinatubo eruption in 1991. Section 5.5 showed that even this significant eruption had little influence on the magnitude of the electric fields produced within the model. Use of a climate model showed that aerosols have a significant impact on the microphysics and dynamics underlying the global electric circuit, which causes greater influences on electric fields within the atmosphere than simply looking at loss of ions from attachment to aerosols.

The thesis begins with an analysis of measurements of atmospheric electric fields that are made across the globe in chapter 2. This chapter will be utilized to validate model development

and results in future chapters. The physical description of ion production and loss processes that go into any model of the GEC are described in chapter 3. Chapter 4 describes the electric circuit development within the models, including current and electric field generation. Lastly, the models are exercised in chapter 5 to determine how different atmospheric and solar perturbations modify the GEC.

Chapter 2

Meteorological Influences on Observational Data

The first ideas for a global current system and the global electric circuit (GEC) phenomenon were developed after global measurements of electric fields were all found to be correlated with each other. Electric field measurements have been critical to the understanding of the GEC and are used to validate and test model predictions. Measurements of the electric field in the atmosphere have occurred for over 100 years. These measurements are typically focused on either lightning applications where timescales are under 1 s and the changes in electric field, $\frac{dE}{dt}$, without an absolute magnitude are acceptable. On the opposite end of the spectrum are timescales over 1 h where slowly varying global signatures can be observed. Between these two domains there is a mix of local and global processes that influence the measured electric field.

This chapter will investigate the influence of local and global processes on the measured electric field with the utilization of several publicly available data sets. An in-depth statistical analysis was conducted in Lucas et al. [2017] to determine the local meteorological influences on measured electric fields that will be expanded upon within this chapter. Measured surface electric fields in the absence of local influences should represent variations of the global electric circuit. First, a brief description of the instrumentation used to measure the local electric field is discussed in section 2.1. Many of these instruments are deployed to warn of severe weather or collect fair-weather data but do not save the data or make it publicly available. A description of the available data will be discussed in section 2.2. A local model is developed in section 2.3 to describe the

differences between local and global scale phenomena. Finally, with the use of the local model, the influence of local processes on the electric field are investigated and quantified in section 2.4.

2.1 Instrumentation

The typical method that is used to measure the atmospheric electric field is with an electric field mill. Electric field mills are powered devices that spin a rotor that alternately expose and shield sense plates. Figure 2.1 shows a picture of the components of an electric field mill. The rotor (1) is grounded and provides a zero reference field when it is over the sense plates (2). A motor (5) drives the rotation of the rotor that causes different areas of the external electric field to be exposed to the sense plates. The change in area over time is therefore proportional to the rotation rate of the rotor, $\frac{dA}{dt} \propto \omega$. This effectively turns a DC signal from the external electric field into an AC signal. The sense plates (2) accumulate an amount of charge that is proportional to the external electric field and the area, $Q \propto EA$. This small amount of charge is then sent into a charge amplifier circuit (6) to amplify the signal. This produces an AC signal of unknown phase. To determine the phase of the signal there is generally a rotary encoder (4) that is attached to the motor shaft to signify what position the rotor is in. Coupling the rotary encoder and amplifier output together (7) produces an AC signal of known positive or negative strength. Finally, this signal is fed through additional low-pass filters and electronics (8) to produce a final DC output (9) that can be read by an analog to digital converter and recorded. More detailed descriptions of the electronics can be found in MacGorman and Rust [1998]. Many of the field mills that people use are designed to warn and detect when lightning is present, and may not be built with the best electronics or machining because it is unnecessary. Measuring the fair-weather field takes a little more care and attention to detail in order to measure the small changes in the field. Therefore, there are not as many atmospheric electric field measurements that are available for research use. The publicly available data sets for research purposes are discussed further in section 2.2.

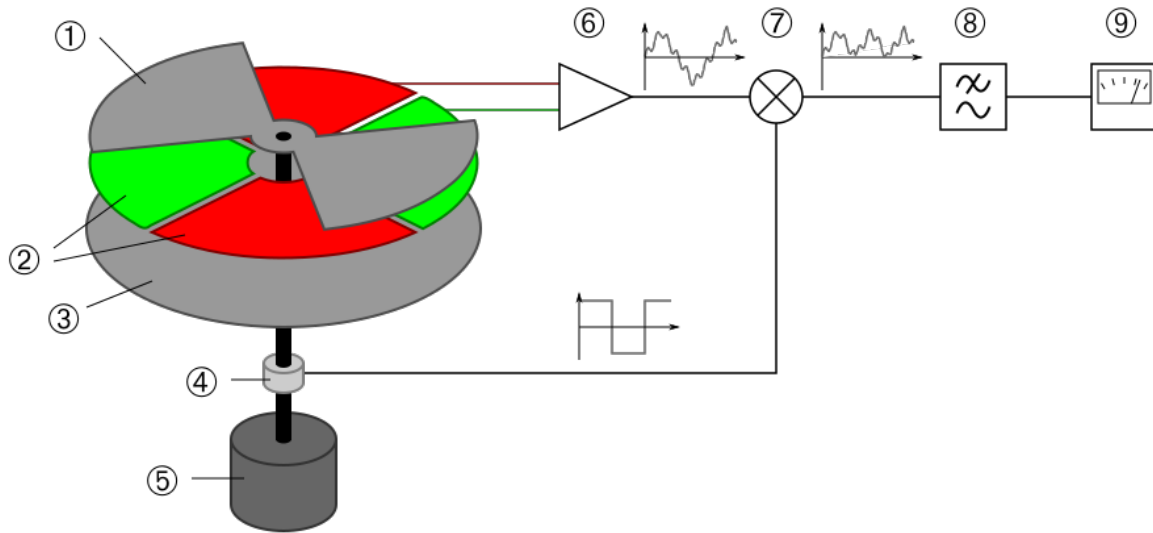


Figure 2.1: Typical field mill components and their integration. The components are: (1) Rotor, (2) sense plates, (3) ground plate, (4) rotary encoder, (5) motor, (6) charge amplifier, (7) multiplier, (8) filters, (9) output.

2.2 Electric Field Data

The publicly available data sets used within this thesis are obtained from Vostok and Concordia in the Antarctic discussed in section 2.2.1, and over 30 electric field mills located around Kennedy Space Center (KSC) discussed in section 2.2.2. Table 2.1 shows a summary of the data sources and availability.

Table 2.1: Summary of publicly available electric field data.

Site	Frequency [Hz]	Years Available	Link
Vostok	0.1	1998-2004	doi:10.4225/15/588811d206493
Vostok	0.1	2006-2011	doi:10.4225/15/58880fc1a1fb9
Concordia	0.1	2009-2011	doi:10.4225/15/5875ad6740e93
KSC	50	1998-present	kscwxarchive.ksc.nasa.gov

2.2.1 Antarctica

The Australian Antarctic Division has run several field campaigns in Antarctica investigating the atmospheric electric environment where they have archived the data. The available data online are from Vostok for the years 1998-2004 [doi:10.4225/15/588811d206493](https://doi.org/10.4225/15/588811d206493) and additionally for the years 2006-2011 [doi:10.4225/15/58880fc1a1fbdb](https://doi.org/10.4225/15/58880fc1a1fbdb). Data from Concordia station are available for the years 2009-2011 [doi:10.4225/15/5875ad6740e93](https://doi.org/10.4225/15/5875ad6740e93). The electric field was sampled every 10 seconds, with calibration files included with the data sets to obtain an absolute field.

2.2.2 Kennedy Space Center

Kennedy Space Center (KSC) utilizes an array of electric field mills for rocket launch safety that is a part of their suite of measurements used to decide if a lightning threat exists. The electric field mills at KSC are located in a unique environment where some are placed close to a coastline, while others are located further inland. This unique spatial distribution of the field mills combined with the 18-year data set allows one to investigate both the spatial and temporal variability of the near-surface atmospheric electric fields. Figure 2.2 shows a satellite image of Kennedy Space Center (KSC) with the field mills and meteorological instrumentation highlighted. The field mills are located between the Indian river on the west and the Atlantic ocean on the east with the Banana river passing through the middle of the site. The average minimum distance between two field mills is about 2 km, and the full spatial distribution of the array of field mills in longitude and latitude can be seen in figure 2.2, which is approximately 40 km on a side.

Kennedy Space Center has archived 50 Hz data of near-surface vertical electric field measurements from late 1997-present. The field mills were custom-made for KSC and are periodically calibrated with a known reference voltage input to the system. The data is flagged when values are being calibrated or erroneous for any reason, such as nearby mowing going on. All of the flagged data are discarded. For all subsequent analyses, the 50 Hz data has been converted to 1-minute means for each field mill. Meteorological data have been obtained from instrumentation on the

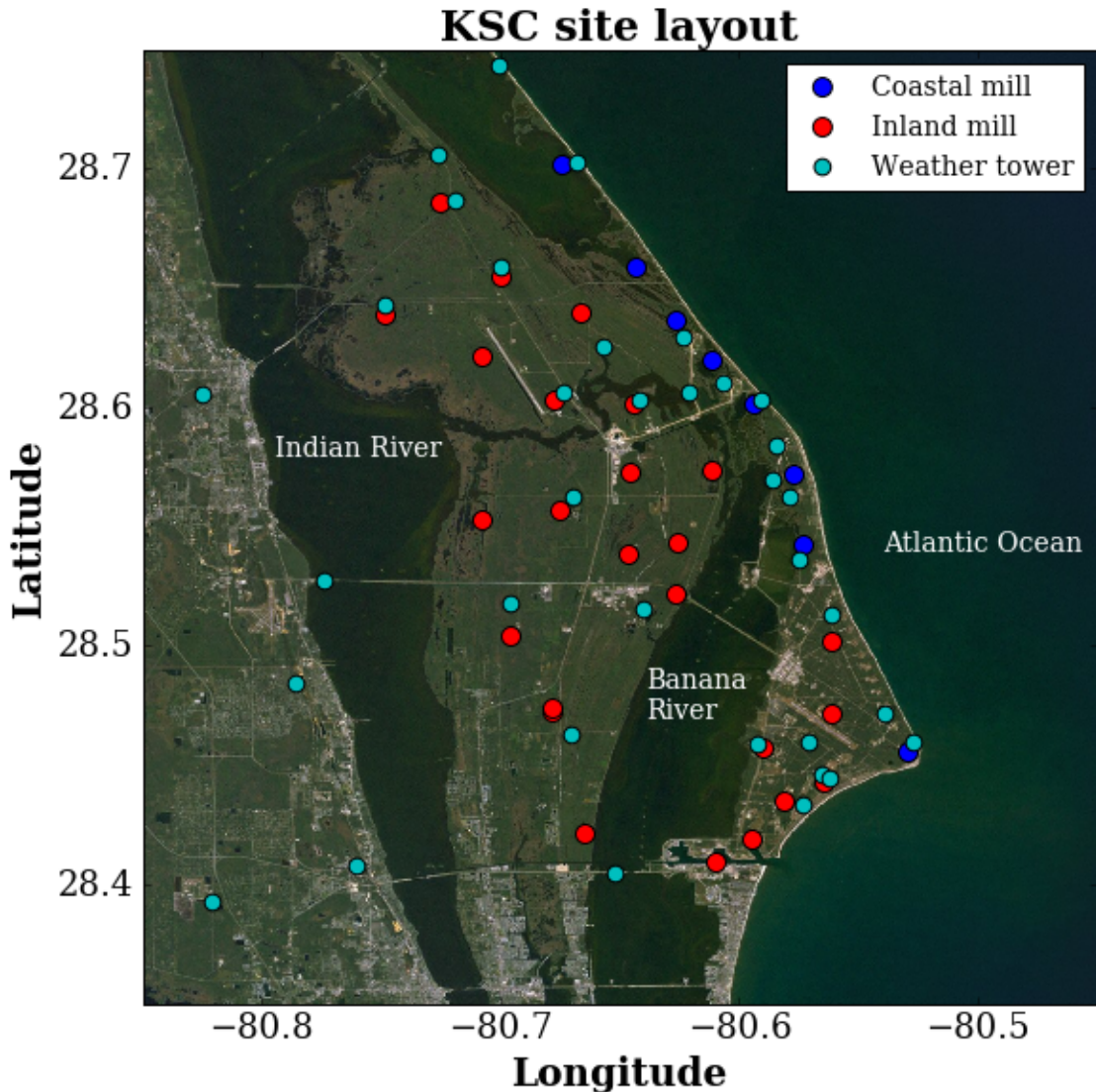


Figure 2.2: Instrumentation located around KSC in Florida. Electric field mills are the larger circles. Blue circles represent locations of coastal field mills, and the red circles represent locations of inland field mills. The smaller cyan circles are the locations of the meteorological towers.

local weather towers at a 5-minute frequency over the same time span. The meteorological data contains wind speed, wind direction, temperature, dew point, humidity, and pressure. Cloud cover and other reported meteorological conditions are obtained from automated Meteorological Terminal Aviation Routine (METAR) reports from the space shuttle landing strip (KTTS).

The electric field data are available at a 50 Hz frequency for the years 1998-present from kscwxarchive.ksc.nasa.gov. The data is in a binary format that requires some decoding to deal

with. Therefore, a binary decoder was written to download and save the field mill data in a more accessible format. The code is located on github: <https://github.com/greglucas/KSC>. This tool parses the binary format and outputs csv files that contain the electric field readings from each field mill as 1-minute means. The data obtained from the array of field mills will be utilized in the following sections to elucidate local meteorological influences on the electric field.

2.3 Local Model

Recent modeling efforts for the GEC have been undertaken within community climate models to determine how the near-surface electric field varies with time at different locations across the globe [Baumgaertner et al., 2013; Mareev and Volodin, 2014; Lucas et al., 2015]. These models provide a means of analyzing long-term and large spatial distributions of atmospheric electric fields due to the global distribution of conductivity and currents in the GEC. However, the models are not able to resolve local influences on near-surface electric fields. This becomes an issue when interpreting the global model output in comparison to near-surface electric field data that contains local meteorological influences not captured within climate models. This requires the local and global electric field signatures within the observational data sets to be separated from one another. Statistical analysis of the observational data sets can identify these differences, but a numerical model can provide quantitative constraints on local and global factors influencing the electric field.

The local near-surface electric field measurements can be modified from a nominal atmosphere in several distinct ways. One possibility is to modify the local electrical environment by changing either the conductivity or space charge distribution. Another way is through the vertical column resistance of the atmosphere. Conductivity changes can occur through changes in the concentration of charge carriers and/or their mobility. This scenario generally occurs due to an increased/decreased ionization rate, or a change in the loss of ions due to attachment of ions to heavier and less mobile aerosols, dust, or other large particles [Hoppel, 1985]. A space charge occurs when one polarity of charge is preferentially present in the local environment over the opposite polarity of charge which produces a divergence in the electric field, $\nabla \cdot E = \rho/\epsilon_0$, where ρ is

the space charge density. This divergence can occur through the preferential separation of positive and negative ions onto small and large droplets or aerosols. These different size particles are then gravitationally sorted and advected, causing deviations in the local charge concentrations [Hoppel, 1985; Hoppel and Gathman, 1971].

Previous articles have described the generation of electric fields from space charge in the atmosphere [Marshall et al., 1999] or from conductivity changes in the atmosphere [Nicoll, 2012; Yaniv et al., 2016; Nicoll and Harrison, 2016]. However, these approaches have not incorporated the coupling of space charge and conductivity effects together in the same model. The incorporation of the coupling of both phenomena in a single mathematical derivation provides insight into the interpretation of the observations. Although conductivity or space charge effects are not directly determinable from the observations, the mathematical model provides limits to the possible value for atmospheric conductivity changes and local space charge changes that match the observations. This will be demonstrated when describing the impact of wind direction and cloud coverage on the near-surface electric field observations in section 2.4.

2.3.1 Potentials in the atmosphere

Within the global electric circuit, the current continuity equation is solved to obtain the currents and electric fields throughout the atmosphere. This is based on Ohmic relationships where the conductivity and electric field lead to conduction currents flowing through the system. Here, ionization from radon and galactic cosmic rays form ionization pairs that are subject to various processes that affect mobility and concentration. The integrated ion mobility in the electric field gives rise to the conductivity. However, local production of ions by processes such as wave breaking do not form in pairs and, in general, are positively charged [Blanchard, 1966; Hoppel et al., 1986]. This can lead to an imbalance in ion concentration, i.e. space charge, if not counter balanced by charges of opposite sign. This describes the electrode effect ¹ in the planetary boundary layer whose

¹ the accumulation of an excess of ions of positive sign in the neighborhood of a negative electrode, and vice versa, when ions are continuously produced in the space above the electrode and move under the influence of the electrode's field [Chalmers, 1957]

charge distribution in altitude and by region is quite variable [Markson, 2007]. To incorporate all of the local effects, the current continuity equation has an additional local current source, J_{local} , that also needs to be accounted for in addition to the globally driven GEC currents, J_{GEC} . The continuity equation becomes

$$\nabla \cdot (J_{GEC} + J_{local}) = 0. \quad (2.1)$$

Expanding this equation out in terms of potentials, ϕ , and conductivity, σ gives

$$\nabla \cdot \sigma \nabla (\phi_{GEC} + \phi_{local}) = 0. \quad (2.2)$$

In fair-weather, the current flows primarily in the vertical direction and therefore, in this derivation, currents and electric fields are confined to the vertical coordinate, z , which is directed positive upwards away from the surface. Expanding equation (2.2) into two separate equations produces

$$\phi''_{GEC} + \frac{\sigma'}{\sigma} \phi'_{GEC} = k(z) \quad (2.3)$$

$$\phi''_{local} + \frac{\sigma'}{\sigma} \phi'_{local} = -k(z) \quad (2.4)$$

where ' indicates differentiation with respect to z and $k(z)$ is a function used to separate the two equations. With a substitution of $u = \phi'$, the differential equation takes the following form

$$u' + f(z)u = k(z), \quad (2.5)$$

which can be solved with an integration constant of $e^{\int f(z)dz}$. Recognizing that the integral of σ'/σ is $\ln \sigma$, the integration constant becomes σ . This yields the following solution for u

$$u = \frac{1}{\sigma} \int \sigma k(z) dz. \quad (2.6)$$

Integrating u then gives the solution for the potential in the region, with two integration constants.

The function $k(z)$ is unknown, but the local potential is generated by a space charge density, $\rho(z)$, and therefore, the potential due to space charge can be obtained by solving Gauss' law

$$-\phi''_{local} = \rho(z). \quad (2.7)$$

The potential due to this additional space charge must go to zero at the boundaries of the space charge region to satisfy the GEC potential being constant across the boundaries. These two boundary conditions allow one to solve for the constants of integration and obtain a solution for the potential due to the local space charge throughout the region. With the local potential and conductivity known, equation (2.3) can be used to solve for $k(z)$ and then finally solve for the potential due to the GEC throughout the domain with equation (2.6). This description of equations can be utilized with any number of layers throughout the domain and provides a general method to calculate the potential throughout the atmosphere. The following section will utilize the derived equations to produce a representative solution for a given region.

2.3.2 Representative solution

To obtain a representative solution throughout the atmosphere the equations derived in section 2.3.1 are applied to a simple atmospheric distribution of space charge and conductivity. For this simple distribution, the space charge density is assumed constant with height between the surfaces z_0 and z_1 . Solving for the local potential due to this space charge throughout the region gives

$$\phi_{local} = \frac{\rho}{2} (z_1 - z) (z - z_0), \quad (2.8)$$

with the potential going to zero at z_1 and z_0 . Assuming an exponential conductivity profile of the form

$$\sigma = \sigma_0 e^{z/l}, \quad (2.9)$$

where l is the scale height, the conductivity and potential due to space charge can be used to solve for $k(z)$,

$$\rho + \frac{\rho}{2l} (-2z + z_0 + z_1) = -k(z). \quad (2.10)$$

Using equation (2.6), the GEC potential in the domain can be solved for.

$$\phi'_{GEC} = e^{-z/l} \int -\rho e^{z/l} \left(-\frac{z}{l} + 1 + \frac{z_0 + z_1}{2l} \right) dz \quad (2.11)$$

$$= e^{-z/l} \left(-\rho e^{z/l} \left(2l - z + \frac{z_0 + z_1}{2} \right) \right) + C_1 e^{-z/l} \quad (2.12)$$

$$= -\rho \left(2l - z + \frac{z_0 + z_1}{2} \right) + C_1 e^{-z/l} \quad (2.13)$$

Integrating again to obtain the GEC potential

$$\phi_{GEC} = \rho z \left(\frac{z - z_0 - z_1}{2} - 2l \right) - C_1 l e^{-z/l} + C_2. \quad (2.14)$$

The total potential within the region is then

$$\phi = \phi_{GEC} + \phi_{local} = \rho \left(-2lz - \frac{z_0 z_1}{2} \right) - C_1 l e^{-z/l} + C_2. \quad (2.15)$$

To determine the integration constants in each region, the appropriate boundary conditions need to be given. Here, the potential is defined to be zero on the surface of the earth, and the potential to reach the GEC ionospheric potential, Φ_{GEC} , as z goes to infinity. Finally, at each interface, the current and potential need to be continuous. All of these boundary conditions are defined mathematically below with a single interface, z_1 , between regions I and II,

$$\phi_I = 0 \quad \text{when } z = 0 \quad (2.16)$$

$$\phi_{II} = \Phi_{GEC} \quad \text{when } z = \infty \quad (2.17)$$

$$\phi_I = \phi_{II} \quad (2.18)$$

$$\sigma_I \frac{d\phi_I}{dz} = \sigma_{II} \frac{d\phi_{II}}{dz} \quad \text{when } z = z_1. \quad (2.19)$$

There are two boundary conditions and two equations for each interface, which gives a linear set of equations to solve for all of the constants in the domain. This formulation enables the potential, and therefore the current and electric field, to be determined anywhere in the atmosphere given a conductivity profile, a space charge distribution, and the GEC potential of the ionosphere.

A full solution for the potential within the atmosphere due to any space charge and conductivity distribution has been derived, with a representative regional example given for an exponential conductivity distribution and constant space charge. This formulation of space charge and conductivity can be utilized within climate models, such as the GEC model described by Lucas et al. [2015], to obtain a more realistic representation of local electric fields. A parametrization of the space charge density within the boundary layer in addition to the conductivity formulations that have already been developed and incorporated into the models would need to be developed. In the following section these equations will be utilized with typical values for conductivity and space charge seen in the literature to help interpret the observations.

2.3.3 Example of space charge and conductivity perturbations

To illustrate the differences between space charge and conductivity changes, a two region model based on the equations of section 2.3.2 will be utilized. Region I is the closest region to the surface and is modified with either a constant space charge, ρ , or conductivity reduction, α , where $\sigma_I = \alpha\sigma$. Region II is clear atmosphere with an exponential conductivity profile given by equation (2.9) with $\sigma_0 = 5 \times 10^{-14} \text{ S/m}$ and $l = 6 \text{ km}$ [Dejnakarintra and Park, 1974]. Conductivity near the surface in Florida has been found to be 1/3 to 1/10 the typical values used here [Blakeslee and Krider, 1992; Kraakevik, 1961], but due to incomplete knowledge of the vertical profile, the standard conductivity profile within the literature will continue to be utilized. Figure 2.3 shows the electric fields and potentials in the domain when a space charge and conductivity perturbation are introduced. The green lines represent a completely clear atmosphere, the red lines contain a constant space charge introduced within region I, and the blue lines contain a conductivity reduction within region I. The GEC potential is held fixed at 300 kV. The electric field is discontinuous on the boundaries of region I, represented by the blue lines due to the “jump” in conductivity between the regions. This maintains current continuity through the interface and also inherently produces a space charge due to the gradient in conductivity, which is separate from an externally introduced space charge. When a source-generated space charge is introduced in region I (red lines) there is

no discontinuity in the electric field, but the slope of the electric field is modified producing a more negative electric field near the surface. Marshall et al. [1999] observed a similar slope in the vertical electric field when raising and lowering an electric field mill on a balloon near sunrise within the boundary layer, suggesting that space charge is present.

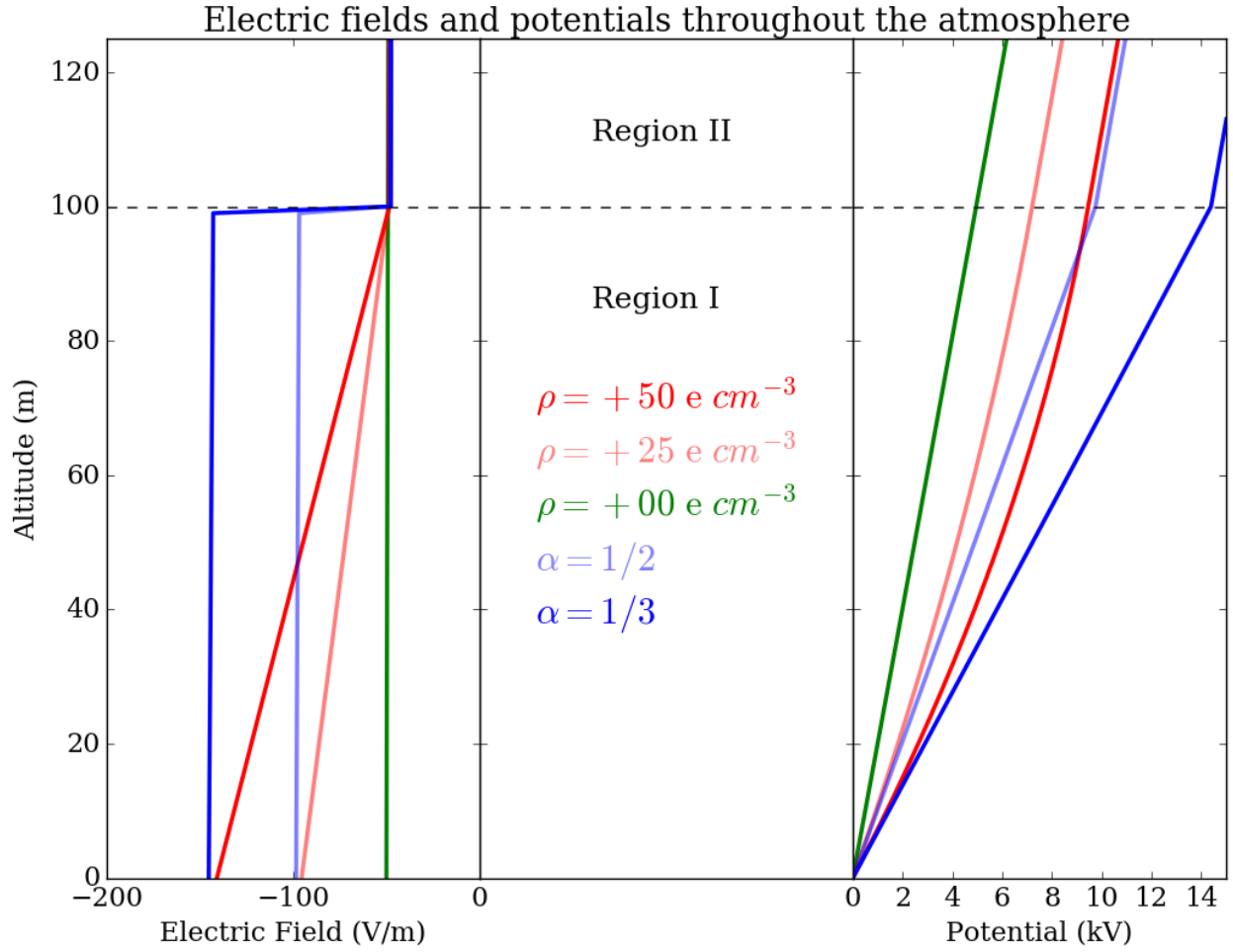


Figure 2.3: Modeled electric fields and potentials due to modifications of space charge and conductivity. The green line is the fair-weather atmosphere, the red lines are due to a modification of the local space charge, ρ , while the blue lines are due to a reduction in conductivity, $\sigma_I = \alpha\sigma$.

Separating the potential into local and global contributions enables the analysis of both conductivity and space charge perturbations to local electric field measurements. As expected, figure 2.3 demonstrates that the local electric field is modified by a change in conductivity and/or a change in space charge. A space charge of 50 e cm^{-3} produces a similar surface electric field

to a conductivity reduction of $\alpha = 1/3$ through the first 100 m of atmosphere. If a different conductivity profile is utilized, the amount of space charge to produce a similar effect would be different as well. A single surface electric field measurement is therefore unable to distinguish which of these factors is causing the field change. However, it does provide some constraint on how much of a change would need to occur to produce the amount of change observed in the near-surface electric field. Furthermore, certain meteorological conditions, such as cloud cover, may help distinguish between a perturbation due to conductivity or space charge, which is discussed within section 2.4.4. A colocated conductivity probe or multiple electric field measurements with altitude would also provide the information needed to distinguish between the two phenomena. This is seen by the discontinuity in electric field when conductivity is changed compared to a change in the slope of electric field seen when space charge is incorporated. This model will be exercised in section 2.4 to describe the local phenomena seen in the electric field data sets at KSC.

2.4 Local Observations

The data from KSC constitute the longest continuous record of sub-hour electric field mill data freely available, derived from an array of field mills to give a horizontal structure to the near-surface vertical electric field, E_z . These unique features of the data set will be exploited in the following sections. First, section 2.4.1 discusses the data in more detail and some of the processing steps undertaken for the subsequent statistical analyses. The statistical analysis is used to make autonomous groupings of field mills and to describe statistically the spatial and temporal influences on the near-surface electric field. Section 2.4.2 utilizes the array of field mills and the statistical analysis to describe the spatial variations seen in the data. The 18-year duration of field mill data is utilized in section 2.4.3 to discuss the variations seen within the data across multiple temporal scales. Finally, section 2.4.4 discusses the influence of clouds on the electric field and section 2.4.5 discusses the sunrise enhancement that is seen in the electric field data at KSC.

2.4.1 Clustering Data

Each field mill in the network has its own unique signature that is influenced by the local environment. To investigate the spatial distribution that leads to horizontal variability in the near-surface vertical electric field, a K-means clustering algorithm is implemented to self-generate groups of field mills. The K-means clustering generates groups autonomously by minimizing the distance between the observations, \mathbf{x} , and the group's mean, $\boldsymbol{\mu}_i$. The equation to be solved is shown below for k groups, which is set equal to two.

$$\arg \min_{\mathbf{S}} \sum_{i=1}^k \sum_{\mathbf{x} \in S_i} \|\mathbf{x} - \boldsymbol{\mu}_i\|^2 \quad (2.20)$$

The potential gradient (PG) is commonly used in the GEC community to work with positive values and is simply defined as the negative of the electric field, $PG = \nabla\phi = -E$. The median diurnal variation of the potential gradient every minute from each field mill is shown in figure 2.4. The two different groups determined solely from the K-means algorithm are colored red and blue. Figure 2.2 identifies the mills in each of these two groups using the same color scheme and shows that these groupings have a clear spatial dependence, with blue mills lying near the coast while red mills are inland. This was done without any manual selection of the groups, relying solely on the K-means clustering algorithm, which is strong statistical evidence that there are local differences in the field mills based on their spatial location. The blue coastal mills are all situated approximately 100 m from the ocean. This indicates that local bodies of water may have an impact on the local environments of individual field mills. The average diurnal variation in the near-surface electric field derived from the Carnegie cruises [Harrison, 2013] is plotted as dashed black lines, which are multiplied by the median values for the two statistical groups. The KSC field mill diurnal variations follow a similar trend to the Carnegie curve variation, with a notable exception around 12 UT that will be discussed further in section 2.4.5.

The electric field and meteorological observations obtained from KSC span 18 years and contain many different local events over the course of this time. A common way to determine

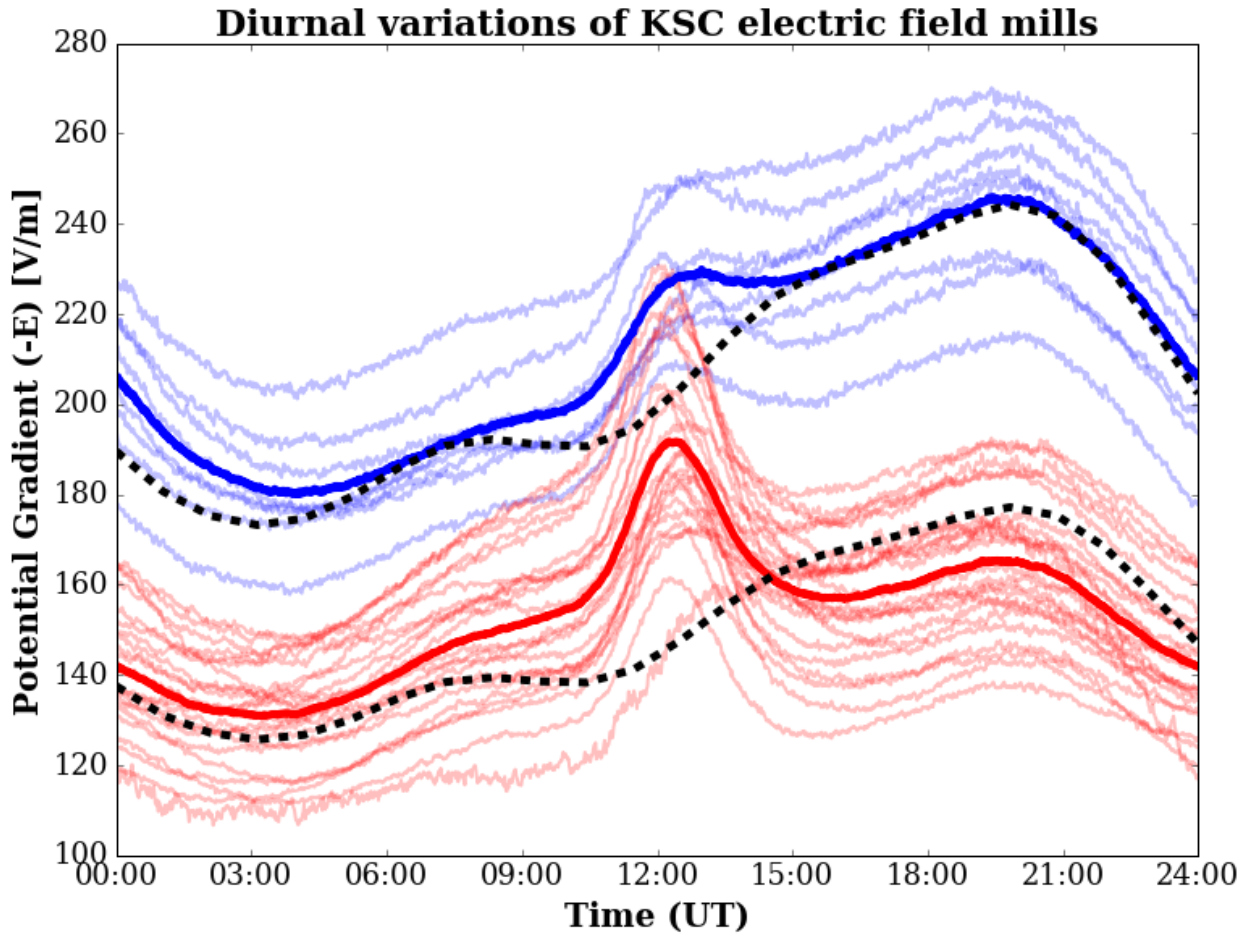


Figure 2.4: Median diurnal variations of the potential gradient every minute for all field mills at KSC, with blue indicating coastal mills and red indicating inland mills, which are grouped by a K-means clustering algorithm. The dark lines are the mean of all field mills within each group. The dashed, black lines are the annual Carnegie curve variations [Harrison, 2013] multiplied by the median for the coastal and inland field mill groups. KSC is in the Eastern time zone which corresponds to UTC-5 standard time.

fair-weather electric fields is to limit data to specific meteorological conditions or electric fields between a given threshold [Burns et al., 2012]. To avoid self-imposed biases of the data set to certain meteorological conditions and arbitrary thresholds of electric field, the following statistical analyses employ the median as the statistic of interest rather than the mean. This is a more robust statistic against outliers compared to the mean and allows the entire data set to be investigated without limiting it to certain time periods or thresholds of electric field values. This means that there will be thunderstorms and electrified shower clouds at the extreme ends of the data. However,

due to the large amount of data, the median is not significantly affected by these extreme values. The variance in the data is then described by the median absolute deviation (MAD). The MAD is the median of the absolute deviation of each observation, X_i , from the median of the entire sample, $\text{median}_j(X_j)$,

$$\text{MAD} = \text{median}_i(|X_i - \text{median}_j(X_j)|). \quad (2.21)$$

The median and median absolute deviation for both the coastal and inland field mills are shown below. These values are computed from over five million, one-minute means of electric field data.

	Median (V/m)	MAD ^a (V/m)
Coastal	205.8	46.8
Inland	149.3	36.0

^aMedian absolute deviation.

2.4.2 Spatial variations from wind direction

The location of KSC along the Florida coast produces complex meteorological and space charge patterns that occur as discussed in section 2.2.2. Each field mill in the regional array of electric field mills experiences the global changes of the vertical electrical field within the GEC. In addition to the global signature, the vertical electric field also has modifications superimposed on it by the local meteorological environment. This is evident in figure 2.4, where the solid blue and red curves follow the same general trend as the dashed, black Carnegie curves, which is due to the GEC, but they also show deviations from those curves, which are attributed to local effects. Section 2.4.1 statistically derived two distinct groups of field mills that were identified generally as coastal and inland. Within the rest of the manuscript, the median of the mills within each group will be used every time to produce a representative mill labeled coastal or inland. These two representative mills are sensitive to the mean local environment of all the mills within the respective groups, which gives an average behavior for each group. Figure 2.5 shows the influence that wind direction has on the field mills by analyzing the difference of coastal minus inland potential gradients. When there is

an on-shore wind (325 to 150 degrees), there is a strong deviation of more than 50 V/m between the coastal and inland field mills. When the wind is off-shore, there is a much smaller deviation between the field mills.

Potential gradient differences between coastal and inland sites

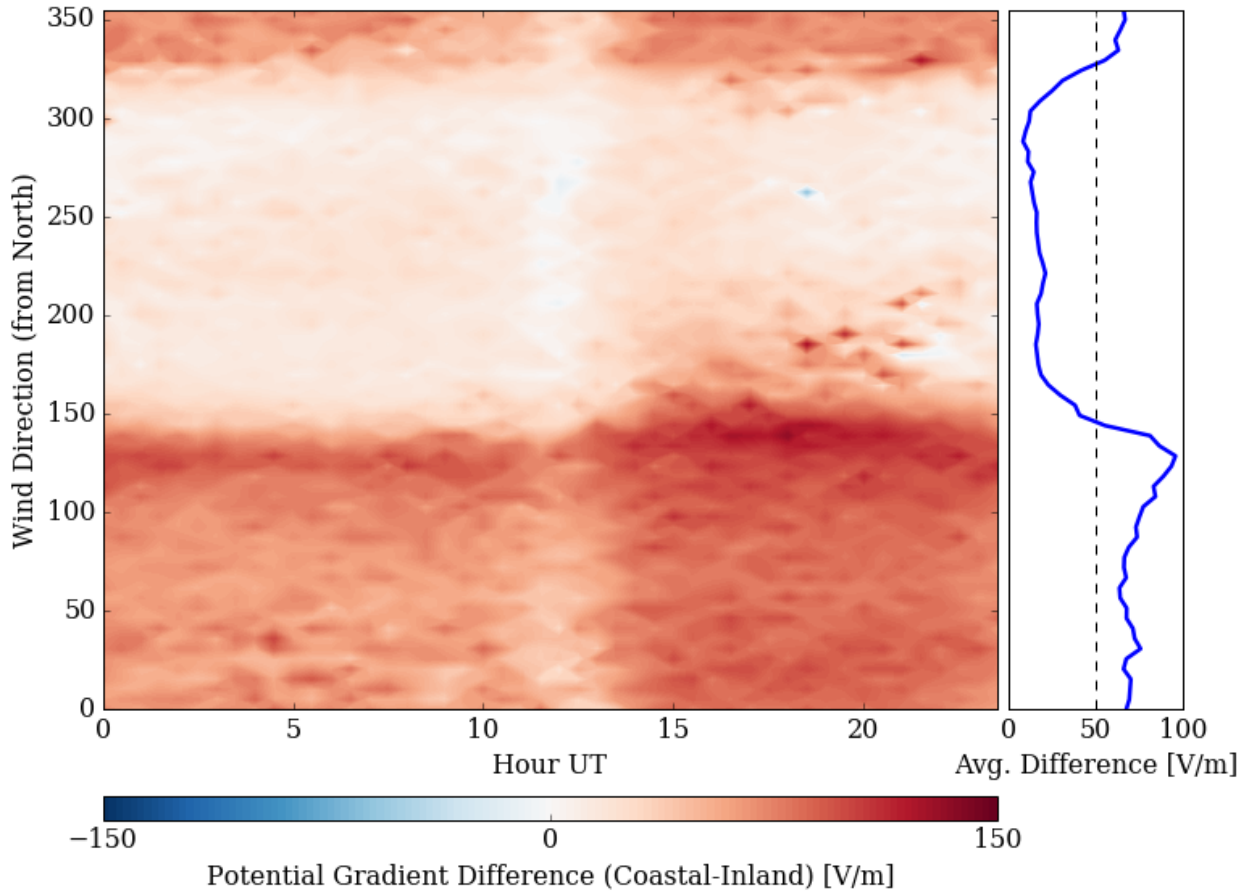


Figure 2.5: The deviation between coastal and inland field mills over time (UT) and wind direction. There is a deviation of more than 50 V/m when the wind is coming from the east or northeast, irrespective of the time of day.

This 50 V/m deviation between coastal and inland mills is suspected to be due to an addition of space charge from the electrode effect [Markson, 1975] over the ocean or surf near the coast [Blanchard, 1966; Gathman and Hoppel, 1970] being brought over the coastal field mills. The additional space charge enhances the electric field of the coastal mills, but is not advected further inland over the inland field mills. This local space charge can be viewed as adding an additional

local current source, J_{local} , in addition to the current flowing within the GEC, J_{GEC} , as discussed in section 2.3. The local current can be produced by convective mechanisms, eddy diffusion, and/or turbulence that moves this space charge mechanically to produce electric currents [Markson et al., 1981]. Utilizing the model development in section 2.3.3, figure 2.3 showed that measurements of the electric field at a single point are unable to determine whether this deviation is due to space charge or a change in conductivity by ion attachment to aerosols making them less mobile. Thus, another possible cause for the wind direction dependency on the coastal and inland near-surface electric fields is through local conductivity changes. Willett [1985] describes how radioactivity from the soil increases local conductivity, which means that the air masses over ocean and land have different conductivity. Consequently, the advection of the ocean air mass over the coastal mills could reduce the local conductivity and increase the electric field. However, previous measurements of the charge distribution near coasts have shown that ocean surf produces a significant space charge [Blanchard, 1966], suggesting that this could be the cause of the difference in measured near-surface vertical electric fields between the inland and coastal field mills.

The electric field mills at KSC determine the local vertical electric field, but more information is needed to determine whether conductivity or space charge is causing these deviations, as section 2.3 showed. One possible method, elucidated by the model simulations shown in figure 2.3, is to observe the change in vertical electric field with height. As shown in figure 2.3, a space charge distribution will produce a vertical gradient in the electric field when space charge is present, while conductivity changes will produce no vertical gradient. Marshall et al. [1999] obtained this type of information from raising and lowering a balloon and observed a vertical gradient in the electric field with height, suggesting space charge was present during those flights. A more extensive campaign of vertically distributed field mills in combination with the horizontal array, under the various conditions elucidated by our statistical study, would help resolve this ambiguity in whether space charge or conductivity is the cause of changing near-surface electric fields.

In summary, a strong spatial deviation of electric field measurements from field mills around KSC that is dependent on the wind direction was identified. This indicates that two different

local air masses, one inland and one near the ocean, have strong influences on the measurement of atmospheric electric fields. In future studies, a vertical distribution of field mills could help elucidate the influence of space charge and conductivity content on the local electric fields.

2.4.3 Temporal variations in the electric fields

The 18-year data set provides the ability to statistically determine signals that span the range from diurnal to multi-year. To identify when different periodic variations are present throughout the data set a wavelet analysis is performed following the derivations of Torrence and Compo [1998]. The bias correction discussed in Liu et al. [2007] is utilized to normalize the power over all periods within the data set. The entire data set is filtered for outliers by keeping data within five median absolute deviations of the median, using the median statistics discussed in section 2.4.1. This removes the outliers, presumably due to local thunderstorms and electrified clouds, from the data set, providing a way to determine the periodic variations due to fair-weather signals. The data set was resampled to a 30-minute frequency and normalized to a zero mean and one standard deviation for the wavelet analysis. Figure 2.6 shows the normalized wavelet analysis for the representative coastal and inland field mills. This analysis shows the relative power of the different periodic signals and how that power varies over the course of the data set.

There is a distinct one-day period seen throughout the data, which is attributable to the global electric circuit diurnal variation. The diurnal signal is not a solid color across the data set, which means that the signal has strong variations in power over intervals of time that exceed days, i.e. weeks and months. This is the reason that multi-day averages were needed to obtain a representative diurnal curve that is colloquially known as the Carnegie curve. There are several other longer time periods that show up at random times indicating no regular variation is present at these temporal scales. There also appears to be a fading of the diurnal signal, particularly for the representative inland mill, from 2008 onwards. This could be due to a decrease in the amplitude of the signal, or that there is less correlation each day during this time period. On shorter timescales the representative inland mill shows a small 12-hour periodicity. This periodicity is likely caused

Wavelet Analysis of Coastal Electric Fields

Wavelet Analysis of Inland Electric Fields

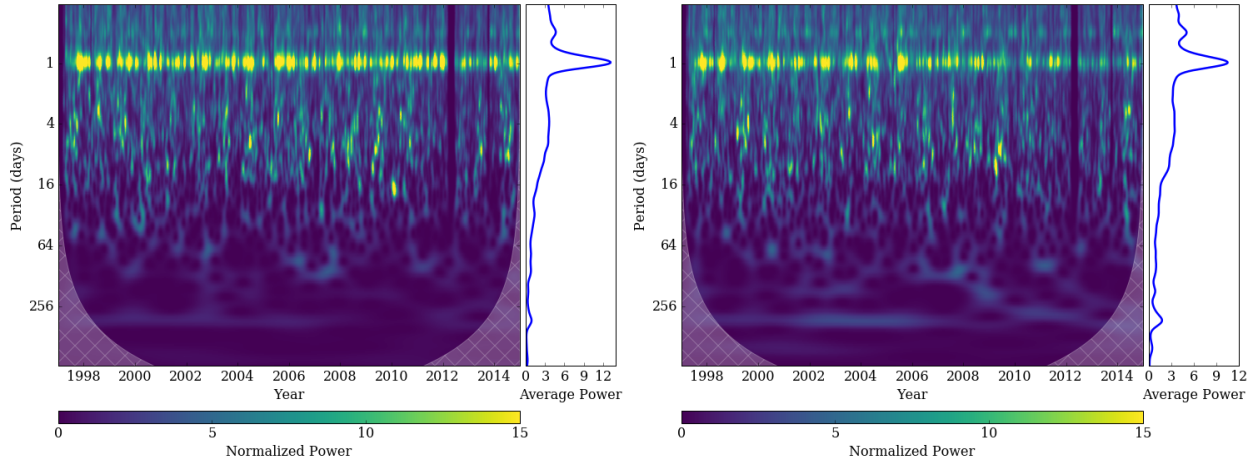


Figure 2.6: Wavelet analysis of coastal electric fields on the left and inland electric fields on the right, with the cone of influence in the white, cross-hatched region, indicating areas where the analysis is not valid. The data was normalized to have zero mean and a variance of one prior to the wavelet analysis. The analysis shows a strong diurnal signal in both data sets with a weak annual signal also present.

by the sunrise effect that is more prominent in the inland field mills than the coastal ones, which will be discussed in more detail in section 2.4.5.

An interesting observation is that there is only a small amount of power seen in the annual period. Figure 2.7 shows the median electric field for each month over the time of day for the coastal sites. The coastal site is chosen to reduce the contamination from the large amplitude sunrise effect that impacts the inland mills, although there could still be contamination from smaller amplitude land/sea breeze perturbations that occur at regular frequencies. This shows that there is about a 10 V/m change over the course of a year, in contrast to the greater than 50 V/m change attributable to the diurnal variation. It is not currently known whether there is a trend in the annual signal of the GEC [Williams and Mareev, 2014]. This data from KSC indicates that the signal is likely weak, and that the local meteorological effects provide more variation than is seen within the annual cycle. Therefore the annual cycle seen at KSC could be a manifestation of the local meteorology changing on an annual cycle, i.e. seasonal changes in the local atmosphere. For example, figure 2.7 indicates that the largest variability over the year is occurring around 18-22 UT in the summer

to fall months. This represents local afternoon for the field sites and the peak in the American chimney of the Carnegie curve. Thus, it is entirely likely that the filtered data set is still sensitive to local thunderstorm activity resulting in the apparent annual cycle signal in the wavelet analysis. This finding is in contrast to other articles demonstrating a distinct seasonal and annual variation in atmospheric electric fields [Burns et al., 2008; Blakeslee et al., 2014] due to seasonal variations in convection over the northern and southern hemisphere. Although the observations in polar regions are not influenced by local thunderstorm activity, annual variations in other meteorological properties may persist that manifest as an annual cycle in the electric field data.

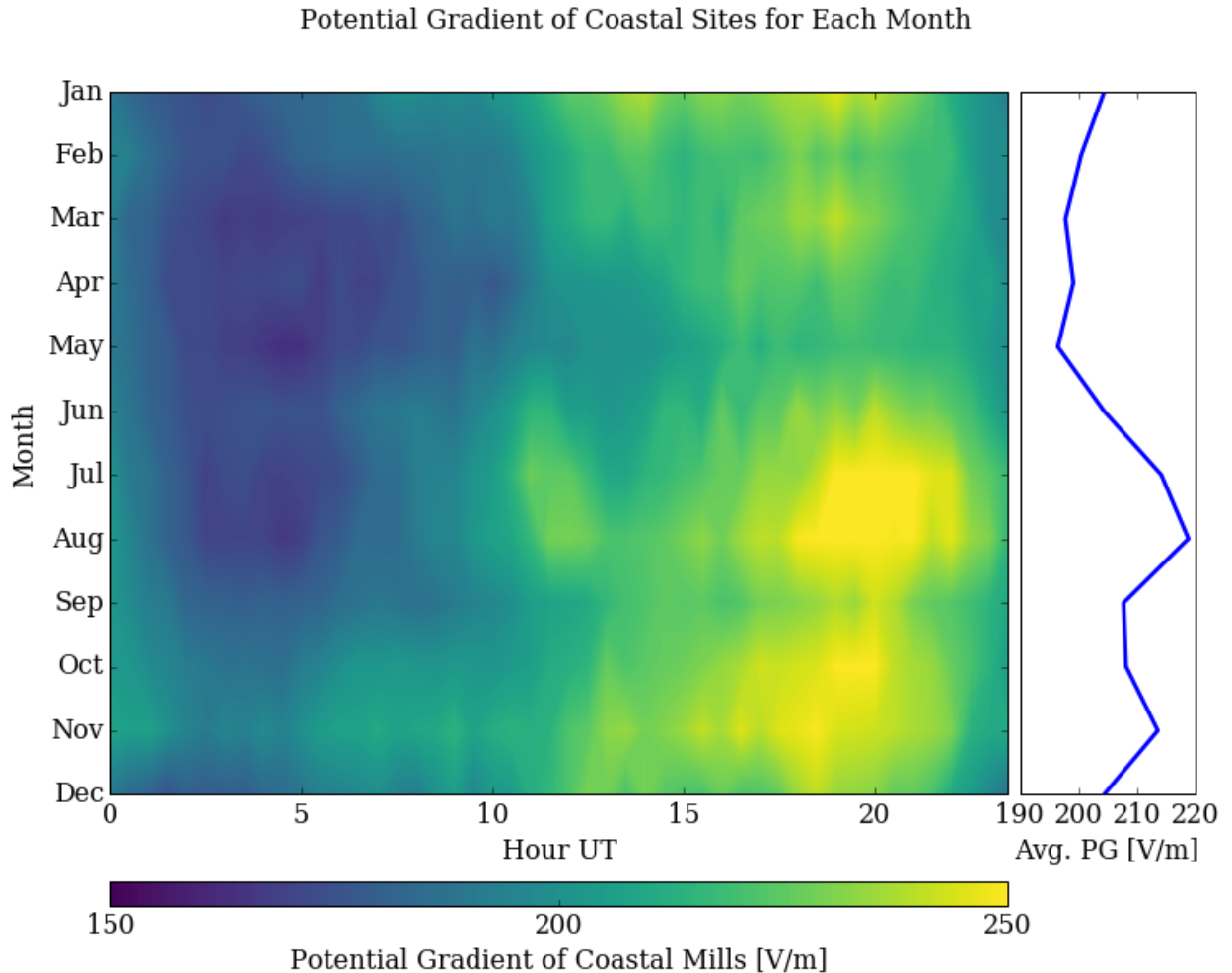


Figure 2.7: The variability in potential gradient over time of day and month of the year. A small 10 V/m variation over the year is seen in the right panel.

There are several possibilities for this small annual variation that is seen in the data. Section 2.4.2 described local influences of sea spray that modify the near-surface electric field by more than 50 V/m. If this local modification has an annual variation that is opposite to the global atmospheric electric field, the signals could destructively interfere with one another reducing the strength of the annual variation in the data. Another possibility is the large occurrence of storms around KSC, which leads to poor fair-weather sampling in the summer months due to the frequency of large electric fields. Therefore, a site with a lower occurrence of electrified clouds and thunderstorms would be a more ideal observation location for assessing an annual variation in atmospheric electric fields. Another possibility for the lack of an annual signal is that there is no annual GEC variation, and that all measurement locations are experiencing an annual local variation with the changing of the seasons causing local fluctuations in the near-surface atmospheric electric field. This discrepancy of the annual and seasonal variation of the atmospheric electric field warrants further investigation of the electric fields from multiple sites over the same long-term periods to determine the differences between the various data sets.

The 18-year KSC data set is large enough to cover around one-and-a-half solar cycles, but greater than 9-year trends are not deducible. Figure 2.8 shows a slight decrease in the signal since 2003. This could be due to the GEC currents decreasing over time or a degradation in the instruments or measurement site over time, as indicated in Markson [2007]. The deduction of long-term trends would benefit from a global site comparison over many years, which would eliminate any instrument degradation or local contamination concerns.

The wavelet analysis showed that there is a significant diurnal variation seen at KSC and a relatively small annual signal, but no other periods had consistent power throughout the data set. A long-term, decreasing trend in the potential gradient was shown in figure 2.8. The lack of a strong annual and seasonal signal, and a weakly decreasing trend in the potential gradient measurements, warrant further investigation in relation to previous authors' findings [Burns, 2005; Burns et al., 2012; Blakeslee et al., 2014].

Potential Gradient of Coastal Sites for Each Year

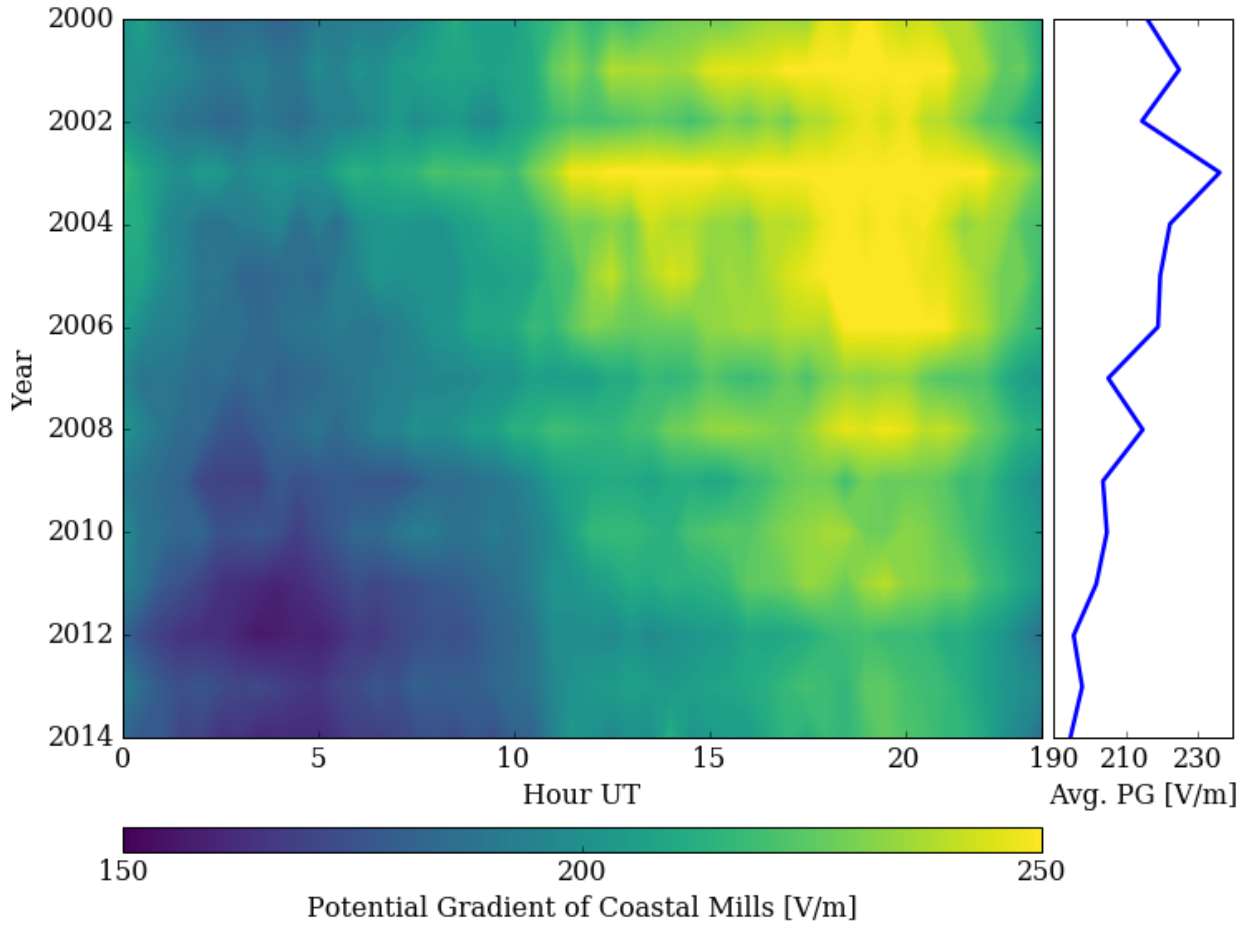


Figure 2.8: The variability in potential gradient over the time of day and year within the data set. The potential gradient has been slowly decreasing since 2003.

2.4.4 Clouds in the GEC

Clouds within the GEC act as resistors and increase the total resistance of the atmosphere. This is due to a reduction of conductivity within clouds caused by the attachment of ions to water droplets that reduce their mobility [Harrison, 2003]. Nicoll and Harrison [2010] launched balloons through layered clouds of large horizontal extent and their measurements show a reduction of conductivity within the cloud of around 1/3. Their balloon measurements also indicated the presence of space charge at the boundaries of the cloud. This space charge developed due to the rapid spatial changes in conductivity between clear and cloudy air rather than by a source, such

as ocean surf, as discussed in section 2.4.2. Their measurements were conducted within the clouds themselves, but no ground measurements of the electric field were related to these findings. This is another example whereby combining the horizontal array of field mills with vertical measurements of electric properties could further advance the findings. To determine the influence of clouds on the near-surface atmospheric electric fields, the long-term data set at KSC and the model simulation from section 4.1 are used to investigate the statistical trends of near-surface electric fields when clouds are overhead.

Local METAR observations from an automated weather reporting system indicating the fraction of cloud cover were obtained at hourly intervals from the shuttle landing strip (airport code KTTS). The different cloud categories correspond to different fractions of the sky covered by clouds given in eighths: clear (0/8), partially cloudy (2/8), scattered clouds (4/8), mostly cloudy (6/8), and overcast (8/8). Taking clear skies to be the baseline electric field, the deviation of other sky conditions with respect to clear skies is determined. Figure 2.9 shows that as the cloud cover increases, the surface electric field reduces in magnitude. However, in the case of fog being present, the magnitude of the electric field increases, which agrees well with previous measurements [Bennett and Harrison, 2009]. In the situation of fog, the electric field measurements can be viewed as being made inside of a local cloud.

To simulate the influence that clouds have on the measured electric field, the model developed in section 2.3 will be used. In this model, a full overcast cloud is placed between 750 meters and 1250 meters, and, separately, a fog layer from zero to 100 meters. Within these clouds, the conductivity is reduced by 1/3 which agrees well with the observations from Nicoll and Harrison [2010]. Figure 2.10 shows a profile of the electric field throughout the column in a standard atmosphere (green), with an overcast cloud (red line) and fog (blue line). The strong enhancement seen in fog, and the weak reduction of the potential gradient due to overhead clouds, agrees with the observations seen in figure 2.9 based on alterations to atmospheric conductivity. The modeling and observational agreement put a realistic limit on the conductivity reduction seen within clouds at no more than 1/10, and draws into question findings of conductivity reductions of more than 1/20 to 1/60 that

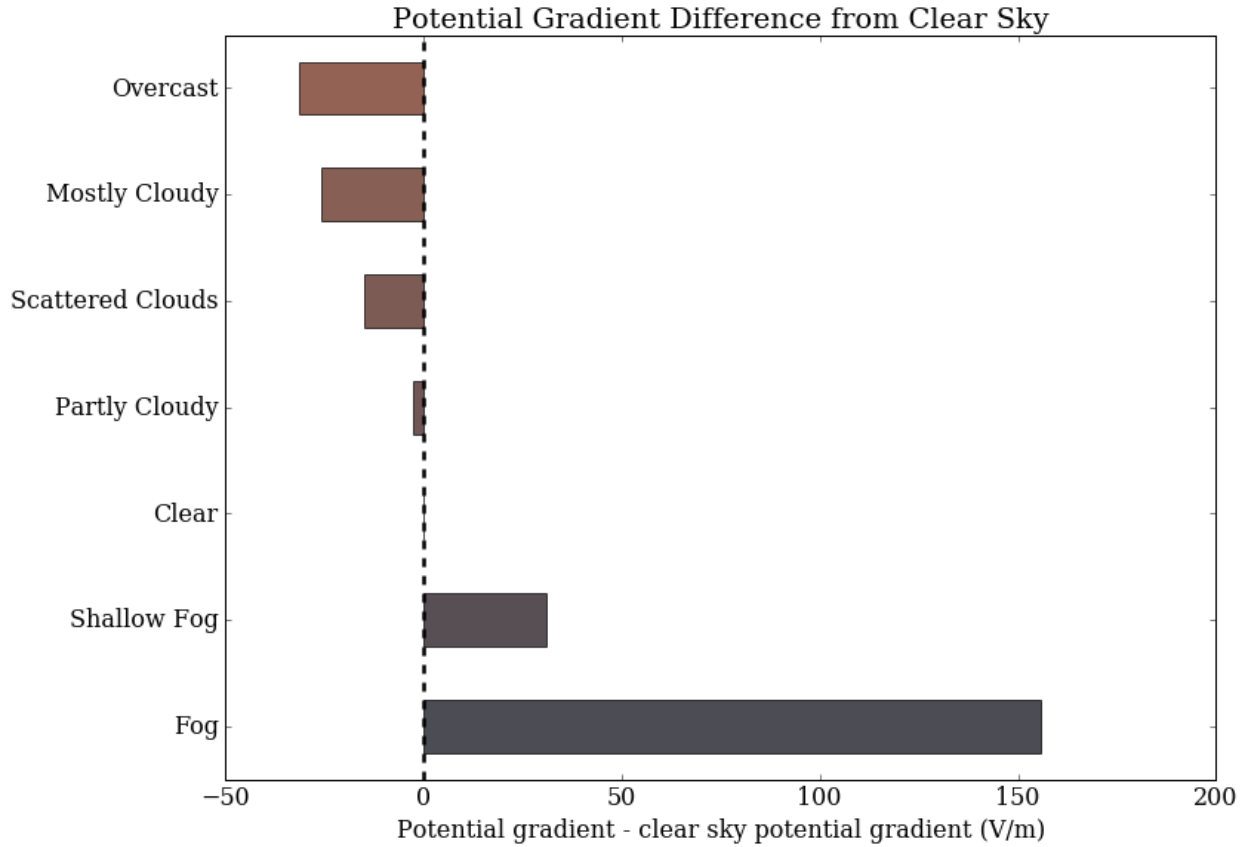


Figure 2.9: Potential gradient deviations due to local cloud cover. Increasing cloud cover overhead causes a reduction in the potential gradient, while a local fog enhances the potential gradient.

were found in the global modeling work of Zhou and Tinsley [2010]. Recent measurements by Nicoll and Harrison [2016] have attributed the large conductivity reduction values used within Zhou and Tinsley [2010] to the shallow transition depth at the edges of clouds that was assumed within that work. In the simplified case where $J = \sigma E$, a reduction in conductivity of 1/10 would lead to a ten-times larger electric field, which is not seen in the KSC data.

Utilizing the model from section 2.3, a reduction in conductivity within clouds is able to explain the reduction in the observed near-surface electric field due to overhead clouds by increasing the column resistance and therefore decreasing the current density within the column. The local conductivity at the surface measurement location is the same, even with an overhead cloud, and therefore, the electric field is decreased by the same amount as the current density is reduced by

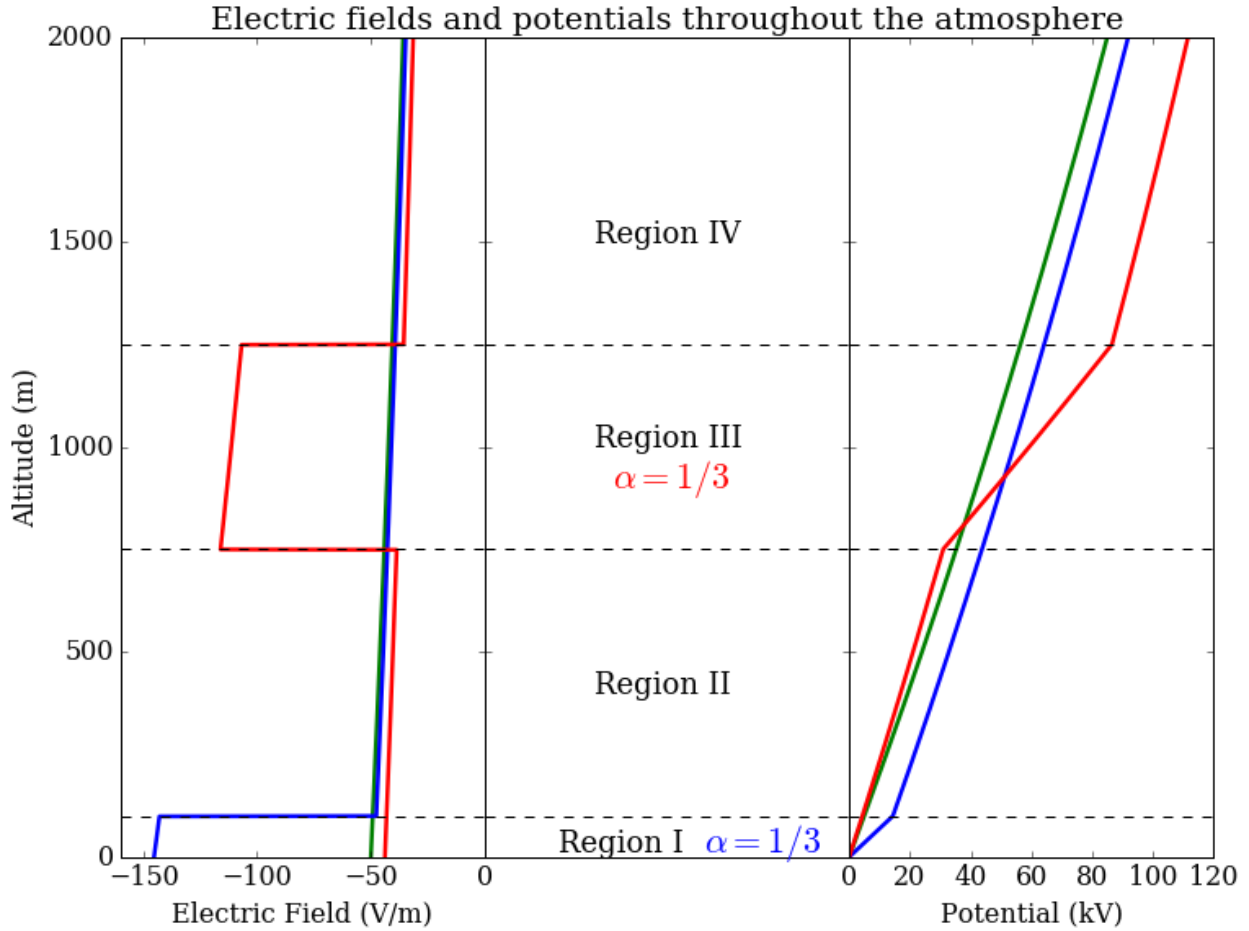


Figure 2.10: The electric field and potential through an overcast cloud (red line) and a low lying fog layer (blue line). The surface electric field is less negative when an overhead cloud is present, while in a fog layer, the electric field is more negative due to the decreased conductivity locally.

the increased column resistance. When fog is present, the local conductivity is modified and one can view the observation as being within the cloud. A layer of fog results in an increased column resistance due to the fog, which reduces the current density in the column. However, the reduced conductivity locally is significantly larger than the reduction of the current density, resulting in a more negative surface electric field.

The influence of clouds on the GEC has primarily focused on the increased total resistance of the atmosphere [Baumgaertner et al., 2014]. However, this analysis shows that overhead clouds modify the local near-surface atmospheric electric fields by up to 30 V/m at KSC, and that a low lying fog can significantly enhance the local electric fields. Therefore, when interpreting near-surface

electric field measurements, one must be cognizant of not only the local atmospheric environment at the surface, but also to what is occurring within the atmospheric column overhead that may modify the column resistance, independent of what other global changes may be occurring in the GEC.

2.4.5 Sunrise enhancement

The near-surface electric field measurements have a distinct diurnal variation that was shown in section 2.4.3. This diurnal variation was attributed to global electric circuit variations. However, figure 2.4 showed a distinct increase in the potential gradient around 12 UT, which is not identifiable in any of the global electric circuit signatures [Williams and Mareev, 2014; Harrison, 2013]. This extra peak at 12 UT corresponds with sunrise at KSC indicating that there could be local factors influencing the global measurement similar to those described by Yaniv et al. [2016]. The enhancement of the atmospheric electric field around sunrise has been investigated by other authors from land based locations around the globe and is known as the sunrise enhancement. The sunrise enhancement is an enhancement of the near-surface atmospheric electric field at local sunrise. This local time influence indicates that different measurement stations throughout the world have these enhancements imposed upon different locations of the universal time diurnal GEC variations. The sunrise enhancement is thought to be produced by a production of local space charge, although the physical mechanism is not fully understood as described within Marshall et al. [1999]. In this study, they raised and lowered a balloon with an electric field meter a few minutes before sunrise to several hours afterwards in the area of the KSC mills. They showed that certain field mill sites around KSC have different strengths of sunrise enhancements and that the sunrise enhancement is not present every single day. The variations seen around sunrise in the near-surface vertical electric field profile appear similar to the space charge profiles developed in section 2.3.3, indicating that some space charge generation mechanism producing a local electric current could be responsible for the sunrise effect.

Investigating a single day or short observational campaigns makes it difficult to discern the difference between the natural GEC variation and the sunrise driven variation. The KSC data set covers 18 years, which is long enough to eliminate variations within the GEC that are found over a single day. The sun rises locally at different times throughout the year at KSC, which means that over a year the time of this local influence will also vary. To investigate the sunrise enhancement, the electric field values were organized into an epoch time defined as the end of civil twilight at KSC. This is the time that the sun's rays will first appear at the site and begin to heat the surface. Figure 2.11 shows the sunrise enhancement of the inland field mills as well as the relative humidity and wind speed at KSC.

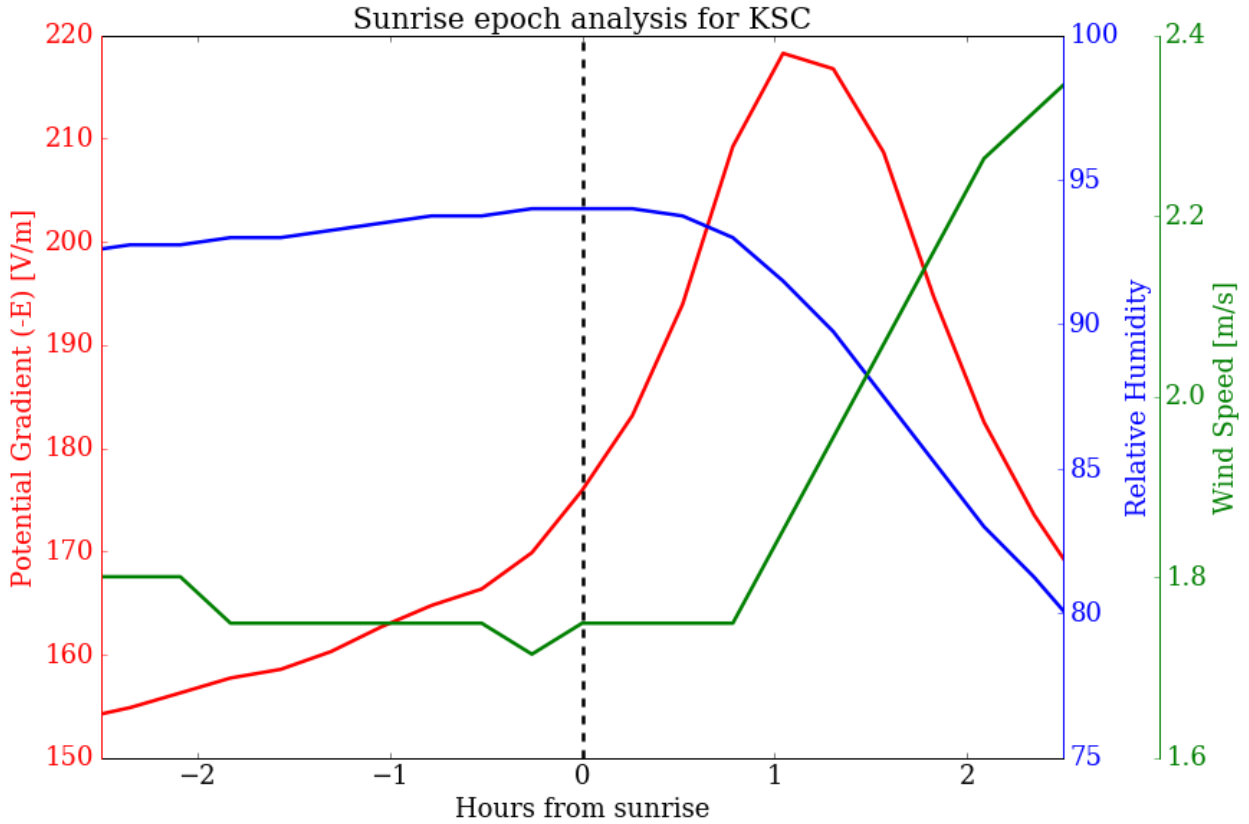


Figure 2.11: Epoch analysis of inland field mills (red), relative humidity (blue), and wind speed (green) at KSC relative to the end of civil twilight. The initial rise in potential gradient appears to start slightly before or right at the end of civil twilight, while the peak in the sunrise enhancement occurs about an hour later.

The maximum in the sunrise enhancement occurs about one hour after the end of civil twilight, but the initial increase in the potential gradient occurs either just before or right when the sun rises. The wind speed and relative humidity are both well correlated with the sunrise enhancement. One possible explanation is that with relative humidities greater than 85%, hygroscopic growth of aerosols occurs, which leads to an increase in the potential gradient due to a decrease in the local conductivity [Silva et al., 2015]. Another theory is that low wind speeds cause an accumulation of space charge near the surface at night that is advected vertically when the sun rises and causes an enhancement in the potential gradient [Marshall et al., 1999]. Figure 2.12 shows the relationship of the potential gradient to the relative humidity and wind speed at KSC. There is a very noticeable sunrise enhancement when the relative humidity is greater than 85%, as well as when the wind speed is less than 2.5 m/s. These two variables are closely related in that when low wind speeds are present there is a high relative humidity, making the separation of these effects difficult.

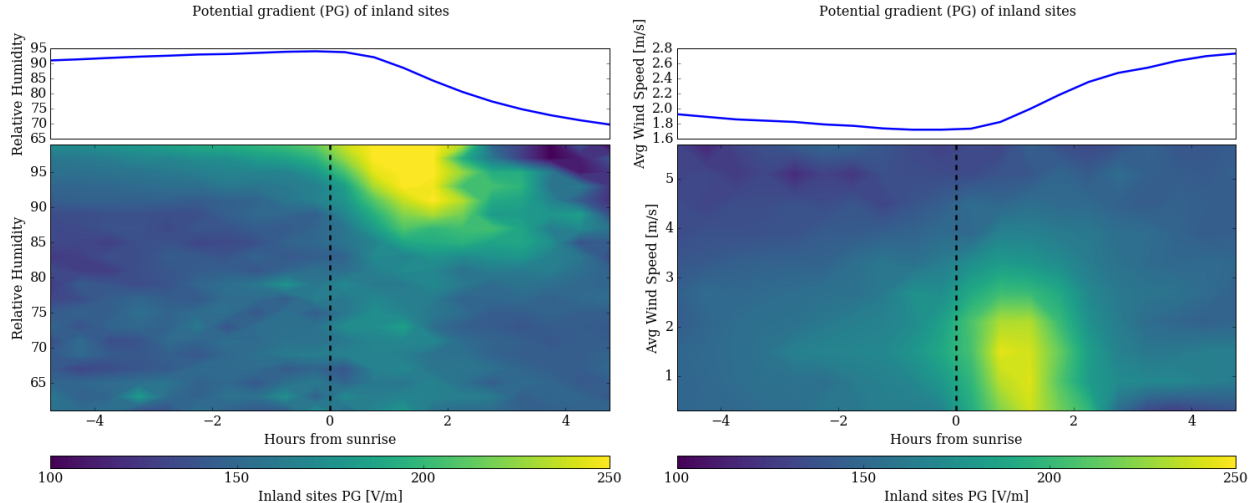


Figure 2.12: Inland field mill measurements showing a significant increase in the potential gradient after sunrise. The left image shows that the sunrise enhancement occurs with relative humidity above 85% and the right image shows that wind speeds below 2.5 m/s are required for the enhancement.

The sunrise enhancement occurs frequently at KSC and produces a strong local time influence on the electric fields. This local influence can cause large deviations from the diurnal GEC variation that must be accounted for when attempting to determine the GEC signal. The relative humidity

and wind speed correlate well with the sunrise enhancement, and several explanations found in the literature warrant further investigation. An attempt to simulate the sunrise enhancement in a laboratory setting where these variables can be controlled would be useful to understand this effect in more detail.

2.5 Summary

The investigation of electric fields in the atmosphere has been rooted in measurements for over 100 years. Within this chapter, data sets from Kennedy Space Center in Florida, and Vostok and Concordia stations in Antarctica were utilized for their fair-weather measurements. Investigating the long-term statistical trends showed that local meteorological properties affect the electric field measurements. The location of field mills close to the ocean showed that the air mass over the ocean blowing over the field mills near the shore leads to differences of more than 50 V/m , compared to field mills further inland, in the measured surface electric fields. An in-depth statistical analysis was carried out to show that local cloud cover and the local sunrise time influence the local electric field measurements as well. Investigation of these local phenomena within the electric field data showed that care must be used when investigating global electric field signatures from a surface electric field measurement. Chapter 3 will discuss the electrical processes that go into the generation of the global electric fields.

Chapter 3

Electrical Processes

To address the four questions posed within this thesis an understanding and description of relevant atmospheric electrical processes is required. Air is generally thought of as an insulator due to its large resistance. Even though air is a great insulator it is not a perfect insulator and there are ions within the atmosphere that are able to move charge from one location to another. Although a minor species in the dynamical system of the atmosphere these ions maintain the electrical nature of the atmosphere. To understand this electrical system in more detail a model that incorporates both the dynamical and electrical system together is imperative because the dynamical forces are stronger than the electrical forces in the atmosphere. The dynamical forces are able to move the ions around, which intrinsically generates local currents through the motion of these ions, and also affects the resistances throughout the atmosphere by changing the number concentrations of the ions. The electrical system can also influence the dynamical system with an extra force term from the electric fields, but these forces are not as powerful and, therefore, the effects are harder to identify. Coupling the dynamics and electrical nature of the atmosphere within a self-consistent model provides a means to observe these different forcing mechanisms in a deterministic way.

The essential process to be evaluated within any electric model is to satisfy the current continuity equation. This accounts for the flow and production/loss of currents within the system. The two driving parameters in solving the current continuity equation,

$$\nabla \cdot \sigma \nabla \phi = S, \quad (3.1)$$

for the potential ϕ are the conductivity, σ , and the source distribution, S . The conductivity of air generally increases exponentially with altitude, following the decreasing density of the atmosphere. There are also perturbations to this exponential profile caused by ion creation and loss processes, which includes clouds and aerosols. These perturbations to conductivity are discussed within Baumgaertner et al. [2013], Zhou and Tinsley [2010], Tinsley and Zhou [2006] and expanded in more detail within section 3.1.

The source distribution within previous global models has relied upon thunder and convective area distributions [Hays and Roble, 1979; Markson, 2007; Mareev and Volodin, 2014] or electrified cloud parameters that relate to the strength of currents produced [Kalb et al., 2016]. For a simplified representation of storms, an electrified cloud will generally have a positive charge center located above a negative charge center. These two charge centers are then represented within the mathematical models as dipole current sources as mentioned by Tzur and Roble [1985]. This dipole current source represents the separation of charge that occurs within a storm cloud. The previous work discussed above will be advanced in section 3.2 to provide a method of integrating realistic local thunderstorms into global models that are not able to resolve individual storms.

To solve for currents and electric fields in the GEC, the full spatial and temporal distribution of the conductivity and source currents within the modeling framework need to be assessed. Several GEC models have been developed in the past to describe different aspects of the circuit that were discussed in chapter 1. Recent model developments have provided better characterization of the electrical connections within the atmosphere by utilizing finer grid resolutions and novel numerical techniques [Odzimek et al., 2010; Zhou and Tinsley, 2010; Kalinin et al., 2014; Bayona et al., 2015]. The work within this thesis builds upon these methods and integrates them into one comprehensive modeling framework. The incorporation of conductivity extends the methodology of Baumgaertner et al. [2013, 2014] by utilizing data and observations where available and two-moment microphysics for the loss of ions. The sources utilized within the modeling extend the methodology of Kalb et al. [2016] by incorporating a dependence upon resistance. All of these variables are incorporated into the same computational framework to use a consistent time step and spatial grid.

3.1 Conductivity

Conductivity represents how easy it is to sustain a conduction current within the atmosphere and has the units of Siemens per meter. A medium can be made more conductive through the introduction of more ions, or by increasing the mobility of the ions that are present in the material. The calculation of conductivity, σ , includes calculating the ion pair concentration n , and the mobility of the ions $\mu^{+/-}$, such that,

$$\sigma = ne(\mu^+ + \mu^-), \quad (3.2)$$

where e is the elementary charge.

To create the ion pairs, highly energetic particles ionize the air. Highly energetic particles include galactic cosmic rays (GCRs), radioactive decays from radon that has been emitted from the ground, and solar proton events. Higher up in the atmosphere the solar photon flux dominates the production of ions and electrons in what is called the ionosphere. Within the global electric circuit this highly conductive region is generally assumed to be a constant potential [Israël, 1970] and used as an upper boundary within models.

Each ionization event can create thousands of ions locally but these ions are close enough together that they will recombine with one another. The ion-ion recombination rate is considered as a loss process within models which reduces conductivity.

The conductivity can also be modified by adjusting the mobility of the particles as well, this includes accounting for ion attachment to clouds and aerosols. When a small ion attaches to a larger aerosol or cloud droplet the mass is greatly increased and therefore the ion becomes much less mobile. To characterize these small-scale (not resolvable within the climate model grid size) perturbations within the circuit, a finite element method (FEM) was used in Baumgaertner et al. [2014]. This allowed for a parameterization of small-scale cloud effects, that are not resolvable on global climate model scales, to account for their influence on the downward return currents.

Incorporating these physical mechanisms to determine the conductivity in the domain allows one to calculate the full 3D spatial and temporal distribution of conductivity utilizing the Community Earth System Model framework with the Whole Atmosphere Community Climate Model, CESM1(WACCM). Calculating conductivity in a physics-based framework allows for the coupling of many different physical and chemical mechanisms, and the investigation of new parameterizations and couplings within the same model.

3.1.1 Ion Production

Ions are produced through highly energetic particles interacting with the neutral particles in the atmosphere to ionize them. The creation of these ion pairs is primarily due to galactic cosmic rays (section 3.1.1.1) and radioactive decay (section 3.1.1.2) within the atmosphere and occasionally highly energetic solar particles from a CME (section 3.1.1.3) that can cause ionization in the middle atmosphere. The production of ions are described in the sections below.

3.1.1.1 Galactic Cosmic Rays

Galactic cosmic rays (GCRs) are high energy particles coming from outside the solar system produced by supernovae [Ackermann et al., 2013]. GCRs are the main source of ionization in the middle atmosphere and have a maximum production rate near 10-15 km [Bazilevskaya et al., 2008]. The charged particles interact with the magnetic fields of the sun and earth. This interaction is able to change the direction of the particles. Therefore there is a variation in GCRs with solar cycle due to the interplanetary magnetic field increasing in strength during solar maximum [Usoskin et al., 2005]. The interplanetary field describes the solar cycle dependence on cosmic ray ionization, but there is also a latitudinal dependence of cosmic ray ionization. This latitudinal influence is due to the non-uniform magnetic field of Earth that preferentially allows different energies of particles into the atmosphere to produce ionization. Earth's magnetic field is therefore able to deflect the GCRs depending on the magnetic rigidity of the particles. The magnetic rigidity, R , of a particle

is defined as

$$R = Br_L = p/q, \quad (3.3)$$

where B is the magnetic field and r_L is the Larmor radius of the particle. This is also equivalent to the momentum, p , over the charge, q , of the particle, indicating that the rigidity is the ability of a particle to penetrate a given magnetic field Herbst et al. [2013]. With Earth's dipole magnetic field, particles can more easily penetrate near the poles and therefore we can define a cutoff rigidity, R_C , where particles under this energy are unable to penetrate Earth's magnetic field. The cutoff rigidity is dependent on the L-shell of Earth's magnetic field, L , as

$$R_C = \frac{\kappa}{L^\alpha}, \quad (3.4)$$

where $\kappa \approx 14.823$ GV and $\alpha = 2.0311$ [Herbst et al., 2013]. The cutoff rigidity on Earth shows that there will be more ionization near the poles from GCRs than near the equator, because the high energy particles are able to penetrate farther into the atmosphere where the same L-shell altitudes are lower than at the equator.

One way to represent these effects in the model, is through a parameterization of ion production. One developed by Tinsley and Zhou [2006] is utilized and implemented in the same manner as Baumgaertner et al. [2013]. The parameterization is a function of altitude, geomagnetic latitude and solar cycle. Table 3.1 shows the values used during solar minimum, with the full complement of values found in Tinsley and Zhou [2006]. The altitudes and ion production rates between the equator and the knee are adjusted based on a scaling of $\sin^4 \theta / \sin^4 \theta_{knee}$, where θ is the geomagnetic latitude and θ_{knee} is the geomagnetic latitude of the knee.

The parameterization works well as an approximation to the solar conditions and allows for the experimentation during different solar minimum and maximum idealized scenarios. But recently, the Coupled Model Inter-comparison Project released a solar forcing data set [Matthes et al., 2016]. This project calculates the historic record of GCR flux from neutron monitor counts at several different latitude locations. These neutron monitor counts are then incorporated into an ionization model that is used to produce a daily file containing the GCR production rates as a

Table 3.1: GCR ion production rate parameterization values during solar minimum [Tinsley and Zhou, 2006].

Level	Equator Altitude	Knee Altitude	Knee Latitude	Equator Ion Production [$cm^{-3}s^{-1}$]	Knee Ion Production [$cm^{-3}s^{-1}$]
z_s	0.0	0.0	50	1.4	2.2
z_a	6.5	9.8	52	13.5	145
z_b	9.0	16.0	58	34	325
z_c	11.0	21.0	60	64	435
z_m	16.0	32.0	63	98	500
Assympotote	∞	∞	63	45	550

Table 3.2: GCR ion production rate equations for any altitude [Tinsley and Zhou, 2006].

Height	Ion Production Rate (q)	Scale Height (s)
$z < z_a$	$q_a \exp((z - z_a)/s_s)$	$s_s = (z_a - z_s)/\ln(q_a/q_s)$
$z_a \leq z < z_b$	$q_b \exp((z - z_b)/s_a)$	$s_a = (z_b - z_a)/\ln(q_b/q_a)$
$z_b \leq z < z_c$	$q_c \exp((z - z_c)/s_b)$	$s_b = (z_c - z_b)/\ln(q_c/q_b)$
$z_c \leq z < z_m$	$q_m \exp(-((z - z_m)/s_c)^2)$	$s_c = (z_m - z_c)/\sqrt{\ln(q_m/q_c)}$
$z_m \leq z$	$q_d + (q_m - q_d) \exp(-((z - z_m)/s_c)^2)$	

function of altitude and geomagnetic latitude. A typical ionization profile during a solar minimum (1998) and maximum (1991) period is shown in figure 3.1.

The GCR flux is dependent on the solar cycle due to the sun's changing magnetic field strength. The GCR flux is anti-correlated with the sunspot number, which is an indication of how active the sun is. Figure 3.2 shows the anti-correlation over the previous century. The impact of the changing flux with solar cycle is most prominent at high geomagnetic latitudes. Viewing the ionization rate over time from three different geomagnetic latitudes shows the distinct variability in this flux at high latitudes while lower latitudes show less variability in figure 3.3.

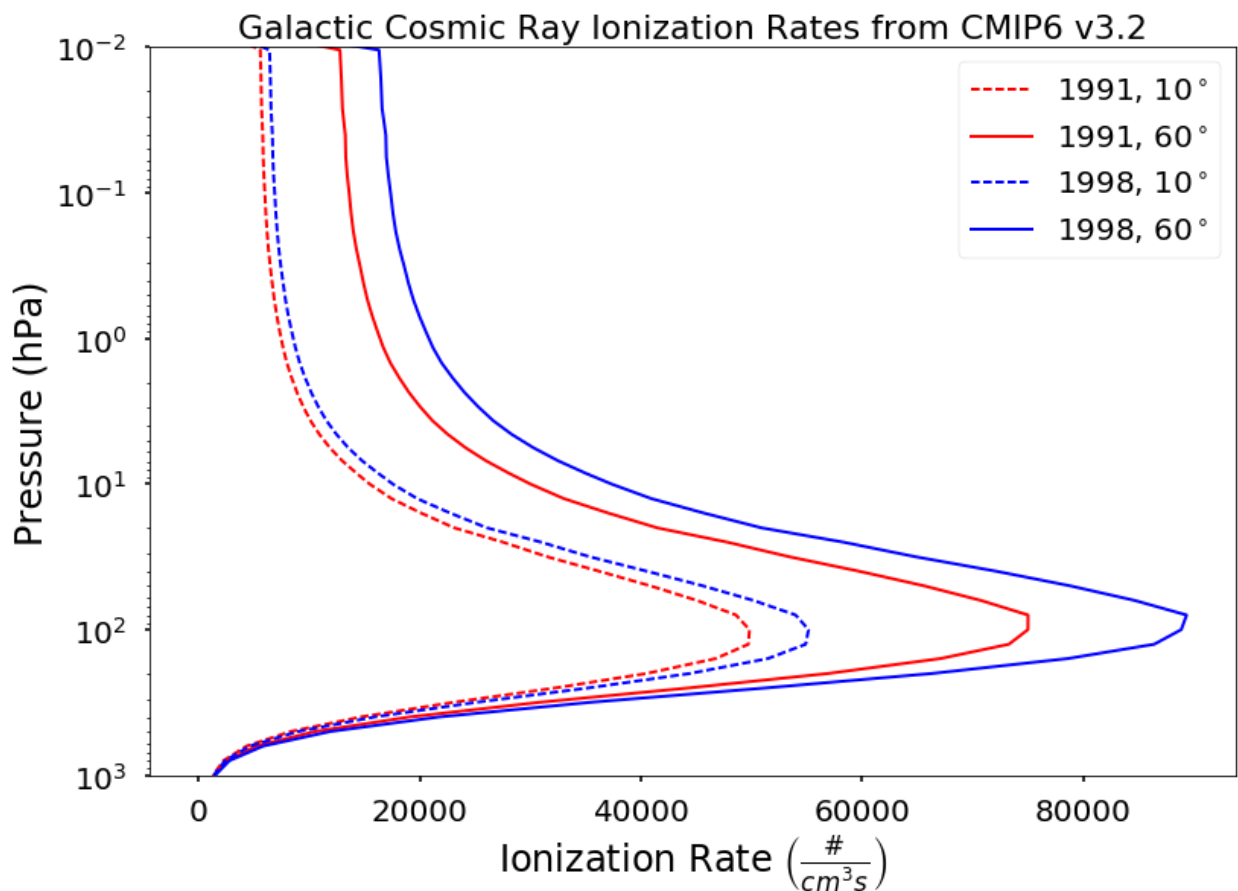


Figure 3.1: Galactic cosmic ray ionization rates for two geomagnetic latitudes and solar minimum and maximum conditions. The ionization rate increases with altitude to a maximum around 100 hPa when it begins to decrease due to the decreasing air density.

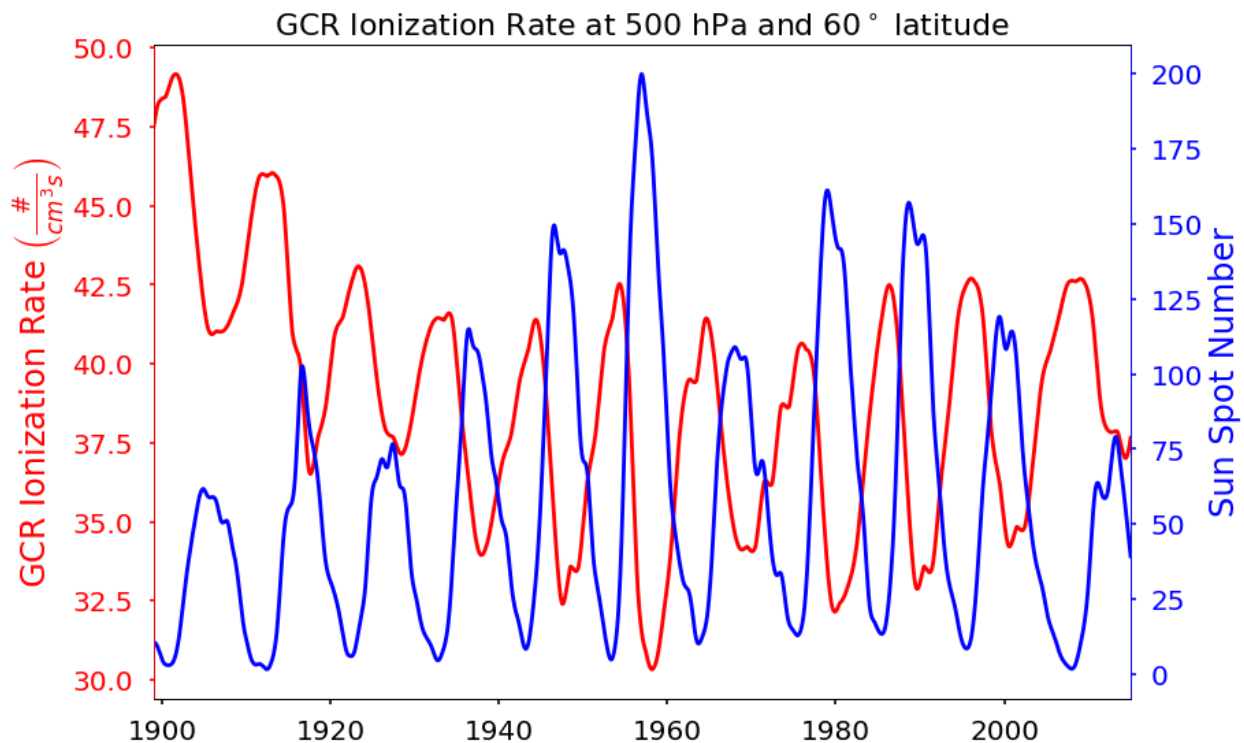


Figure 3.2: Galactic cosmic ray ionization rate and the sunspot number for the previous century. The sunspot number is an indication of how active the sun. The GCR ionization rates are anti-correlated with the sun's activity due to the changing strength of the interplanetary magnetic field.

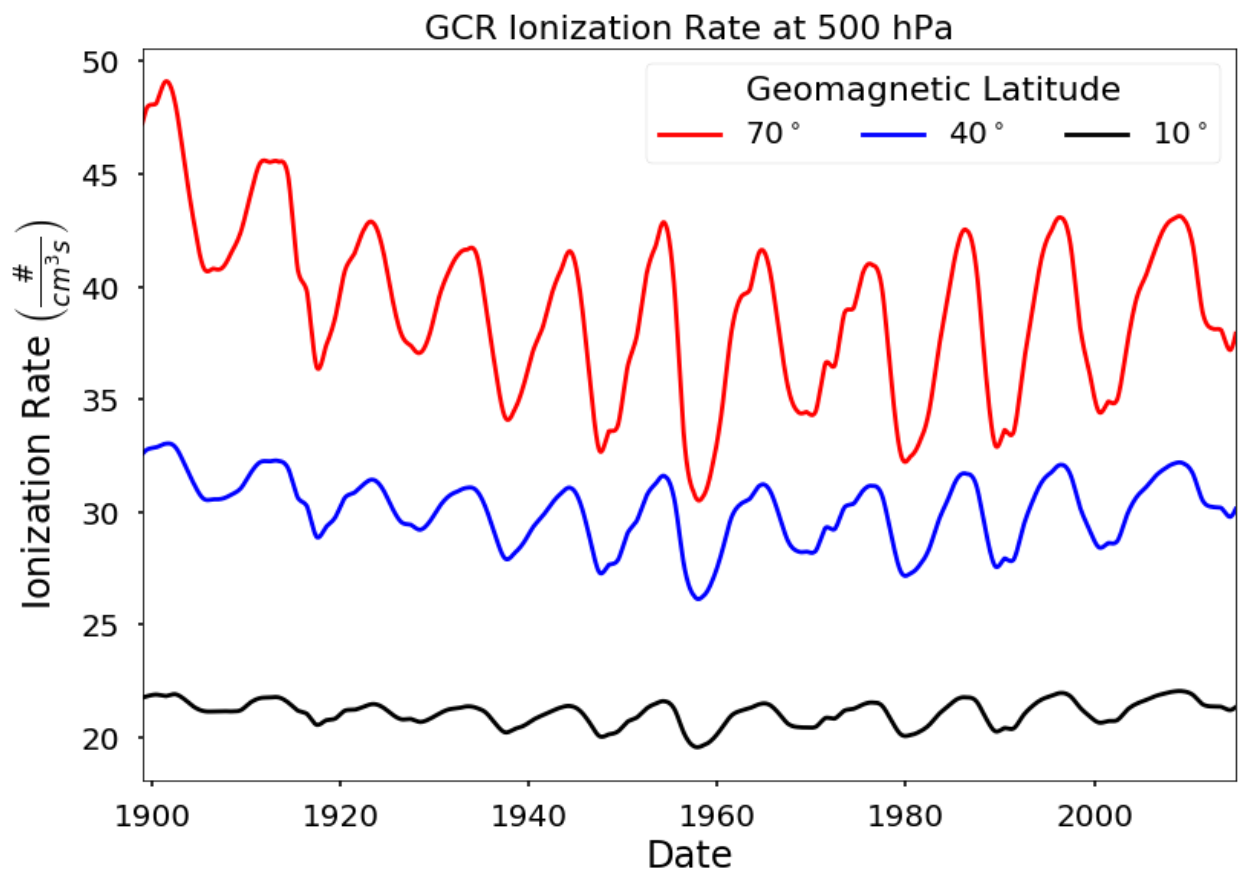


Figure 3.3: Galactic cosmic ray ionization rates for different geomagnetic latitudes over time. The ionization rate increases with geomagnetic latitude, and the variability with the solar cycle also increases at higher latitudes.

3.1.1.2 Radon

The isotope Rn²²² has a half-life of 3.8 days and can stay suspended in the air to be transported over large distances. Radon seeps through the ground in aerosol form, and then decays to produce ion pairs in the atmosphere. A model of the source emission of radon and the decay within the atmosphere is described here. A global map of radon emissions for each month of the year was produced by Schery and Wasiolek [1998]. Figure 3.4 shows the distribution of the radon flux globally in the month of June from this emission profile.

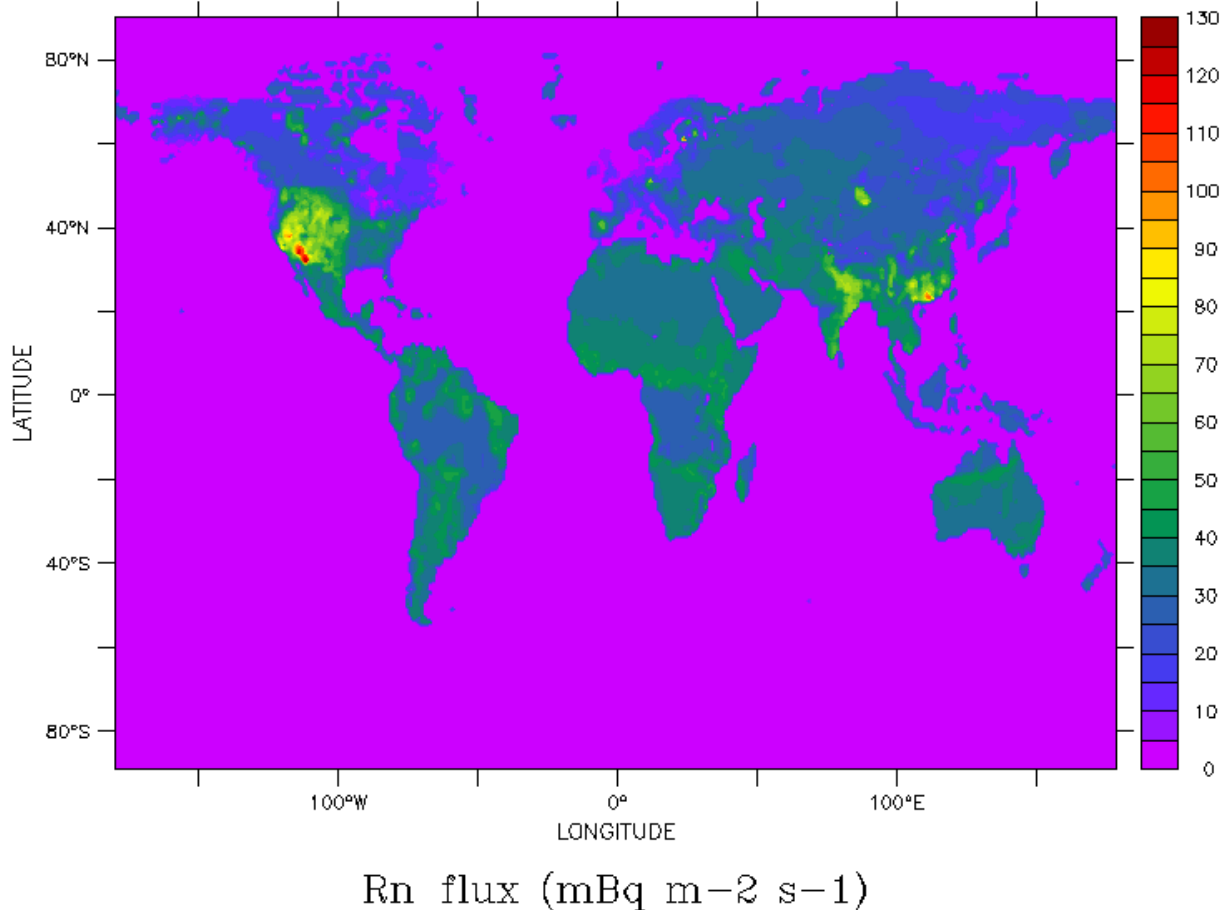


Figure 3.4: The global distribution of radon flux from the ground during the month of June [Schery and Wasiolek, 1998].

Knowing the radon flux from the ground gives the source term for the models, $q_{surface}$. This flux from the ground is able to accumulate, advect and decay within the atmosphere. To model

all of these processes a differential equation representing the radioactive decay and production is solved for the total quantity of material at the end of the time period, $N(t)$.

$$\frac{dN(t)}{dt} = -\lambda N(t) + q; \quad N(0) = N_0, \quad (3.5)$$

where the decay constant $\lambda = \ln 2/t_{1/2}$, and the source term, q , is the flux of material entering the volume. Solving for $N(t)$ gives

$$N(t) = N_0 e^{-\lambda t} + \frac{q}{\lambda} \left(1 - e^{-\lambda t}\right). \quad (3.6)$$

This allows for the production and decay of radon within every grid cell. The atmospheric models then take the quantity of radon within each grid cell and are able to advect the radon throughout the atmosphere. With the models tracking the radon, one can determine the specific activity of radon, $N\lambda$, at any location and therefore determine the number of disintegrations per second and then the ion production rate related by 3.5×10^5 ion pairs per disintegration [Crozier, 1969]. These formulations give the total radon ionization within the model.

To reduce the reliance on external data sets, a more general parameterization of the radon emission from the surface has been developed that is a function of latitude and soil type. The flux of radon from ice-free land surfaces is around 1 atom/cm²/s up to 30° N latitude when it linearly decreases to 0.2 atoms/cm²/s at 70° N latitude [Conen and Robertson, 2002]. The land and snow cover is utilized in the models so that radon emission is accounted for appropriately depending on the surface type. This parameterization takes into account the seasonal dependence of radon emissions within the model itself. The average mass mixing ratio of radon for the months of January and June with this parameterization are shown in figure 3.5.

There has been a recent emphasis on investigating the radon emissions from the soil and determining what those are through measurements. An interesting note here is the radon concentration in the atmosphere is dependent on the transport within the climate models and not solely dependent on the emissions. The radon in the atmosphere can accumulate in certain locations depending on the preferential wind patterns. The incorporation of radon into atmospheric models

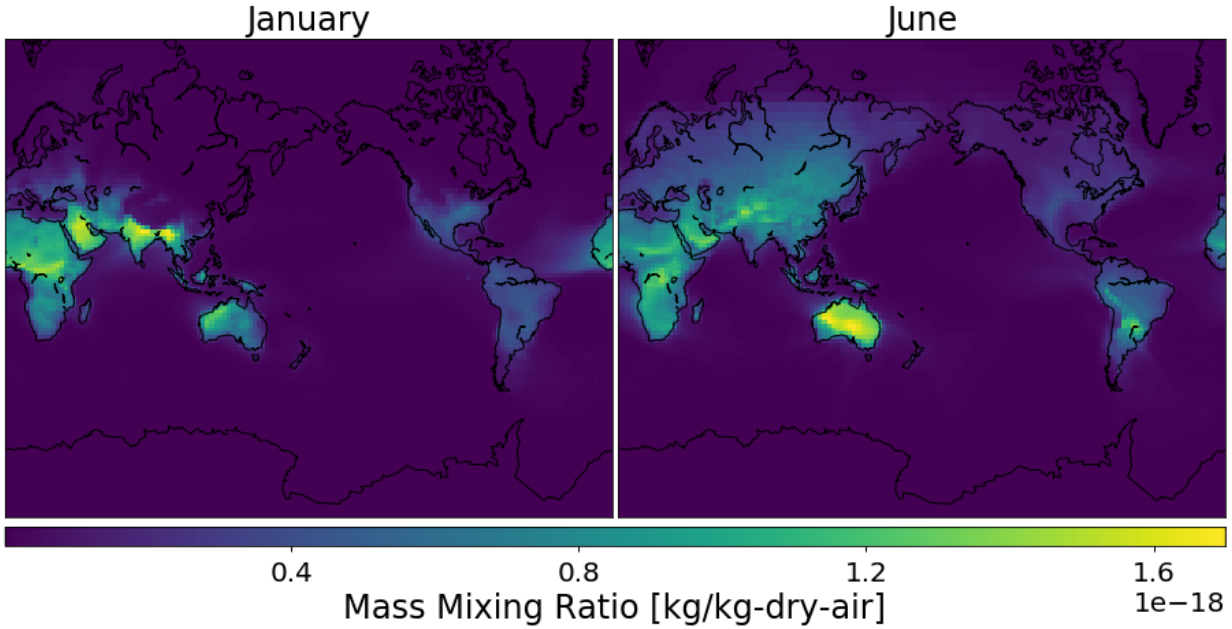


Figure 3.5: Radon concentrations in the lowest model level. The northern hemisphere has larger radon emissions in the summer due to decreasing snow and ice on the surface.

could help explain some differences in the observed variability in concentrations of radon within the atmosphere. With the incorporation of radon into WACCM, other radon emission profiles can be tested to compare with observations and better understand the atmospheric transport of radon in addition to the emanation from the soil.

3.1.1.3 Solar Energetic Particles

Solar flares and coronal mass ejections (CMEs) from the sun release huge amounts of highly energetic particles. If the solar flare or CME are in the right position, the particles can interact with Earth's atmosphere at which point it is called a solar proton event (SPE). When the SPE interacts with the atmosphere it greatly enhances ionization and leads to chemical changes through the production of HO_x and NO_y [Funke et al., 2011; Jackman and McPeters, 2004]. The ionization altitude is strongly dependent on the type, speed and number of precipitating particles, which is available within CESM at a daily resolution [Jackman et al., 2008]. For higher resolution runs the AIMOS (Atmosphere Ionization Module OSnabrueck) data, which has a two hour time resolution

[Wissing and Kallenrode, 2009], has been incorporated into the conductivity framework. SEPs produce very significant perturbations to conductivity in the middle and upper atmosphere, but do not generally have enough energy to make it into the lower atmosphere [Baumgaertner et al., 2013]. The particles in the upper atmosphere modify important chemical reactions, but have little consequence on the GEC because most resistance is within the first 10 km.

3.1.2 Ion Losses

The atmosphere is a highly dynamic region where interactions between different constituents plays a major role in the composition of the atmosphere. Not all ions that are produced stay as their initial free ion-pairs. Ions are able to recombine immediately after being created (section 3.1.2.1). They can also attach to larger aerosol particles (section 3.1.2.2) and cloud water droplets (section 3.1.2.3). These loss processes are described in more detail below.

3.1.2.1 Ion-Ion Recombination

Ions in the atmosphere can quickly recombine after being produced, and this recombination is therefore a loss of ions in the atmosphere. This loss mechanism is dependent on the density and temperature of the atmosphere. To account for this, Tinsley and Zhou [2006] produced a parameterization based on altitude and temperature that fits data from Bates [1982]. The ion-ion recombination rate, α , used in this modeling, in units of cm^3/s , is dependent on altitude in equation (3.7), equation (3.8), and equation (3.9).

$$0 \leq z < 10 \text{ km}; \quad \alpha = 6 \times 10^{-8} \sqrt{300/T} + 1.702 \times 10^{-6} (300/T)^{-1.984} [M]^{-0.451} \quad (3.7)$$

$$10 \leq z < 20 \text{ km}; \quad \alpha = 6 \times 10^{-8} \sqrt{300/T} + 1.035 \times 10^{-6} (300/T)^{4.374} [M]^{0.769} \quad (3.8)$$

$$20 \text{ km} < z; \quad \alpha = 6 \times 10^{-8} \sqrt{300/T} + 6.471 \times 10^{-6} (300/t)^{-0.191} [M]^{0.901} \quad (3.9)$$

$[M]$ is the concentration of air molecules in units of $2.69 \times 10^{19} \text{ cm}^3$ and T is the absolute temperature in K.

3.1.2.2 Ion-Aerosol Attachment

Ions attaching to aerosols that are larger in size effectively slows them down reducing their mobility, which then reduces the conductivity. Natural and anthropogenic emissions have a large variability in size and time of the emissions. Therefore, a realistic treatment of ion attachment to aerosols requires an accurate representation of the size distribution and number density of aerosols in the atmosphere. The Community Aerosol and Radiation Model for Atmospheres (CARMA, version 3.0) [Turco et al., 1979; Toon et al., 1979, 1988] is able to simulate the full aerosol life cycle including nucleation, condensational growth, coagulation, and deposition. The CARMA model is utilized within WACCM-GEC for the representation of aerosols and utilizes 22-36 radii size bins. Within WACCM-GEC a comprehensive size-dependent aerosol distribution is provided from off-line calculations that utilized two CARMA models [Baumgaertner et al., 2013].

The ion-aerosol attachment rate in units of ions/s is calculated as

$$\sum_i \sum_r \beta(r_i) N(i, r), \quad (3.10)$$

where $N(i, r)$ is the number concentration of the aerosol of type i , and r is the particle radius. The coefficient β , which has units of cm^3/s , is a function of particle radius, with different particles types able to have different radii as well. The β coefficients used are from Hoppel [1985] and extended below 10 nm following Tinsley and Zhou [2006], with the radius r given in μm .

$$r \leq 0.01 \mu\text{m} : \quad \beta = 10^{1.243 \log_{10}(r) - 3.978} \text{cm}^3/\text{s} \quad (3.11)$$

$$r > 0.01 \mu\text{m} : \quad \beta = 4.36 \times 10^{-5} r - 9.2 \times 10^{-8} \text{cm}^3/\text{s} \quad (3.12)$$

The loss rate due to different aerosols within WACCM-GEC is produced within Baumgaertner et al. [2013]. The use of CARMA within the code involved utilizing off-line emission scenarios within the model. New versions of CESM have been updated to provide online emissions from volcanoes and other major aerosol sources with realistic amounts and size distributions of these releases. The Modal Aerosol Model (MAM) [Liu et al., 2016] implemented within CESM utilizes these emissions

during a run producing more realistic timing of the events. New versions of WACCM-GEC utilize the MAM 4 bin aerosol model to determine the aerosol attachment rates. The mean attachment rate of ions to aerosols is shown in figure 3.6. This shows that there are significant areas of aerosols over East Asia as well as dust from the Saharan desert that is produced within the model.

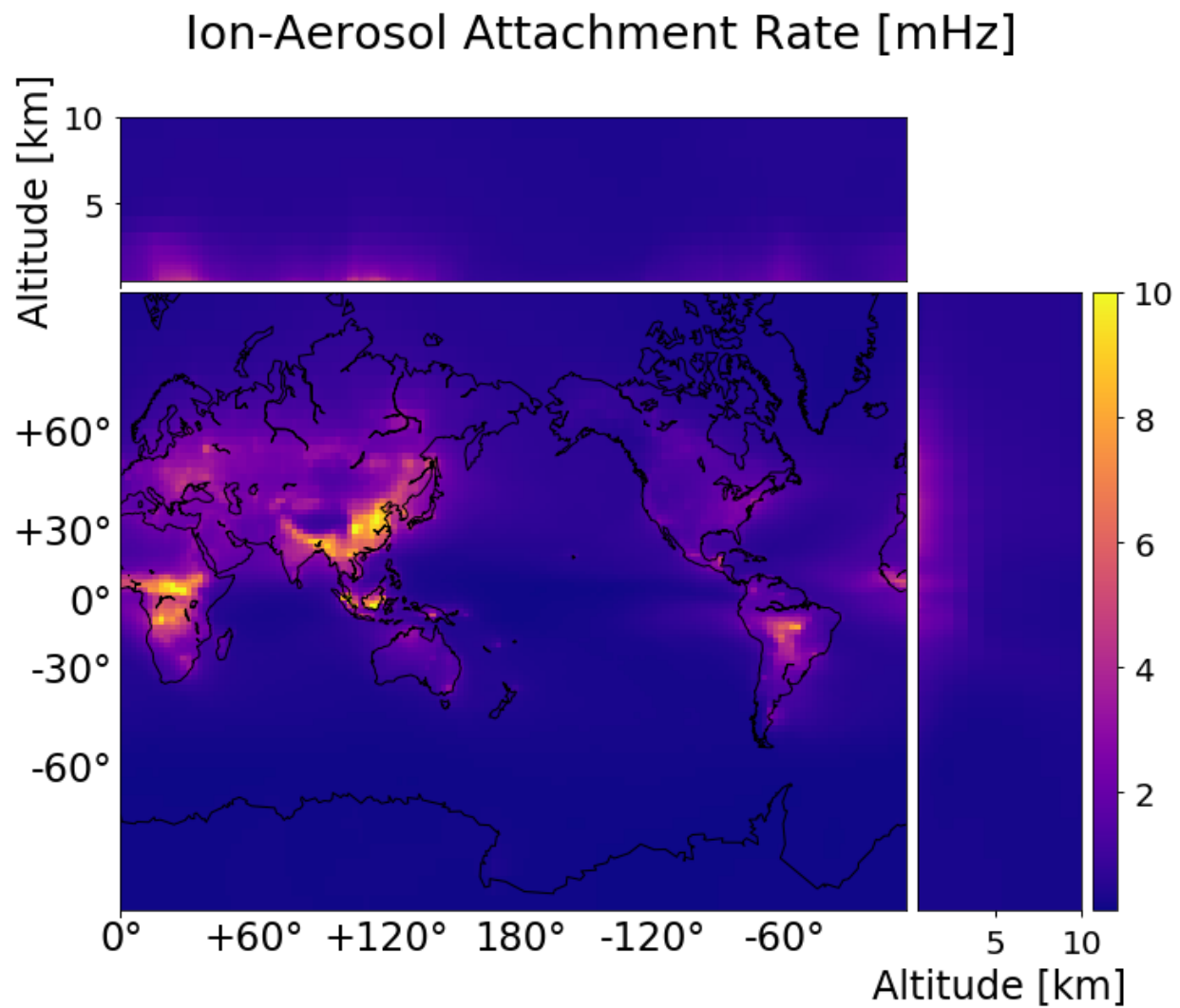


Figure 3.6: Ion attachment rates to aerosols averaged over the entire year. The attachment rate decreases with altitude due to the decreasing density of the atmosphere. There are also noticeable hot spots in east Asia due to biomass burning and pollution.

3.1.2.3 Ion-Cloud Attachment

Ions in the atmosphere can also attach to cloud particles through diffusion and conduction [Pruppacher and Klett, 1997]. The attachment of the ions to cloud drops can be described through the ion diffusivity, D , droplet concentration, N_i , and the droplet radius, r_i through the following equation

$$4\pi D \sum_i N_i r_i, \quad (3.13)$$

where the ion diffusivity is

$$D = \frac{\mu k T}{e}. \quad (3.14)$$

Within CESM a two-moment microphysics scheme is implemented [Morrison and Gettelman, 2008]. The two-moment microphysics determines the number density and size distribution within each grid cell where the size distribution, ϕ , is represented by a gamma function

$$\phi(D) = N_0 D^\mu \exp^{-\lambda D} \quad (3.15)$$

where D is the diameter, N_0 is an intercept parameter, λ is a slope parameter and $\mu = 1/\eta^2 - 1$ is the spectra shape parameter with η being the relative dispersion radius determined by the measurements and parameterization given in Martin et al. [1994]. The equation for η used in CESM is

$$\eta = 0.0005714 N_c'' + 0.2714 \quad (3.16)$$

with N_c'' the local cloud droplet concentration in $1/\text{cm}^3$. Within CESM the local cloud droplet concentration, N'' , and local mass mixing ratio, q'' are calculated and the spectral parameters for the distribution gamma distribution in equation (3.15) are

$$\lambda = \left(\frac{\pi \rho N'' \Gamma(\mu + 4)}{6 q'' \Gamma(\mu + 1)} \right)^{(1/3)} \quad (3.17)$$

$$N_0 = \frac{N'' \lambda^{\mu+1}}{\Gamma(\mu + 1)} \quad (3.18)$$

where Γ is the gamma function. Taking moments of equation (3.15) and rearranging gives the effective radius, r_{eff} , of the droplets within the grid cell

$$r_{eff} = \frac{\Gamma(\mu + 4)}{2\lambda\Gamma(\mu + 3)}. \quad (3.19)$$

Utilizing these distributions within the cloud attachment equations produces a spatially and temporally varying ion attachment to clouds. Figure 3.7 shows the ion attachment rate to clouds averaged over an entire year. The southern ocean has many persistent clouds that are evident in the attachment rates. The incorporation of aerosols and clouds acts to increase the total resistance of the atmosphere.

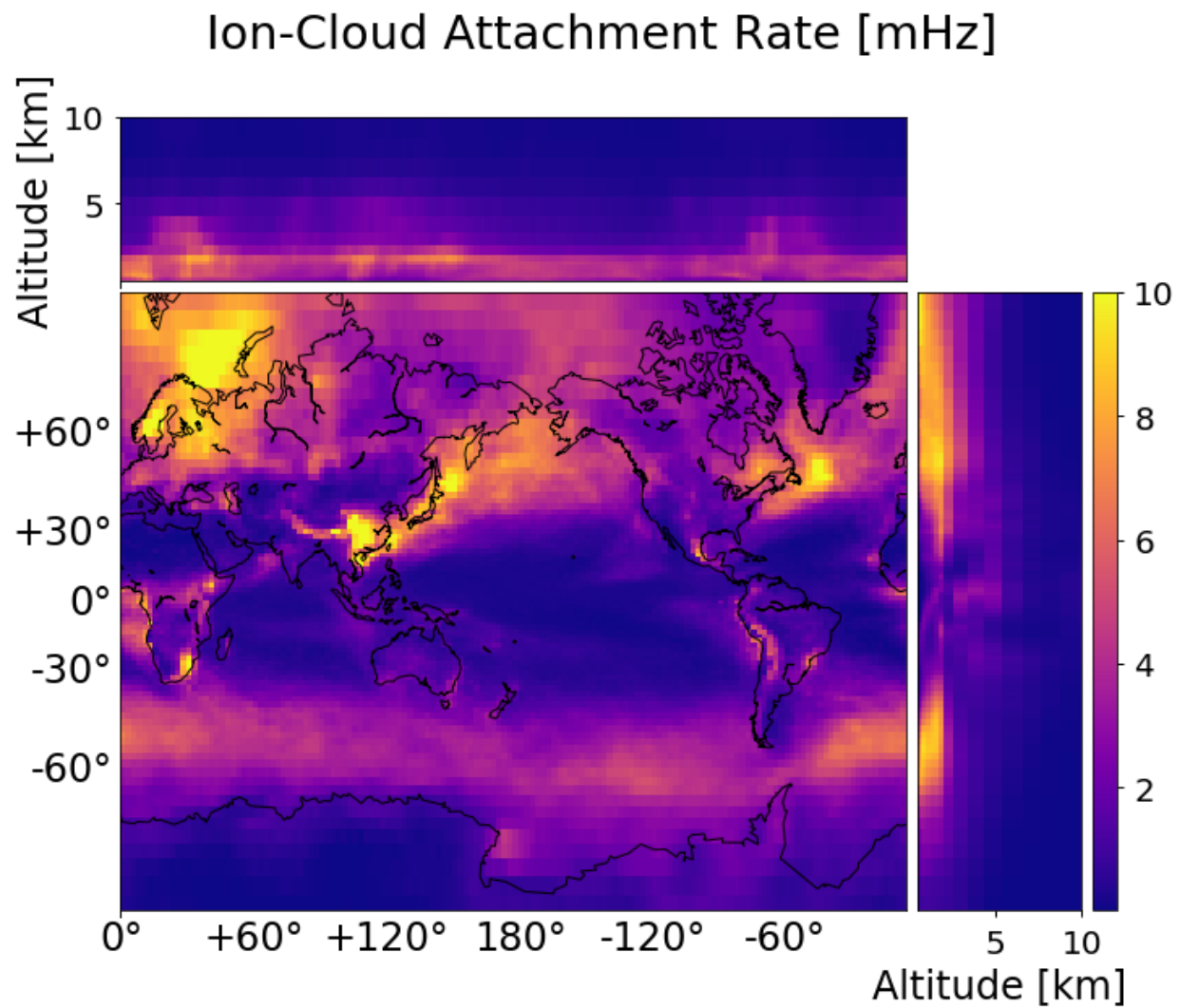


Figure 3.7: Ion attachment rates to clouds averaged over the entire year. The attachment rate decreases with altitude due to the decreasing density of the atmosphere. There are noticeable concentrations of clouds in the mid latitudes of both the southern and northern hemispheres.

3.1.3 Ion Concentration

The conductivity of the atmosphere is dependent on the total ion concentration from equation (3.2). The total ion concentration, n is calculated from the total ion production, q , discussed in section 3.1.1 and loss mechanisms discussed in section 3.1.2. The losses due to recombination from section 3.1.2.1, and the losses due to aerosols and clouds in section 3.1.2.2 and section 3.1.2.3 are utilized in the following equation

$$\frac{dn}{dt} = q - \alpha n^2 - \left(\sum_i \sum_r \beta(r_i) S(i, r) - 4\pi D \sum_r N_r A_r \right) n. \quad (3.20)$$

Where q is the sum of all ion production rates given in units of ions/cm³/s, α is the recombination rate discussed in section 3.1.2.1, $\sum_i \sum_r \beta(r_i) S(i, r)$ is the ion attachment to aerosols in units of 1/s discussed in section 3.1.2.2, and $4\pi D \sum_r N_r A_r$ is the attachment of ions to water droplets in units of 1/s discussed in section 3.1.2.3.

Assuming steady state for the system, $\frac{dn}{dt} = 0$, equation (3.20) becomes a quadratic equation that can be solved for the total ion concentration, n ,

$$n = \frac{\sqrt{4\alpha q + \left(\sum_{i,r} \beta(r_i) S(i, r) + 4\pi D \sum_r N_r A_r \right)^2} - \sum_{i,r} \beta(r_i) S(i, r) - 4\pi D \sum_r N_r A_r}{2\alpha}. \quad (3.21)$$

With the total concentration of ions known, the remaining unknown in the conductivity equation is the mobility of the ions. Mobility is calculated using a "reduced mobility" experimentally determined in clean air, μ_0 following Tinsley and Zhou [2006]

$$\mu = \mu_0 \frac{P_0}{P} \frac{T}{T_0}. \quad (3.22)$$

P_0 and T_0 are for STP at 1013 hPa and 273 K respectively. The value μ_0 used in this work is 3.3 cm² V⁻¹ s⁻¹ which is the sum of the positive and negative ion mobilities. With mobility and ion concentration calculated, equation (3.2) can be used to determine the conductivity. The conductivity in the atmosphere with all of the factors discussed in the previous sections generally follows an exponential distribution with a notable exception near the surface due to radioactivity making the atmosphere more conductive. Figure 3.8 shows the typical exponential distribution from

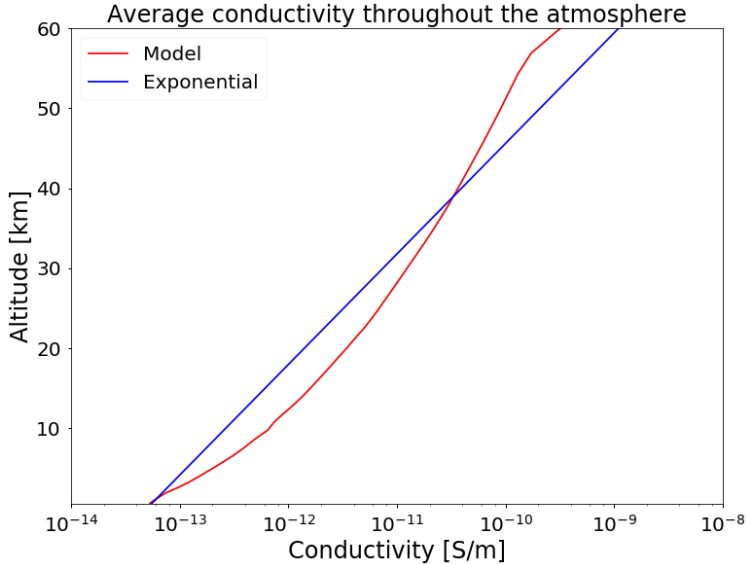


Figure 3.8: Average conductivity throughout the atmosphere from an exponential distribution (blue) and from the WACCM-GEC model (red).

equation (2.9) in red alongside the average model produced conductivity in red. The curves both generally follow the exponential nature of atmospheric density and an increasing conductivity with height. However, there is more variation with the model due to the significant production and loss mechanisms described earlier.

3.1.4 Cloud Current Convergence/Divergence

One of the problems with climate models is their large grid sizes. Therefore, resolving clouds can be difficult or impossible. This means that only a general cloud fraction is known at each location within the model, rather than describing what size and thickness the clouds have. Previously, fair-weather clouds were accounted for with the use of the parallel resistor law [Tinsley and Zhou, 2006; Baumgaertner et al., 2013] and simply reducing the column resistance by the relative cloud fraction assuming parallel resistors. This assumes that the potential at the tops of the clouds are all the same, and that current is unable to flow around the clouds. Figure 3.9 demonstrates the different approaches to modeling current flow through and around clouds [Baumgaertner et al., 2014].

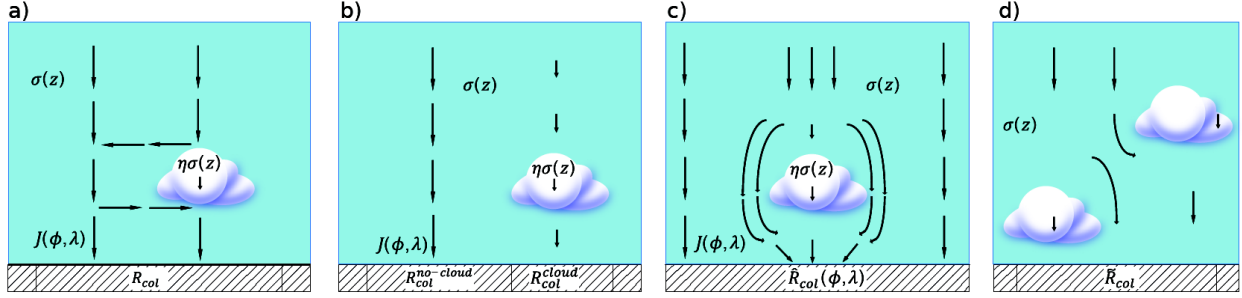


Figure 3.9: Schematics of cloud modifications of conductivity and column resistance. Arrows denote current direction and the current density magnitude in a qualitative sense. (a) Single cloud, with current mainly flowing around the cloud as assumed in the small cloud approximation. (b) Single cloud, only allowing for vertical currents as assumed in the large cloud approximation. (c) Current divergence/convergence around the cloud, and “effective column resistance” as a function of latitude and longitude, employed for the Poisson approach. (d) Model grid column with cloud fraction and Poisson approach column resistance \tilde{R}_{col} [Baumgaertner et al., 2014].

To determine how clouds can modify the current flow a Finite Element model was developed. This model, described within section 3.1.4.1 and Baumgaertner et al. [2014], demonstrated that up to 20% error in the total global resistance can be introduced without considering the converging and diverging currents around clouds. Many different size and shapes of clouds were modeled to obtain a parameterization to input into global models based on the cloud cover fraction. Figure 3.10 and figure 3.11 illustrate the current convergence and divergence around a cirrus and stratus cloud respectively demonstrating the influence of altitude on the currents.

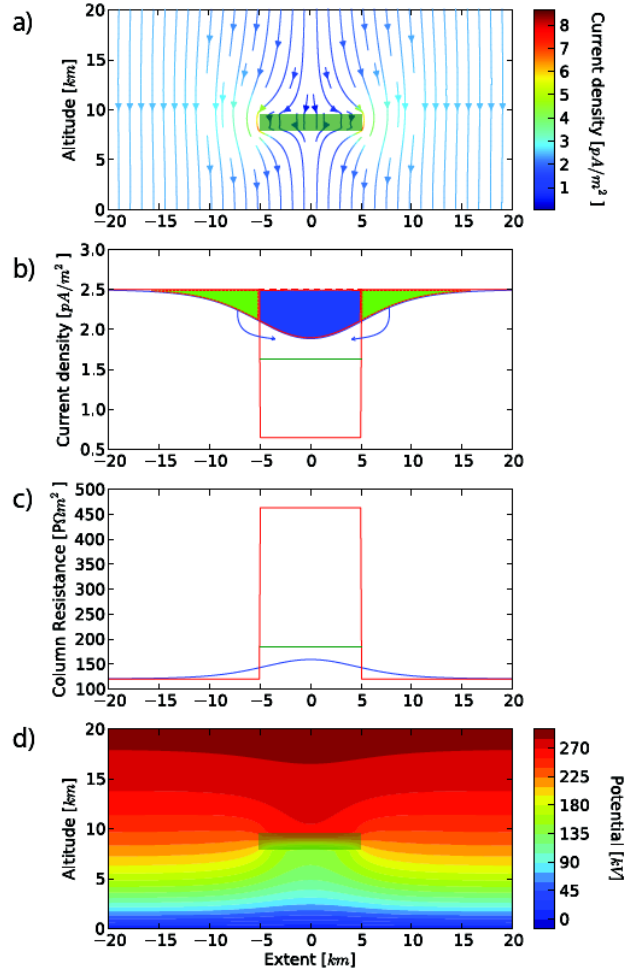


Figure 3.10: (a) current streamlines and total current density around a cirrus cloud (indicated by the green box) with a diameter of 10 km, located between 8 and 9.5 km altitude. (b) Model air-to-earth current density (blue), restricted to vertical currents only (red), and mean effective cloud current density (green). (c) Effective column resistance \hat{R}_{col} (blue), column resistance for considering vertical currents only R_{col} (red), and mean effective cloud column resistance \hat{R}_{col}^{cloud} (green). (d) Potential difference distribution [Baumgaertner et al., 2014].

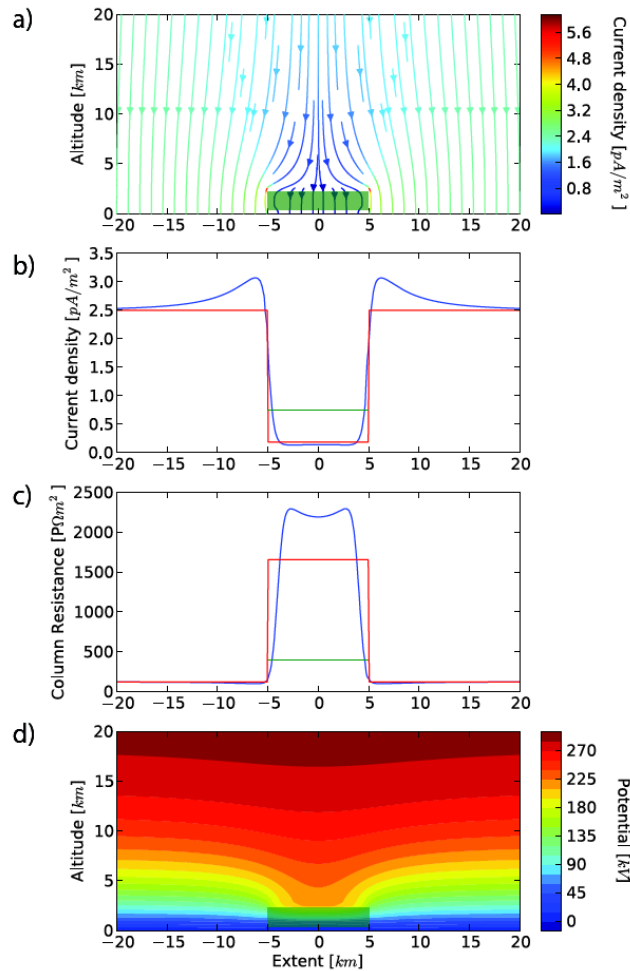


Figure 3.11: As Figure 3.10 but for a stratus cloud between 0.5 and 2.5 km altitude [Baumgaertner et al., 2014].

3.1.4.1 Finite Element Cloud Model

A finite element model formulation is created to represent small scale clouds that are not able to be represented within climate models. The finite element formulation requires a variational form of the partial differential equation. Incorporating boundary conditions to the variational form, the problem can be written as:

$$\begin{aligned} -\nabla \cdot [\sigma \nabla \Phi] &= S \quad \text{in } \Omega, \\ \Phi &= \Phi_E \quad \text{on } \Gamma_E, \\ \sigma \nabla \Phi \cdot n &= 0 \quad \text{on } \Gamma_L \text{ and } \Gamma_R, \end{aligned} \tag{3.23}$$

where Γ_E is the earth boundary, and a Dirichlet boundary condition is implemented with Φ_E , the fixed potential of the earth. Γ_L and Γ_R represent the left and right boundaries of the domain where the current is expected to be vertical far away from any clouds. For the top boundary of the ionosphere, Γ_I , a Neumann boundary condition can be chosen:

$$\nabla \Phi \cdot n = 0 \quad \text{on } \Gamma_I. \tag{3.24}$$

Alternatively, it is possible to use a Dirichlet boundary condition:

$$\Phi = \Phi_I \quad \text{on } \Gamma_I. \tag{3.25}$$

For the GEC cloud simulations presented in the next section we specify a fixed potential and define the sources S to be zero.

The solution is obtained over the domain Ω where σ varies exponentially in height, and within Ω_C (the cloud) $\sigma_c = \eta \sigma$, where η is a constant.

The variational form of Poisson's equation solves for $\Phi \in V$, where V is a suitable function space, such that

$$a(\Phi, v) = L(v) \quad \forall v \in V, \tag{3.26}$$

and

$$\begin{aligned} a(\Phi, v) &= \int_{\Omega \setminus \Omega_C} \sigma \nabla \Phi \cdot \nabla v dx + \int_{\Omega_C} \sigma_c \nabla \Phi \cdot \nabla v dx \\ L(v) &= \int_{\Omega} S v dx \end{aligned} \tag{3.27}$$

where integrals over the Γ_L and Γ_R boundaries would appear in $L(v)$ if they were non-zero.

This formulation was implemented in the Fenics Python program [Logg et al., 2012] to obtain the potential and current distribution throughout the domain.

With the current densities known throughout the domain, one can integrate over the lower boundary to determine the total current

$$I_{tot} = \int_{\Gamma_E} -\sigma \nabla \Phi ds. \quad (3.28)$$

Using the total current flowing out of the domain with a known potential applied provides a solution for the total resistance within the domain using Ohm's law, $V = IR$. This model was run for many different widths and heights of clouds to provide a parameterization that can be utilized within the global models to account for the convergence and divergence of currents around clouds that are not able to be represented within large grid sizes. Figure 3.11 and figure 3.10 show the solution for two different widths and heights of clouds representing a stratus and cirrus cloud respectively.

3.2 Current Sources

Thunderstorms and electrified shower clouds are the sources of current to the GEC that maintain a potential difference between the ground and ionosphere [Wilson, 1921]. Through various electrification processes such as precipitation-based charging, clouds can become electrified. In particular, the non-inductive charging mechanism that involves ice-ice collisions in the presence of supercooled liquid water is thought to contribute significantly to cloud electrification [Takahashi and Miyawaki, 2002; Saunders, 2008]. Storm kinematics as well as gravitational size sorting invoke charge separation that leads to the development of larger scale charge regions inside these clouds. This charge separation can be represented as a dipole current source that drives the current within the atmosphere.

Implementing current sources within a global model requires the investigation of how an individual storm will interact with neighboring grid cells and the vertical conductivity variations

within a column. Section 3.2.1 discuss the leakage current between neighboring grid cells and section 3.2.2 analyzes the amount of current contributing to the GEC from dipole current sources.

3.2.1 Storm Horizontal Extent

Each electrified cloud generally only covers several kilometers in the horizontal, while grids within climate models can be more than 100 km. This means it is difficult to resolve individual storms within climate models, unless they are extremely large convective systems. The FEM model developed in section 3.1.4.1 and Baumgaertner et al. [2014] is utilized to model the currents from a cloud and how they interact with neighboring grid cells.

A simple dipolar charge separation was introduced into the finite element model run at a resolution of 0.5 km to produce two volume current densities, +1 A /m³ at 10 km and -1 A /m³ at 5 km. Assuming an exponential conductivity profile of the form

$$\sigma = \alpha\sigma_0 \exp z/z_0, \quad (3.29)$$

where σ_0 is 5.E-14 S/m, z_0 is a scale height of 6 km [Roble and Hays, 1979b], z is the height above ground, and α is a conductivity scaling parameter. With a 100 km horizontal domain, and a 5 km charge separation distance, a current of 0.272 A exiting the domain is produced. Emulating a model grid boundary where there is a decrease in conductivity ($\alpha = 1/50$) introduced away from the source cloud, the total current reaching the top domain does not change significantly, but the distribution and location of those currents within the grid does. This tests the situation in climate models where two vastly different conductivities occur in adjacent grid cells and a net vertical current from each grid cell is assumed to be unaffected by the adjacent cell. This situation could occur when aerosols are produced in a single column, but not strongly advected into adjacent columns.

Two representative current distributions are shown in figure 3.12, using the standard exponential profile current distribution for $x > 0$. For $x < 0$ it shows a conductivity reduction of 1/50 away from the source region. These two cases were run separately using the FEM model and

plotted side by side for comparison. To further illustrate the point, the top and bottom boundary current densities are plotted in figure 3.13. The bottom current densities are nearly identical due to the sharp fall off from the source, but the top current densities show that there is more current entering the ionosphere in the lower resistance region than the higher resistance region, while the total integrated current remains the same. If one is not concerned with the high fidelity distribution of source currents, then one only has to determine the total current input to the circuit for determining the top potential.

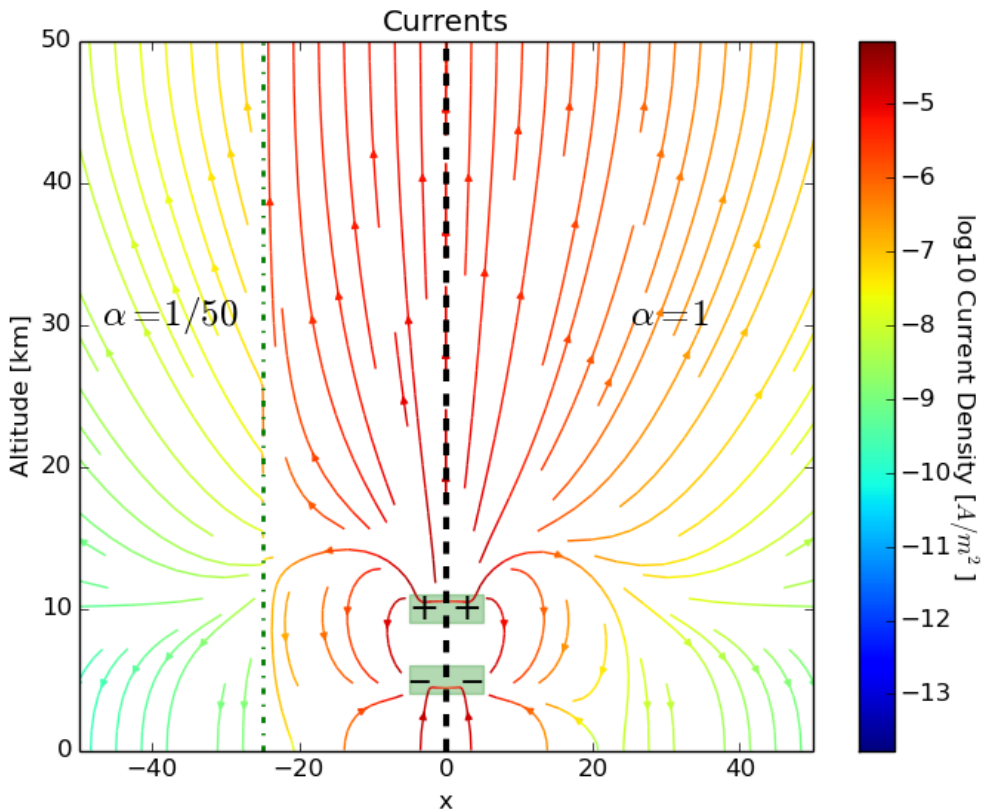


Figure 3.12: Current produced from two separated charge centers. Two separate simulations were run, one $x > 0$ where the conductivity follows an exponential profile, and another, $x < 0$ where the conductivity was reduced by a factor of 50, 25 km away from the center. The distribution of the currents are different between the two simulations due to the increased resistance to current flow away from the source.

The small-scale FEM model has shown that the total vertical current within a grid cell is unaffected by the conductivity variations in the neighboring grid cells. However, the total current

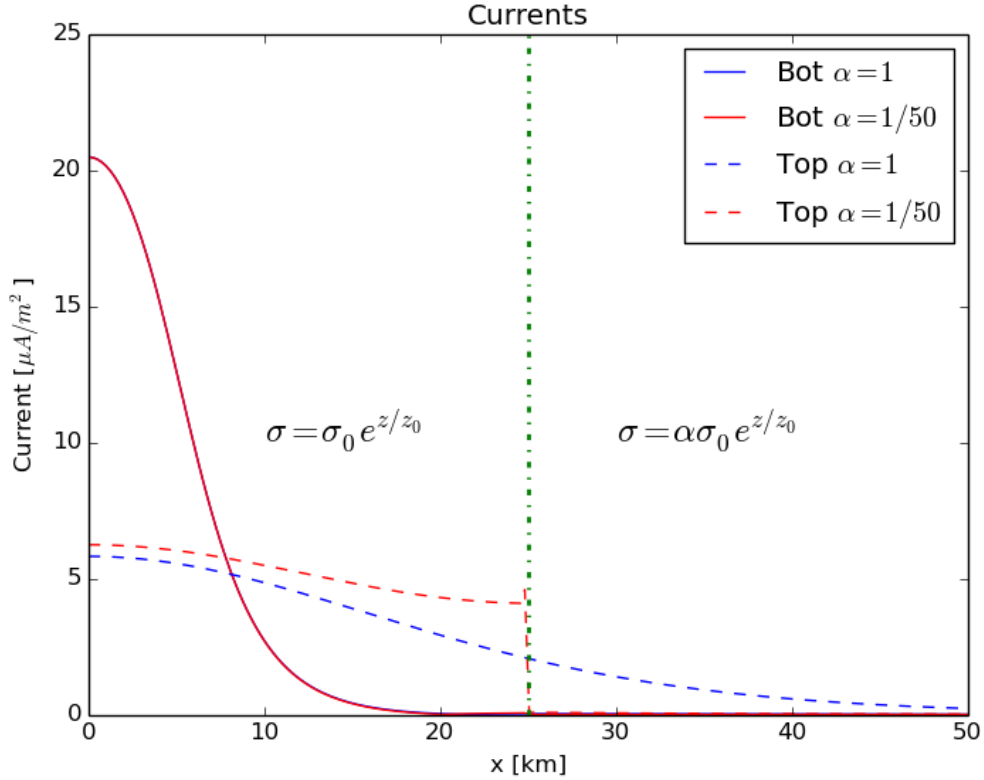


Figure 3.13: Amplitude of the current leaving the boundaries of the domain. When a conductivity change is introduced away from the sources ($\alpha = 1/50$), the location of the current exiting the domain changes, but not the integrated amount of current. Across the top boundary (dashed lines) the red curve shows a higher current density when $x < 25$ km and then a sharp decline due to the increased resistance in the region outside of this. The dashed-blue curve shows a continuous path as there is no conductivity perturbation introduced.

input to the GEC is highly dependent on the distribution of conductivity within the local vertical column.

3.2.2 GEC Current Contribution

To determine the amount of current contributing to the GEC previous studies have utilized an electric circuit analog. This electric circuit can be driven by either a current source or voltage source [Slyunyaev et al., 2015] with resistors above and below the storms. To determine the electric fields in an arbitrary conductivity medium, a one dimensional analytic model is developed within this section. The model determines the potential, ϕ , throughout the domain by maintaining current continuity throughout the domain

$$\nabla \cdot \sigma \nabla \phi = 0. \quad (3.30)$$

To determine the amount of current leaving the column 0 V potentials are applied at the bottom, z_0 , and top, z_3 , boundaries. There are also two other interfaces within the domain due to the dipole current source. The dipole current is represented by $-I_{dipole}$ at z_1 and $+I_{dipole}$ at z_2 . This produces a 3 region model that can have any arbitrary conductivity distribution within each region, $\sigma(z)$. At each interface the current and potential are continuous, which at z_1 becomes

$$\phi_1 = \phi_2 \quad (3.31)$$

$$\sigma_1 \nabla \phi_1 = \sigma_2 \nabla \phi_2 - I_{dipole}. \quad (3.32)$$

Solving equation (3.30) for the potential gives solutions of the form

$$\phi = C_1 \int \frac{dz}{\sigma(z)} + C_2. \quad (3.33)$$

Realizing that $\int \frac{dz}{\sigma(z)}$ is just the resistance as a function of z , $r(z)$, the equation can be rewritten as

$$\phi = C_1 r(z) + C_2. \quad (3.34)$$

Using this form for the potentials in all regions and applying a continuous potential condition across the boundaries between regions, the first interface becomes

$$C_1 r_1(z_1) + C_2 = C_3 r_2(z_1) + C_4. \quad (3.35)$$

There is no depth in region 2 yet, so $r_2(z_1)$ is 0, and $r_1(z_1)$ is just the total resistance within region 1, denoted by a capital R , which simplifies to

$$C_1 R_1 + C_2 = C_4. \quad (3.36)$$

The current continuity across the interface, evaluated at z_1 , becomes

$$\sigma_1 C_1 \frac{dr_1}{dz} = \sigma_2 C_3 \frac{dr_2}{dz} - I_{dipole}. \quad (3.37)$$

The resistance in each region was defined as the integral of $1/\sigma$, therefore the derivative of resistance becomes $1/\sigma$, which simply cancels with the conductivity in front of the coefficients leaving

$$C_1 = C_3 - I_{dipole}. \quad (3.38)$$

After applying these equations at each interface and both boundaries the potential only depends on the strength of the current dipole, I_{dipole} , and the total resistances within each domain, R . Solving for the potential in each region yields

$$\phi_1 = I_{dipole} R_{ratio} r_1(z) \quad (3.39)$$

$$\phi_2 = I_{dipole} R_{ratio} \left(R_1 - \left(\frac{R_1 + R_3}{R_2} \right) r_2(z) \right) \quad (3.40)$$

$$\phi_3 = I_{dipole} R_{ratio} (r_3(z) - R_3), \quad (3.41)$$

where R_{ratio} is the ratio of resistances between the centers of the dipole to the entire column.

$$R_{ratio} = \frac{R_2}{R_1 + R_2 + R_3} \quad (3.42)$$

A representative illustration of a simple dipole current source with strength $I_{dipole} = 1000$ A and the centers located at 5 km and 10 km is shown in figure 3.14. There are two different conductivity distributions shown, an exponential conductivity following equation (2.9) (blue) and a constant conductivity within each region (blue) that gives the same total resistance within each region as the exponential conductivity. Due to the different conductivities within each region the electric fields will be different, however the total current leaving the domain is the same.

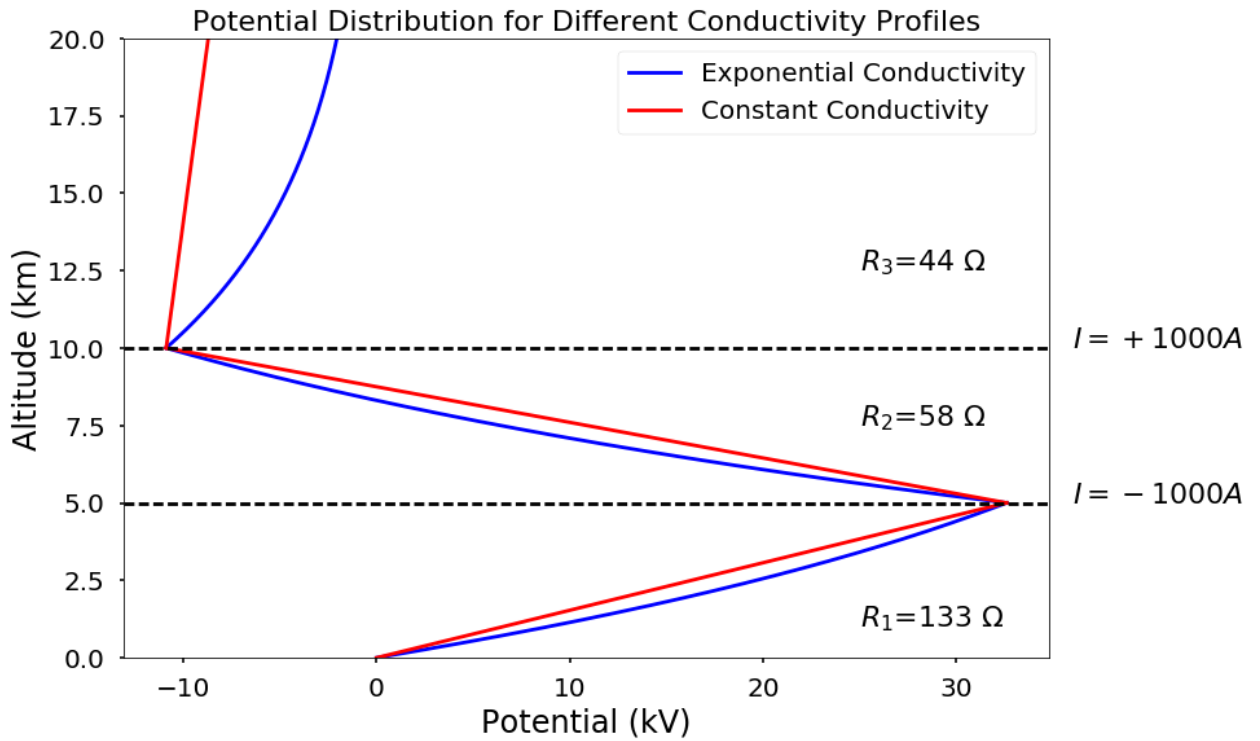


Figure 3.14: The potential distribution from different conductivity distributions within each region. The blue curve has an exponential conductivity profile defined by equation (3.29) while the red curve has a constant conductivity within each region to produce the same total resistance as the exponential distribution. The potentials follow different paths indicating that the electric fields within the domain would be different in each situation, but the total current contributing to the GEC remains the same and is dependent on the ratio of resistances between the domains.

Calculating the total current leaving the domain and contributing to the GEC, I_{GEC} , depends entirely on the ratio of resistances within the column

$$I_{GEC} = I_{dipole} R_{ratio}. \quad (3.43)$$

The ratio can be thought of as an efficiency factor for the current to contribute globally. Increasing the resistance between the dipoles will put more current into the GEC, while increasing the column resistance will reduce the amount of current contributing to the GEC.

Previous work on calculating the current contribution to the GEC focused on parameterizing these source currents based on related cloud parameters [Kalb et al., 2016]. These parameters are related to electrification processes that in turn relate to the magnitude of the currents produced by electrified clouds, I_{dipole} . In that analysis it is implicitly assumed that the dipole resistance is the same for all storms and therefore $I_{GEC} \propto I_{dipole}$. This implicit assumption is able to be relaxed within global models where the conductivity is known throughout the domain and new parameterizations for the generation of the dipole current strength can be investigated. The implications of using the resistance ratio in a global model will be discussed in section 3.2.3.

3.2.3 Global Distribution

Kalb et al. [2016] derived storm currents of electrified oceanic and continental clouds identified by Liu et al. [2010a], based on Tropical Rainfall Mission Measurement (TRMM) satellite precipitation radar measurements, and assigned respective mean currents from Mach et al. [2010, 2011] to these storms. This produced a global current map between $+/- 35^{\circ}$ latitude (the observational domain of the TRMM satellite) shown in figure 3.15. This map was then compared to the total current map produced with model-based cloud parameters and correlations between the model parameters and global conduction currents were developed [Kalb et al., 2016]. Several model parameters that relate to charging mechanisms within storms were investigated, which include convective updraft mass flux, ice water path, and convective precipitation rate. All of the investigated model parameters showed skill at predicting conduction currents within the model.

The convective precipitation rate, that Kalb et al. [2016] identified with strong correlations to the current strength, is used to generate the dipole current strength within the model. The convective precipitation rate averaged over a year is shown in Figure 3.16. There are higher rates

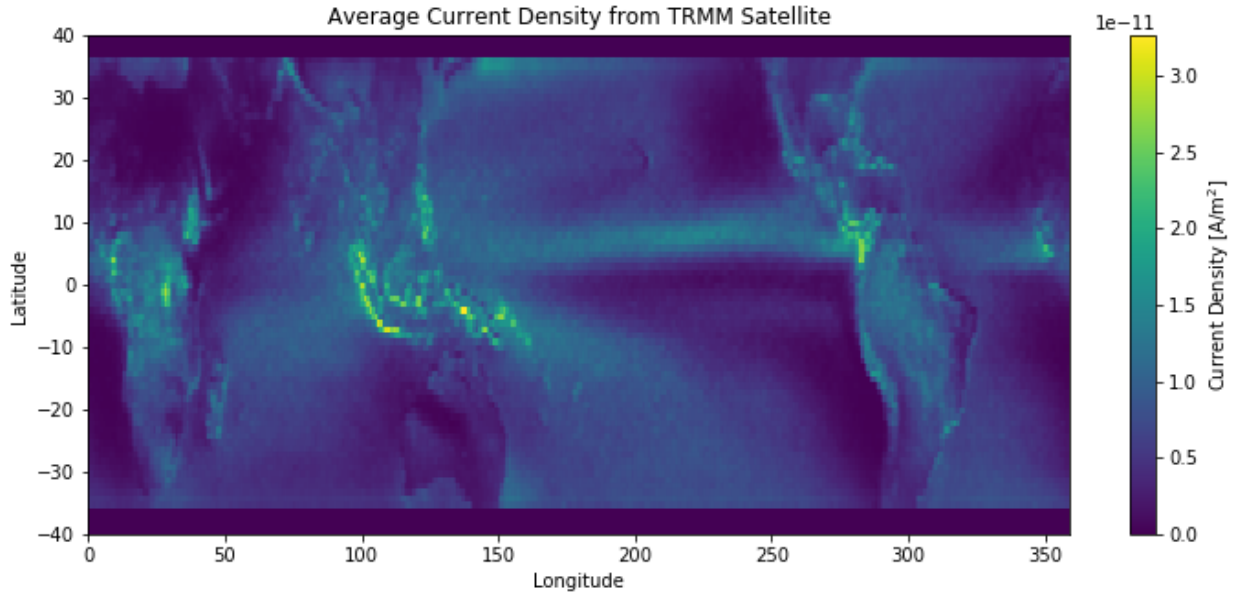


Figure 3.15: The mean estimated current densities from the TRMM satellite after applying mean currents from storm overflights [Kalb et al., 2016].

of convective precipitation in the low latitudes indicating higher dipole current strengths will be generated near the equator.

The convective precipitation rate is utilized to generate a dipole current strength. Equation (3.44) shows how the factor, $C_{current}$, to go from convective precipitation rate, $PRECC$, to current, I_{dipole} is used. With $C_{current}$ equal to $2.5 \times 10^8 \text{ A}/(\text{m/s})$ and the storm efficiencies derived in equation (3.42), the model produces an average total global current within the GEC of 1200 A, which agrees well with previous models and estimates [Hays and Roble, 1979; Williams and Mareev, 2014].

$$I_{dipole} [\text{A}] = PRECC [\text{m/s}] \times C_{current} \left[\frac{\text{A}}{\text{m/s}} \right] \quad (3.44)$$

The surface distribution of convective precipitation alone is not enough to determine the GEC current, I_{GEC} , unless the resistance ratio is assumed uniform throughout the atmosphere. The discussion in section 3.2.2 describes how a vertical profile of resistivity needs to be obtained from the models to determine the resistance ratio. The convective updraft mass flux [Zhang, 1995] and temperature of the grid cell are utilized to determine the depth of the mixed-phase region of

Convective Precipitation Rate [mm/hr]

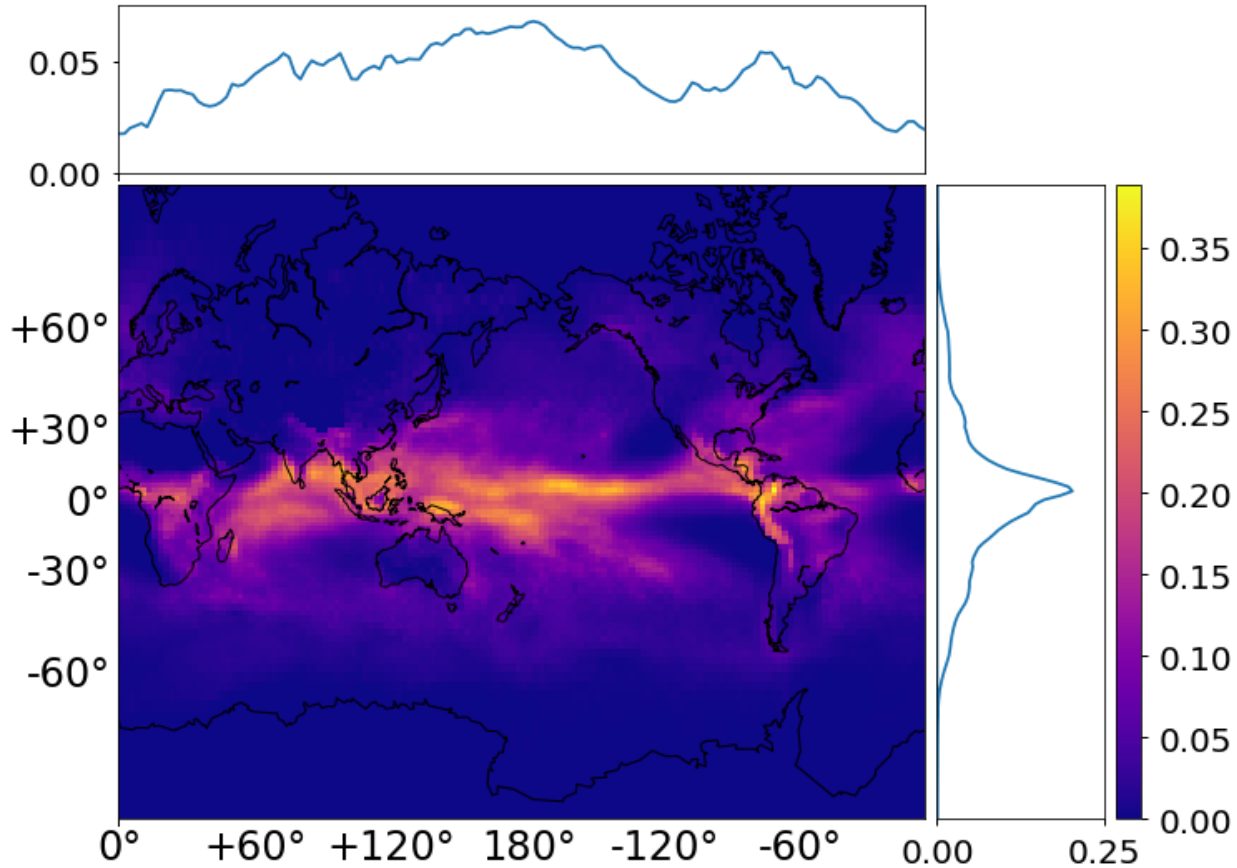


Figure 3.16: The mean convective precipitation rate over a year. There is more convective precipitation near the equator than at higher latitudes.

the storm. These parameters are all related to the charging mechanisms identified earlier where there is a convective updraft in mixed-phase regions of clouds generating a charge separation. In this work, charge generation occurs if there is convective mass flux present and the temperature is between 0 °C and -50 °C, which is a temperature range identified as important in charge generation [Kalb et al., 2016]. This formulation based on convective updraft mass flux and temperature gives the depth of the mixed-phase region of the storm and allows for the calculation of the GEC current

discussed in section 3.2.2. The dipole resistance, R_2 , is calculated within the model based on the following summation and conditionals

$$R_2 = \sum \frac{dz}{\sigma} \quad \text{if : Convective Mass Flux [kg/s] > 0 and } -50 < T [\text{°C}] < 0. \quad (3.45)$$

After calculating the dipole resistances for all storms, equation (3.42) is used to calculate the ratio of dipole current strength to the GEC current contribution. Figure 3.17 shows a one year average of R_{ratio} when storms occur. This is the efficiency factor for contributing to the GEC and it is evident that the storms in mid latitudes are more efficient than storms near the equator for contributing current to the GEC. At mid latitudes, approximately 40% of the current generated within the dipole contributes to the GEC, while closer to the equator approximately 20% of the current generated within the dipole contributes to the GEC. This shows that storms at higher latitudes are twice as efficient at generating a global current compared to lower latitude storms.

The variation in storm efficiencies is caused by the difference in the heights of the charge regions. The conductivity of the atmosphere increases at an exponential rate, as shown in figure 3.8. Therefore, if the charge regions are lower in the atmosphere there will be more resistance between the dipoles, causing more current to flow in the global circuit. Figure 3.18 shows the distribution of base heights of the charge centers (identified by temperature and convective updraft mass flux). There is a clear decrease in the bottom charge height with increasing latitude. The depth and top charge center are also shown as a function of latitude in figure 3.19. The depth of the storm, difference between charge centers, does not change significantly with latitude, maintaining about a 2 km separation throughout the globe. The location of a storm's charge centers relative to the conductivity profile of the atmosphere dictates the efficiency of the storms. The variation in the base heights of the storms leads to more efficient storms at mid latitudes.

The previous figures have all shown the properties of storms when they occur, but the frequency of how often these storms occur has been ignored. Figure 3.20 shows the daily occurrence frequency of charge generating storms averaged over a year. Charge generating storms are more

Storm Efficiency [R_{ratio}]

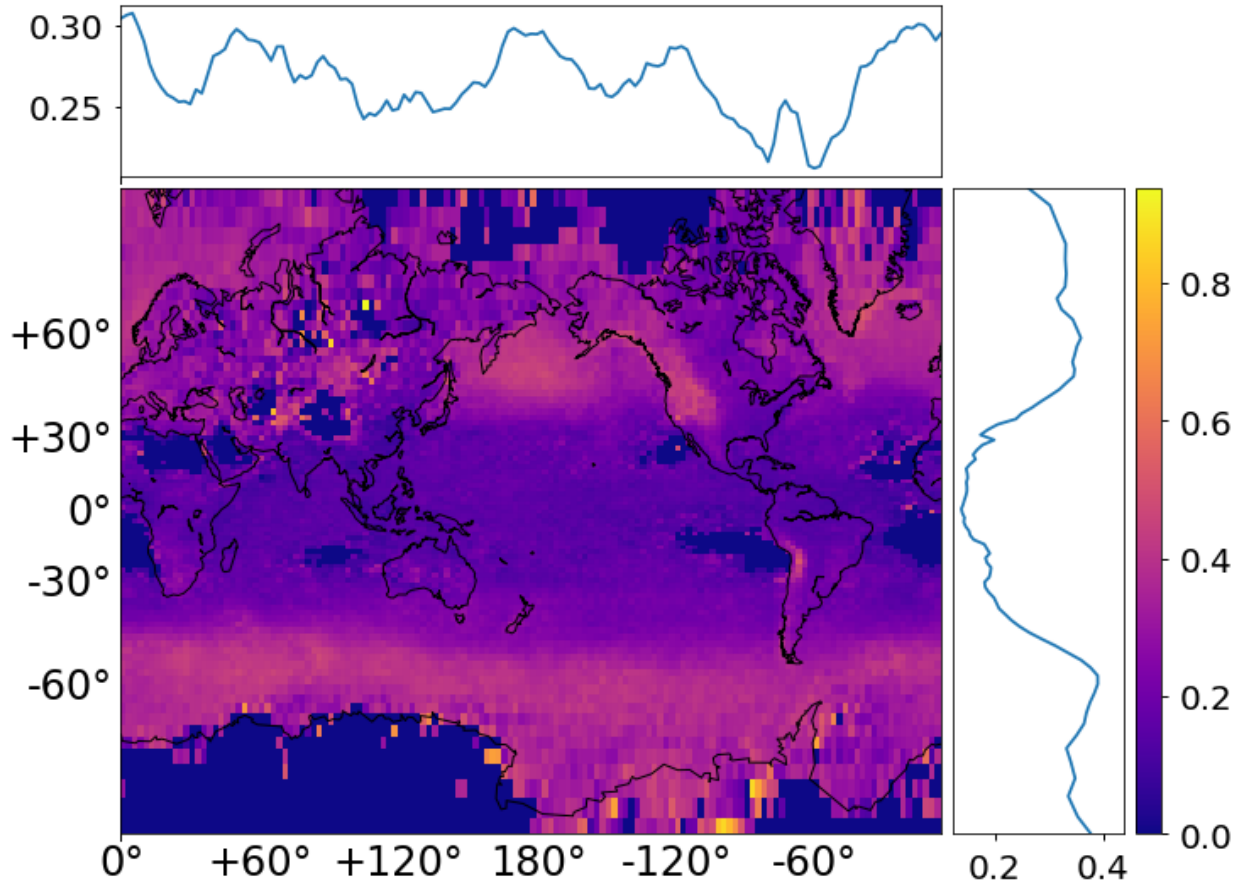


Figure 3.17: The mean resistance ratio over a year. The most efficient storms are located in the mid latitudes, where the storms are about twice as efficient as in the tropics.

frequent at the mid latitudes, which is contrary to the occurrence frequency of storms in general. This is due to many of the frequent low latitude storms not being cold enough to generate charge. The frequency of storms shown in figure 3.20 is dependent on both the temperature and convection within the storm, not just the convection alone.

The total current within the circuit depends on both the dipole current strength and the resistance ratio as shown in equation (3.43). Figure 3.17 showed that mid latitude storms are more efficient, while figure 3.16 showed that the low latitude storms produce the strongest currents. The combination of these factors determines the total contribution current. This total GEC contribution

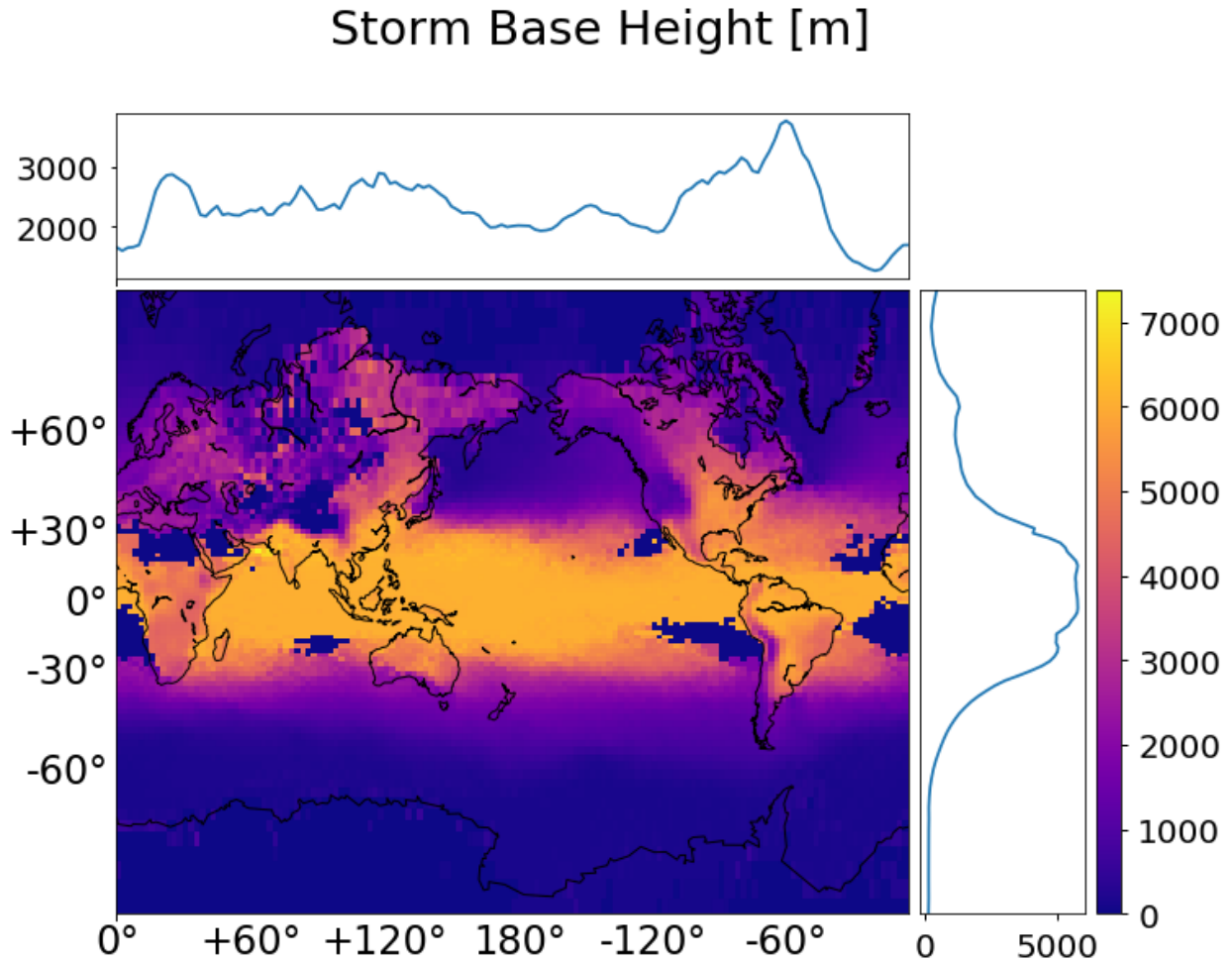


Figure 3.18: The base height of storms is much higher in the tropics due to the colder temperatures being higher in the atmosphere.

current, I_{GEC} , is shown in figure 3.21, which inherently includes the storm frequency throughout the year. There are still hot spots over the continents, but the distribution has been shifted away from the equator.

The latitudinal dependence of all the factors that go into the global production of current to the GEC are normalized to their respective means and shown in figure 3.22. The dipole current (blue) is strongly peaked near the equator, while the resistance ratio (orange) and storm frequency (green) have stronger contributions towards the poles. The combination of these three factors

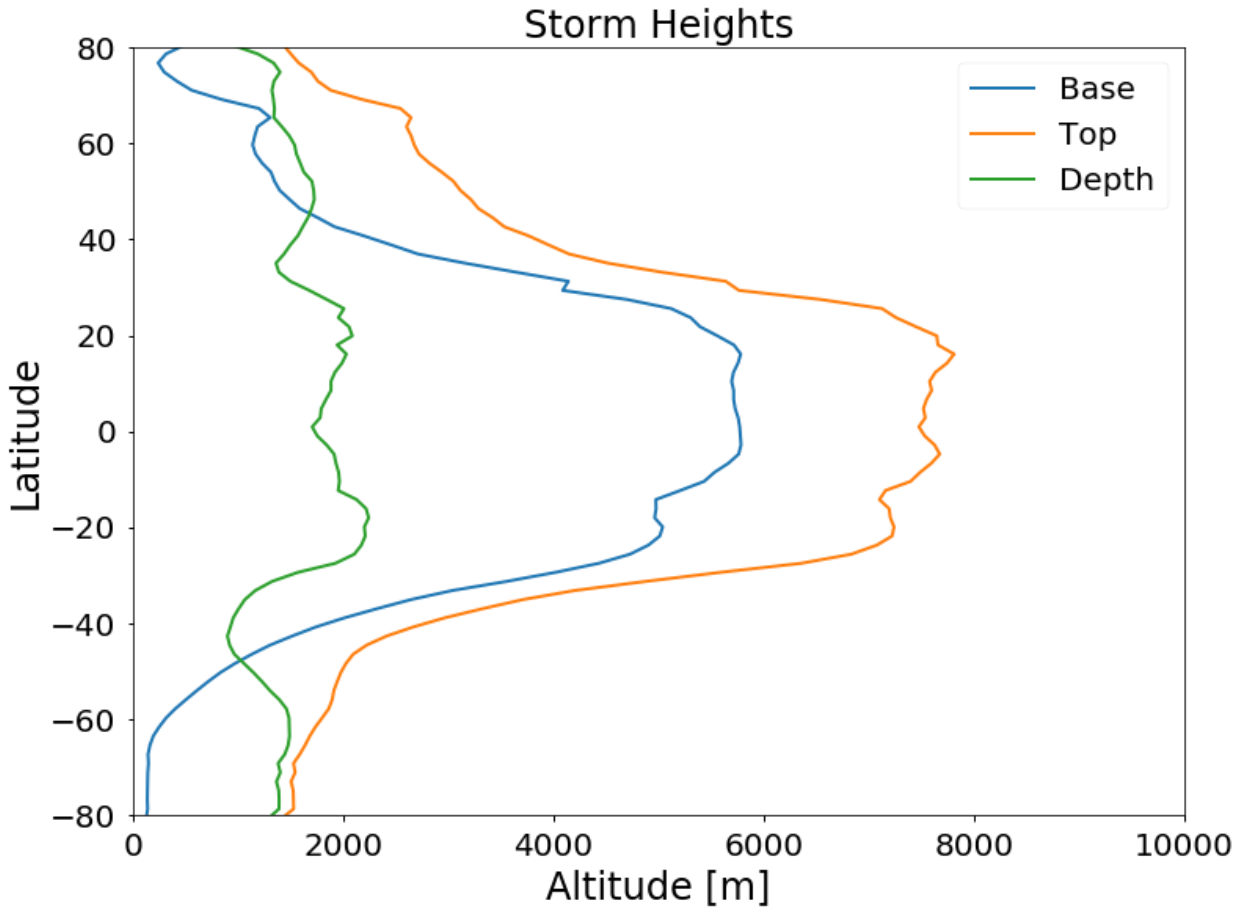


Figure 3.19: The variation with latitude of the heights of different storm parameters. The depth of storms is similar across all latitudes, while the base height and top height of the storms are significantly higher in the tropics than at higher latitudes. More resistance is located between the dipoles of a storm, making it more efficient, when the storms are at lower altitudes due to the decrease in resistance with altitude.

contributes to the total GEC current (red), where the peak is still near the equator, but the distribution has been shifted towards the poles compared to the individual dipole current strengths.

The typical analysis of models is to determine how well they reproduce the Carnegie curve, shown in figure 1.1 and discussed in more detail within Harrison [2013]. This curve is the diurnal variation of the electric field in fair-weather. This surface electric field measurement is assumed to correlate to the GEC contribution current which leads to a diurnal variation in the GEC current as well. The GEC contribution currents within models generally underestimate the diurnal variation that is seen in surface electric field observations. Lucas et al. [2015] utilized a current parameteri-

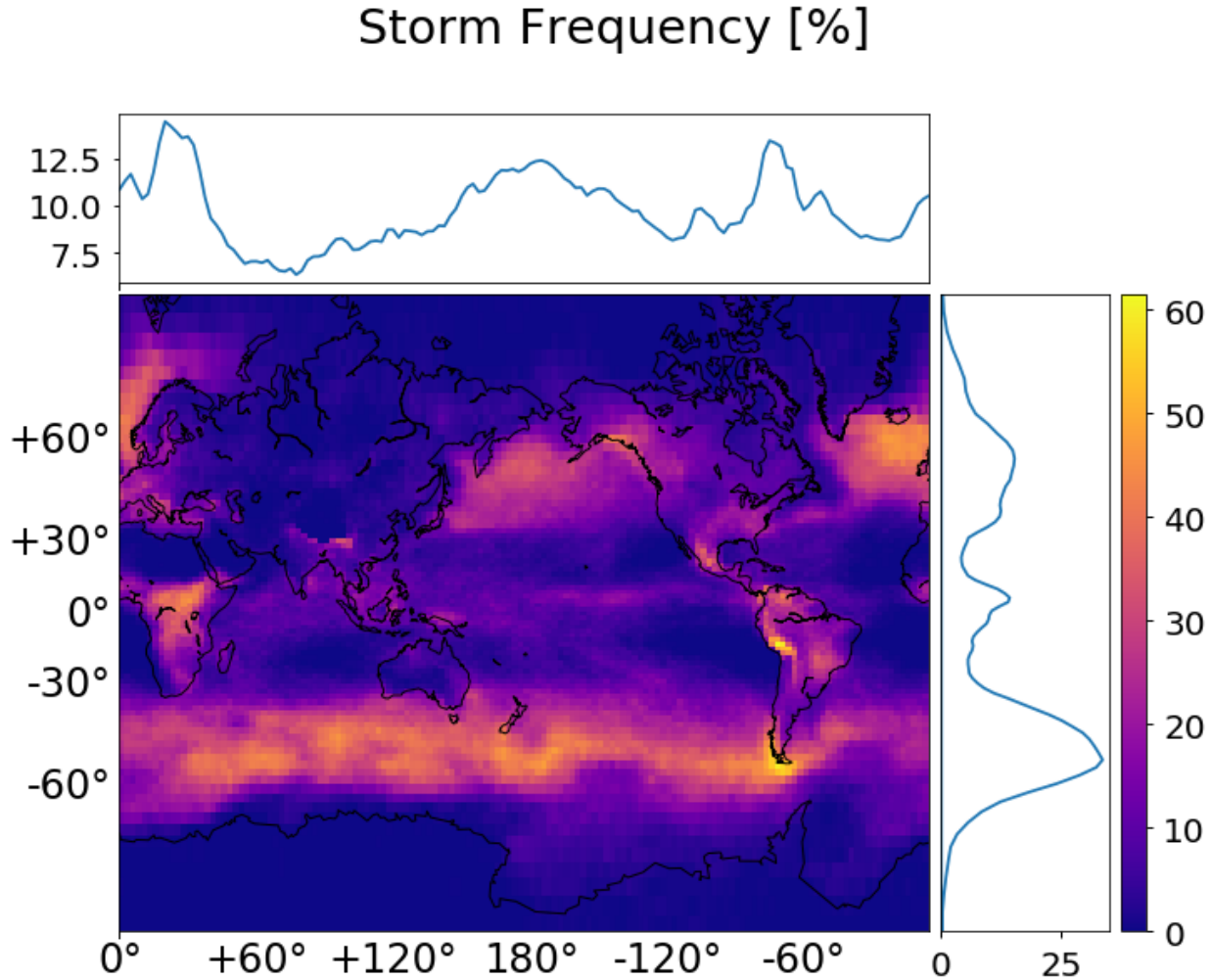


Figure 3.20: The occurrence frequency of storms with charging taking place. Storms with charge generation are more frequent at higher latitudes due to the colder temperatures within the storms.

zation based on the updraft mass flux and pressure levels within the model and obtained variations of around 10%. Kalb et al. [2016] tested a lot of different model parameters and were only able to generate around a 5-6% diurnal variation. With the use of the resistance ratio and convective precipitation the current model produces a 6% diurnal variation averaged over the entire year which is shown as a typical Carnegie curve in figure 3.23.

The formulation of current implemented in this work produced a significant new finding on the utilization of the resistance ratio. Many equivalent circuit models have the incorporation of a reduction in conductivity through the storm region incorporated in them, see for example Slyunyaev

Global Current Contribution [pA/m²]

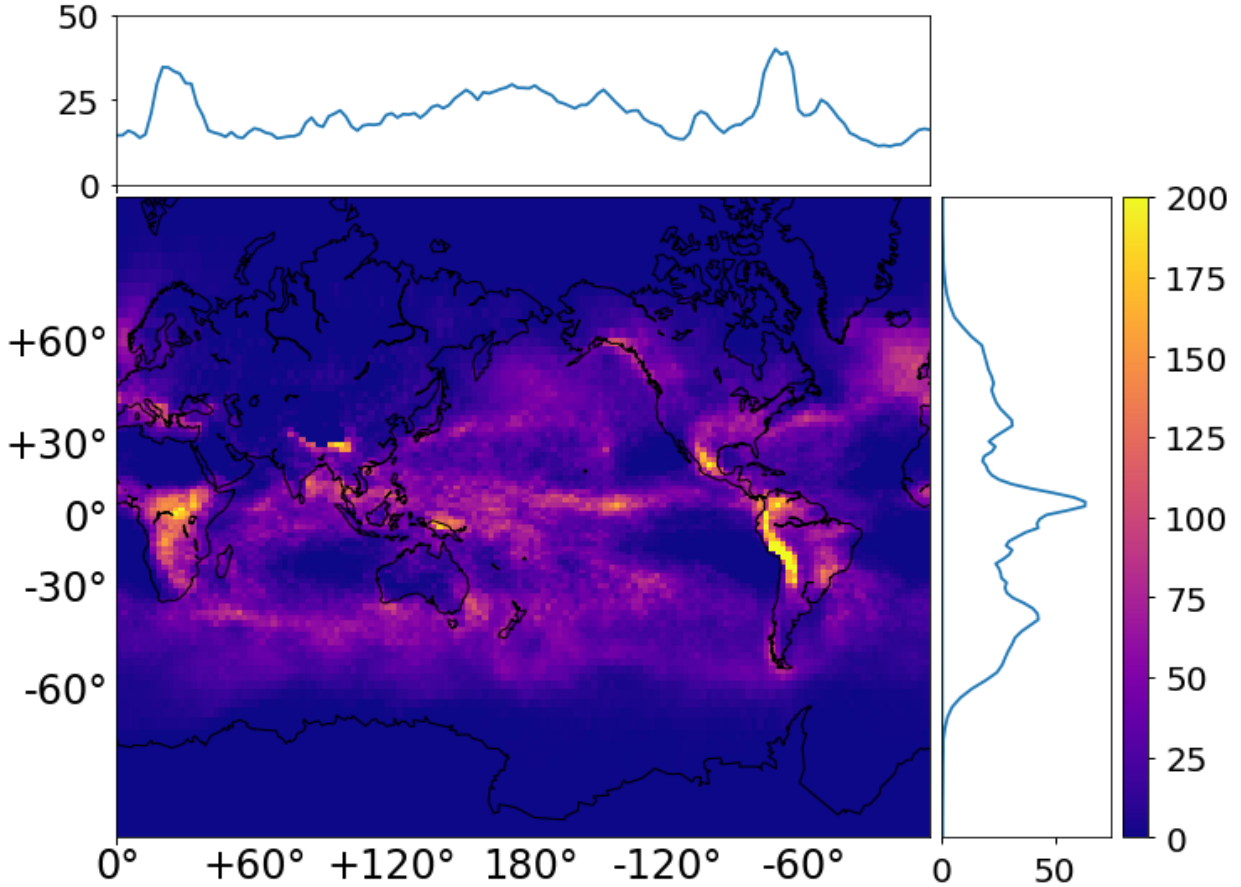


Figure 3.21: The mean current contribution to the GEC over a year. The current contribution is a coupling of figure 3.17 and figure 3.16.

et al. [2015] and the references within. These implementations are factors that are universally applied to all storms throughout the atmosphere. In this work, the conductivity within the storms is generated with the use of a global climate model. This produced a strong latitudinal difference in resistances between the dipole centers that has not been identified before. Figure 3.22 showed how this ratio stretched the GEC current contribution to mid latitudes, although still peaking near the equator. The incorporation of these new resistance ratios shows that storms around the equator are not necessarily the only ones that are contributing to the GEC. This deserves further investigation and measurement, with most overflights being done near low latitudes [Mach et al., 2009].

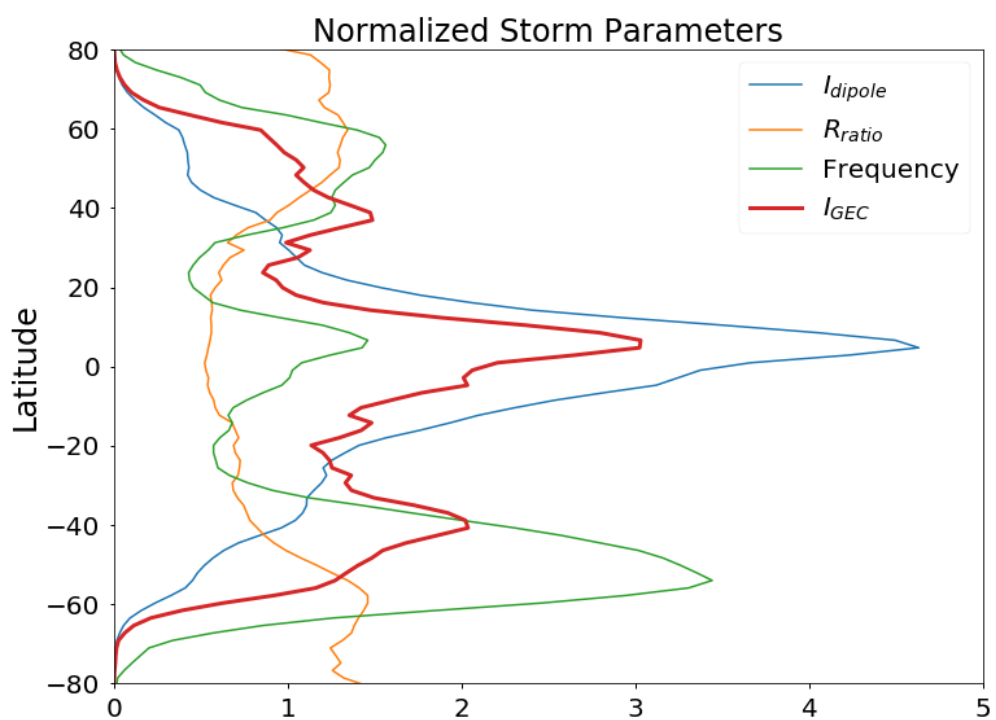


Figure 3.22: The normalized latitudinal distribution of all factors that go into generating the GEC current.

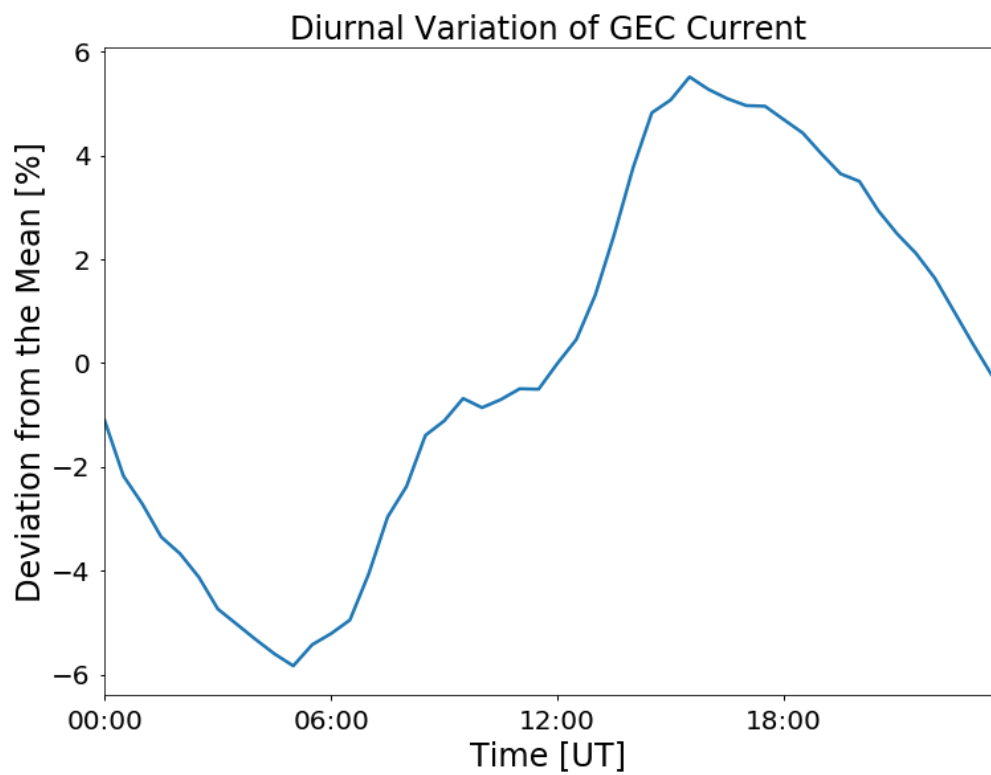


Figure 3.23: The diurnal variation of the model produced GEC current shown in percent deviation from the mean.

3.3 Summary

This chapter described the generation of electrical parameters within the atmosphere from a physics-based perspective. The production of ions from galactic cosmic rays, radon, and solar proton events were discussed in section 3.1.1, while physical mechanisms for the loss of ions, including recombination, aerosols, and clouds, were described in section 3.1.2. Incorporating all of the production and loss mechanisms together generates a highly variable, in both space and time, conductivity distribution throughout the atmosphere.

To drive the electric circuit, source currents were investigated in section 3.2. The global source currents are generated with relationships to known charging mechanisms and the conductivity within the domain. Coupling the source current strengths with the conductivity within the domain showed that storms towards higher latitudes are more efficient at generating global currents than storms near the equator. The generation of conductivity and sources within the atmosphere is the basis for the global electric circuit. Chapter 4 will describe the generation of the global electric circuit and discuss how return currents and electric fields are created throughout the atmosphere.

Chapter 4

Global Electric Circuit Model (WACCM-GEC)

Many different electrical processes in the atmosphere were described in chapter 3. This included the ionization of the atmosphere and the generation of source currents. This chapter utilizes these electrical processes and describes how to implement them within global circulation models. Specifically, this work is implemented within the community earth system model (CESM) with the whole atmosphere community climate model (WACCM) extension to higher altitudes. The GEC model within WACCM will be referred to as WACCM-GEC from here on.

WACCM-GEC calculates the currents and electric fields within the atmosphere to understand how all of the regional processes influence measurements of atmospheric electric fields on a global scale. The fundamental mathematics behind the calculation of the global current system are described within this chapter. The equations build off of the underlying physical parameters described in section 3.1 and section 3.2, which are illustrated in figure 4.1.

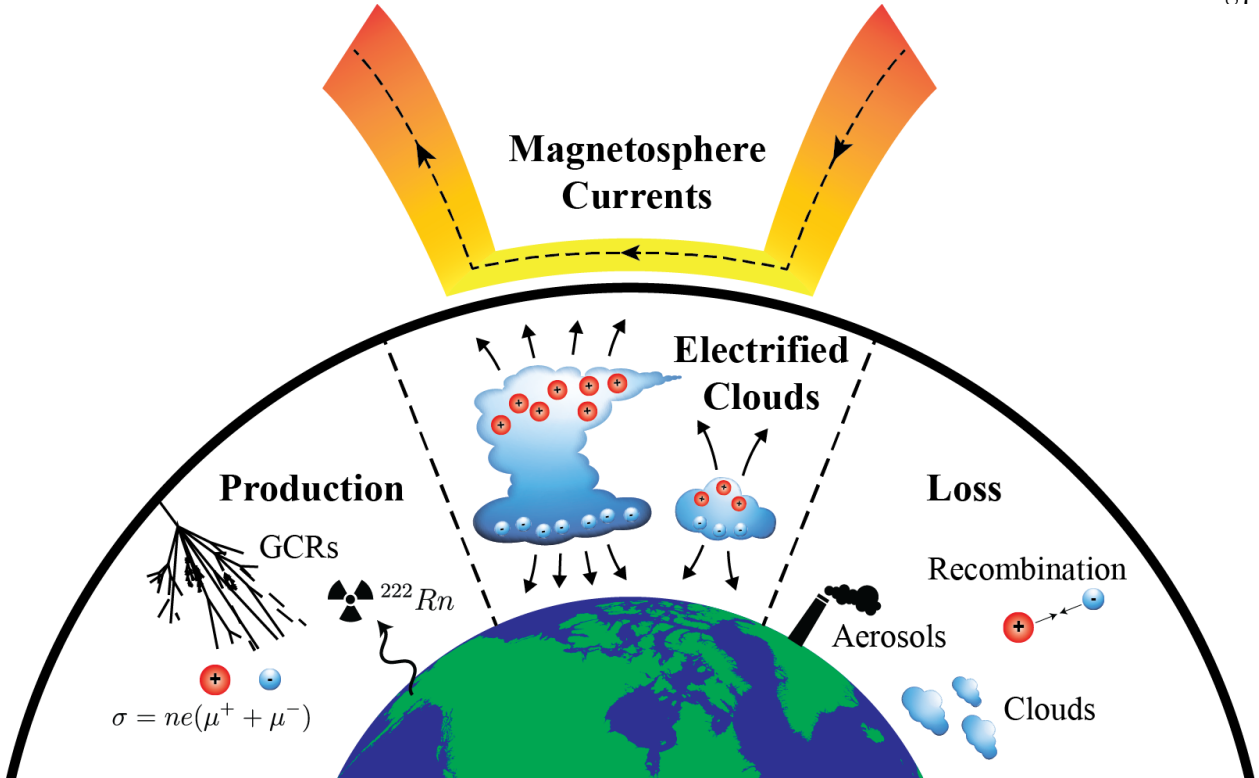


Figure 4.1: A representation of the major physical processes included within WACCM-GEC including conductivity, sources and magnetospheric currents.

4.1 Model Description

To study the GEC, measurements are done in fair-weather regions where there are no sources near the measurement location. This means that the measurements ideally measure the return current of the circuit. Measuring the return currents of the circuit is enabled by linearly decoupling the circuit into two distinct equations. One for sources in the circuit that charge the ionosphere and another equation for the discharging of the atmosphere globally. This can be accomplished by solving for the source currents and fair weather currents separately and adding the solutions together due to the linearity of the partial differential equation. The two separate systems being solved are

$$\text{FairWeather : } \nabla \cdot \sigma \nabla \phi_{fw} = 0 \quad (4.1)$$

$$\text{SourceRegion : } \nabla \cdot \sigma \nabla \phi_s = S, \quad (4.2)$$

with ϕ_{fw} and ϕ_s representing the fair weather and source potentials respectively, and the total potential within the system, ϕ , satisfying $\phi = \phi_{fw} + \phi_s$.

In this problem we apply Dirichlet (fixed potential) boundary conditions on the upper and lower boundaries. Earth's surface is defined as being a zero potential surface with zero net current flow through the surface. The upper boundary is determined by the source and conductivity distribution in the domain and also defined to have no net current flow through the boundary. A different approach to the upper boundary condition is addressed in Kalinin et al. [2014], where they discuss the contribution to potential for individual storms, including modification of the conductivity within the cloud.

The top potential brings closure to the system, so that there are no leakage currents from the GEC, which follows from ensuring current continuity as seen in equation (3.1). Other studies determine the contribution to the upper boundary potential directly from each storm [Mareev and Volodin, 2014]. The use of this method implies that the atmosphere follows a known exponential conductivity profile everywhere across the globe. This indicates that an increase in resistance far away from the storm would not influence the potential of the ionosphere. In this work, we relax the assumption that the conductivity of the atmosphere follows an exponential and calculate the current that storms contribute to the system, and determine the potential based on the total current and resistance of the system.

4.2 Calculation of Potentials

The potential of the ionosphere is solved in a two-step approach. First, the source region is solved with 0 V potentials on the top and bottom of the domain. Integrating over the top and bottom boundaries determines how much current is exiting the domain. This calculates the amount of current that is required to close the system and conserve currents within the model, which is the downward current that is input into the fair weather region. The second step is to calculate the total resistance of the atmosphere. Once the total resistance and total current are known, one can apply Ohm's law to determine the potential needed at the top boundary of the fair weather

region. Another means to calculate the current is to separate the source term, S , into individual source columns applying the linearity argument again, such that,

$$S = S_1 + S_2 + S_3 \dots$$

and

$$\phi_s = \phi_1 + \phi_2 + \phi_3 \dots$$

which allows WACCM-GEC to calculate the total current in a grid cell, I_{col} , due to the sources within that grid cell. Figure 4.2 is a representation of storms in a grid cell contributing a current within that column. Each electrified cloud in general only covers several kilometers in the horizontal, while grids for WACCM are more than 100 km. This means it is difficult to resolve individual storms in climate models, unless they are large convective systems. Therefore a parameterization for determining the source strength within each column is described in section 3.2. Calculations in section 3.2.1 showed that neighboring grid cells don't significantly modify the local current within the column, and can therefore be solved independently. Now the total current flowing in the domain can be calculated by summing up all of the column contributions

$$I_{GEC} = \sum_{col} I_{col}. \quad (4.3)$$

After solving for the total source contribution current the fair-weather domain, equation (4.1), can be solved to determine the potential of the ionosphere. With the high conductivities at the boundary of the fair-weather GEC, the boundaries can be thought of as constant potential surfaces, where any excess charge is redistributed quickly compared to the time scales of interest [Israël, 1970]. As a standard definition throughout the results, we define the potential at the surface of the Earth to serve as our reference, and set it to a value of zero. The upper atmosphere is then typically between a positive potential range of 250-350 kV relative to Earth's surface.

This now allows the potential difference between the ionosphere and ground due to GEC sources, PD_{GEC} , to be determined through the following relation between the total resistance of

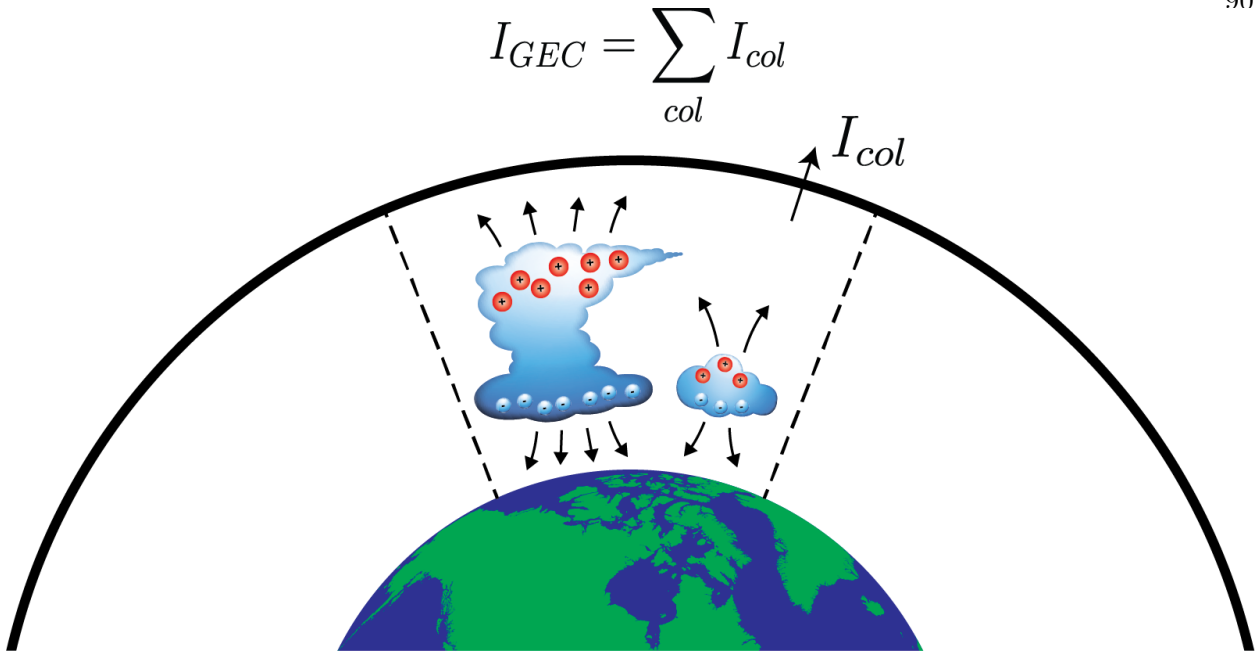


Figure 4.2: A representation of electrified clouds within a global climate model with a charge separation producing a current that leaves the column, I_{col} . When all of these currents are summed they produce the total GEC current, I_{GEC} .

the atmosphere, R_{tot} , and the total GEC source current, I_{GEC} ,

$$PD_{GEC} = I_{GEC} R_{tot} = \sum_{col} I_{col} * \left(\sum_{col} \frac{A_{col}}{R_{col}} \right)^{-1} \quad (4.4)$$

where we have used the fact that column resistances, R_{col} , will add in parallel

$$R_{tot} = \left(\sum_{col} \frac{A_{col}}{R_{col}} \right)^{-1}$$

with A_{col} being the area of the column. Figure 4.3 shows an illustration of the conductivity calculation and how the total resistance is calculated from the physical processes within the conductivity module.

$$R_{tot} = \left(\sum_{col} \frac{A_{col}}{R_{col}} \right)^{-1}$$

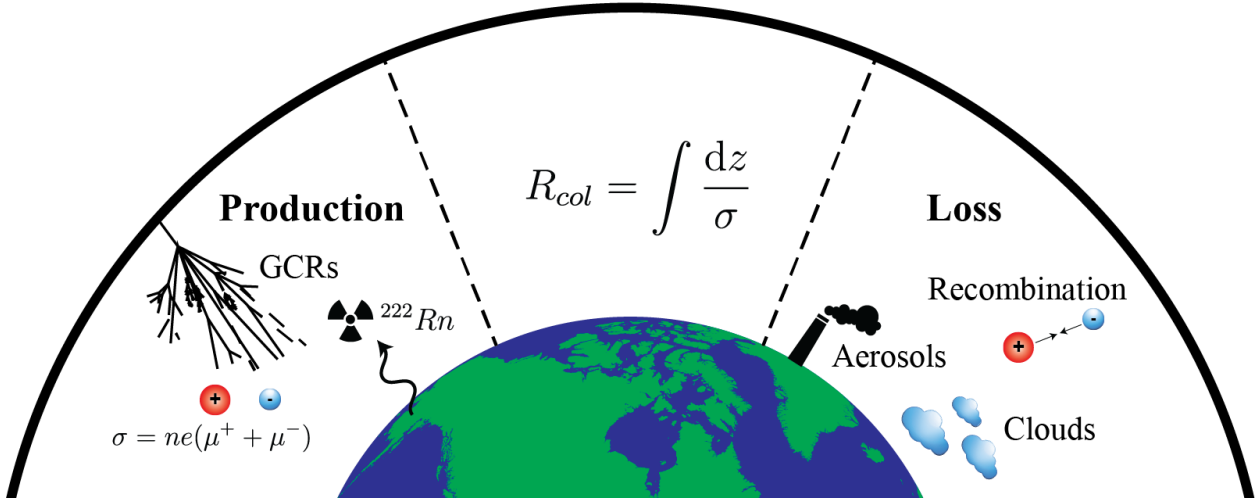


Figure 4.3: A representation of the physical processes that are in the conductivity module and how the total resistance is calculated from conductivity.

With the total resistance and total current contribution known, one can solve for the upper boundary potential due to GEC sources with equation (4.4). Figure 4.4 is an illustration of the current sources and conductivity calculations being applied to obtain the total potential of the GEC, PD_{GEC} .

With the PD of the upper boundary known, the vertically-uniform column current densities and height-dependent electric field in the fair weather region can be calculated by utilizing the ionospheric potential of that column PD_{col} as follows (where $PD_{col} = PD_{GEC}$ for a horizontally uniform potential in the ionosphere).

$$J_{col} = \frac{PD_{col}}{R_{col}} \quad (4.5)$$

$$E_{col,z} = \frac{J_{col}}{\sigma_{col,z}} \quad (4.6)$$

with J_{col} the column current density for a specific column, and $E_{col,z}$ is the electric field at an altitude z within the column.

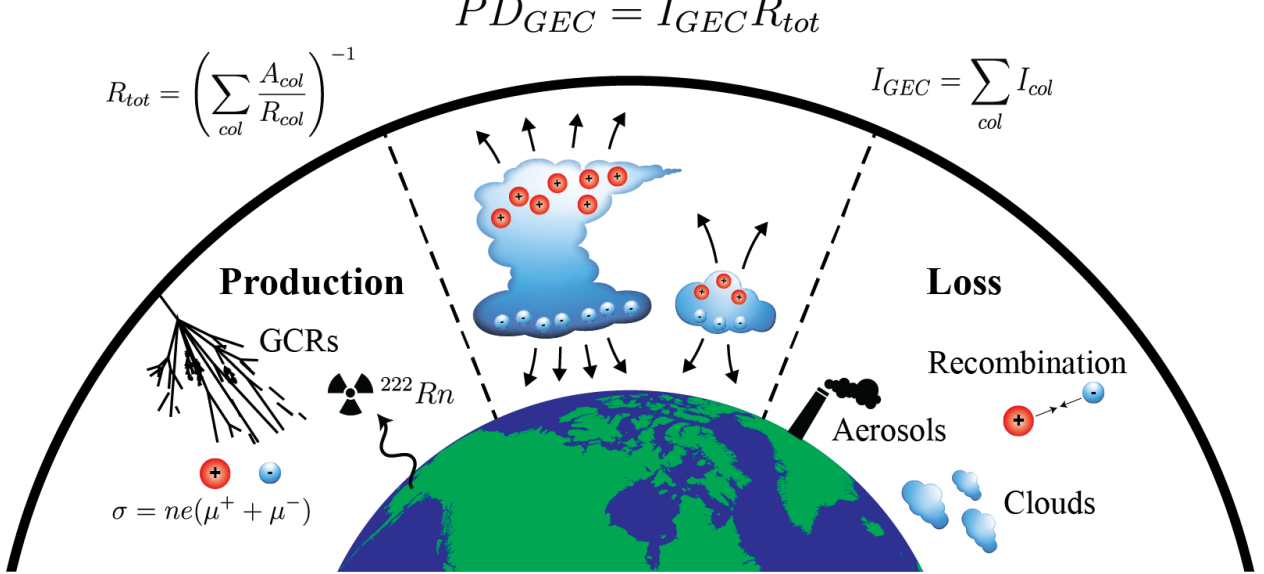


Figure 4.4: A representation of the conductivity and source currents within the GEC model. The column source currents and column resistances produce a global current and resistance that are used to calculate the total potential of the ionosphere, PD_{GEC} .

4.3 Non-uniform Boundary Conditions

The discussion in section 4.2 assumed a constant potential surface throughout the upper boundary. However, there are separate current systems flowing within the ionosphere, due to the ionosphere neutral wind dynamo, and between the ionosphere and magnetosphere, due to the solar wind-magnetosphere dynamo, that create and maintain horizontal potential differences in the ionosphere. These current systems are assumed to be in a separate domain and do not contribute as a source current to the GEC but rather modify the distribution of potentials of the upper boundary in WACCM-GEC.

The horizontal potential created in the ionosphere by these two additional external current systems is incorporated into WACCM in a manner described by Liu et al. [2010b]. At high latitudes, the horizontal potential created in the ionosphere by the solar wind-magnetosphere dynamo is calculated with the Weimer model [Weimer, 1995]. This model is implemented within WACCM to provide a magnetospheric potential over the entire globe. This allows for temporal and spatial variations from solar influences to be incorporated into WACCM-GEC by perturbing the upper

boundary potential over every column. Weaker but horizontally structured potential in the ionosphere can also be created by the neutral wind dynamo. This is accounted for at middle to low latitudes by incorporating an empirical model based on observations described by Richmond et al. [1980]. The variable PD_{col}^{mag} will be used to represent the potential solely due to the magnetosphere current system and neutral wind dynamo that contributes to the total upper boundary potential.

Figure 4.5 shows the output of a typical global ionosphere potential pattern during a quiet solar day that combines both of these external current systems. The stronger and more dynamic potential differences lie at high latitudes where the solar wind-magnetosphere dynamo is most effective. To maintain current continuity within the GEC system, the upper boundary potential is modified globally to ensure that the GEC currents are the only current source in the atmosphere. This can be viewed as allowing for a floating potential PD_{float} .

$$PD_{float} = \int_{4\pi} \frac{PD_{col}^{mag}}{R_{col}} dS * R_{tot} \quad (4.7)$$

The potential at every grid column is then calculated as follows

$$PD_{col} = PD_{GEC} + (PD_{col}^{mag} - PD_{float}), \quad (4.8)$$

where the floating potential is incorporated because we are maintaining current continuity between the ground and ionosphere.

Finally, this new potential difference of the column is used to calculate the current density and electric field according to equation (4.5) and equation (4.6). Within WACCM-GEC the floating potential from the magnetospheric perturbation modifies the global potential by less than one tenth of one percent. This small change is due to the fact that the magnetospheric potentials have both positive and negative components and that the column resistance, R_{col} , over these areas does not vary significantly. However, the local potential changes introduced to individual columns will be shown to have significant local effects. Figure 4.6 is an illustration of the magnetospheric current system and the modifications that can occur to individual columns. Once the potential from each column is known, the current density and electric fields are calculated for each model grid point.

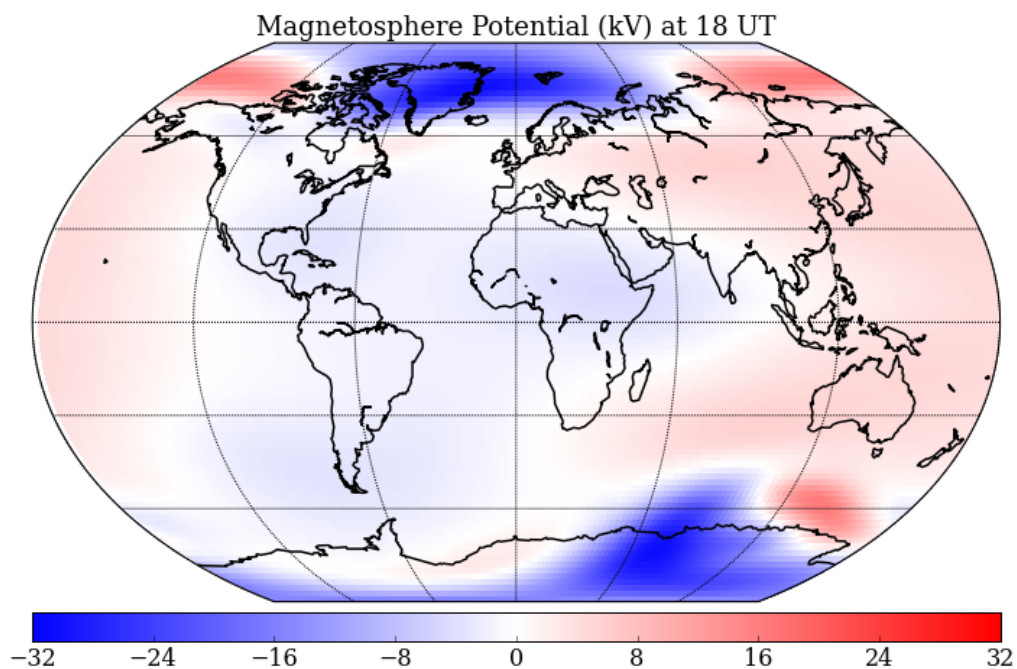


Figure 4.5: The magnetosphere potential around the globe due to external current systems at 18 UT on a quiet solar day. The largest potentials are seen at high latitudes in the arctic and antarctic regions caused by the solar wind-magnetosphere dynamo.

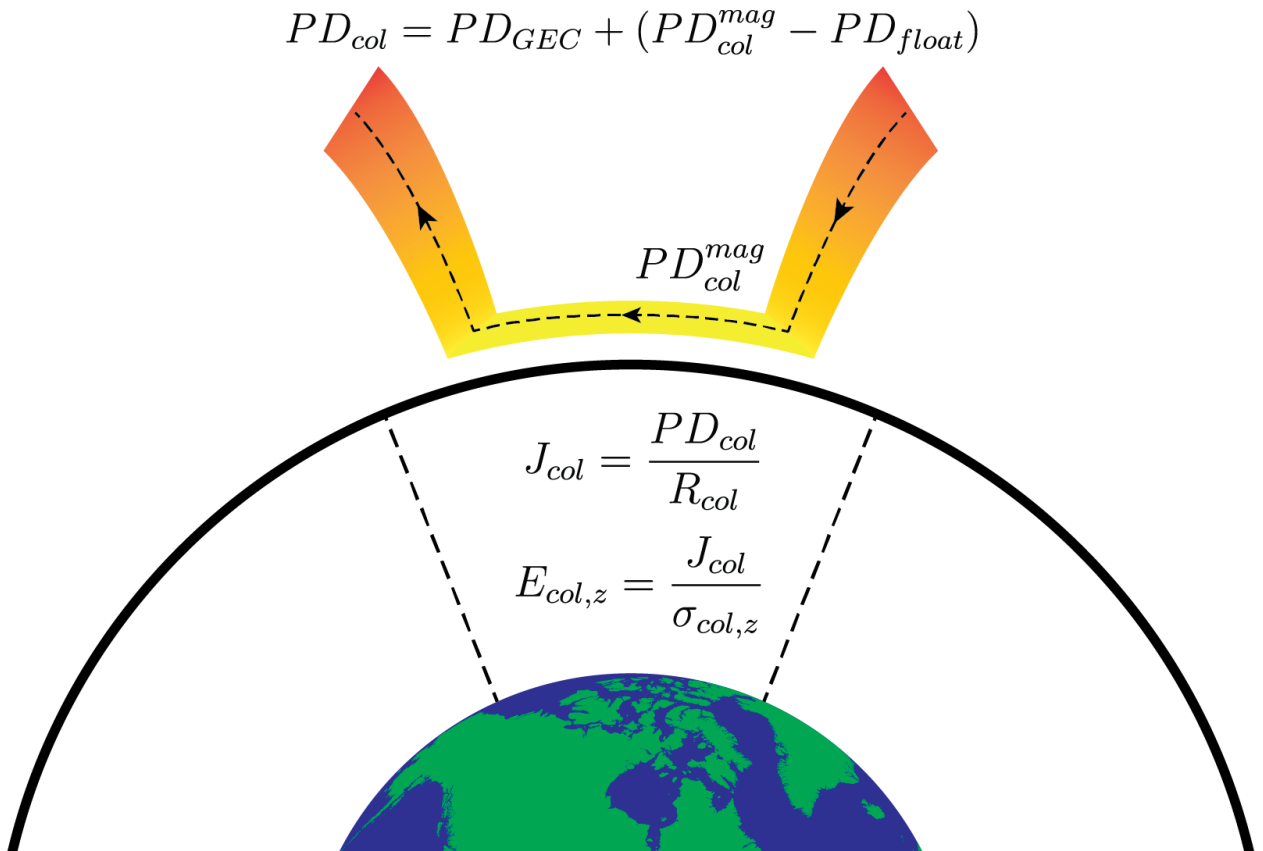


Figure 4.6: A representation of the magnetospheric current system modifying the potential above a model column. Within the model the potentials of all columns are modified by a global floating potential, PD_{float} to enforce current continuity. The current density and electric field are then computed after the potential of the column is known.

4.4 Summary

The generation of currents and electric fields in the atmosphere within a consistent model framework, called WACCM-GEC, were developed in this chapter. The underlying conductivity and source generation that were described in chapter 3 were utilized to obtain the total resistance and source current within the atmosphere. These processes led to the generation of electric fields and return currents to maintain current continuity throughout the atmosphere. WACCM-GEC will be exercised in chapter 5 to determine how currents and electric fields change in response to different scenarios.

Chapter 5

WACCM-GEC Model Results

In chapter 4 the equations underlying WACCM-GEC were developed and the generation of currents and electric fields within the model were calculated. Within this chapter the model will be exercised to demonstrate the capabilities of WACCM-GEC. This is done by running the model over representative periods, during which observational data in the Antarctic was collected. This run allows the conductivity and sources to be generated in a free-running simulation within a consistent model framework. The magnetospheric contribution seen at high latitudes will be analyzed in detail in section 5.1, followed by a comparison of WACCM-GEC electric fields to observational electric fields in Antarctica in section 5.2. Then an analysis of different conductivity disturbances will be investigated. The influence of the solar cycle on the GEC will be described in section 5.4 and volcanic eruptions in section 5.5.

5.1 Influence of Magnetospheric Currents on GEC Properties

The new model formulation discussed in chapter 4 opens up many opportunities to explore various influences on the GEC. As a demonstration, this section elucidates the connection between the GEC current system and external current systems flowing in the ionosphere. The upper boundary conditions implemented within WACCM-GEC enable the combined influences of the GEC and magnetosphere currents on electric potential distributions to be investigated. The imposed potential due to solar wind-magnetosphere interactions is best described in Earth's geomagnetic coordinates, while the GEC source contribution to the ionosphere potential is driven by solar heating and best

described in Earth's geographic coordinates. The geomagnetic coordinate system used in WACCM to describe the magnetospheric potential is the magnetic apex coordinates that are described in Richmond [1995] and then converted to geographic coordinates. These two potential patterns are summed at each time step to produce the total potential pattern for the GEC. With these two potential patterns rotating differently within the earth-fixed frame, there are times and locations on the globe where these potentials are in-phase and out-of-phase with each other, which can lead to an interesting dynamic response in the polar regions. Both the magnetospheric perturbation and GEC sources have dominant 24 hour modes. Because the net potential in the model is determined based on equation (4.8), these two contributions can be decomposed into an amplitude and phase to elucidate their relative contribution to the net potential. For illustration purposes, a sinusoidal function with a 24-hour period plus a constant offset is fit to the two potentials and summed, which is represented by the following formula.

$$PD_{col}(t) = C_{col} + A_{col}^{mag} \cos(\omega t + \phi_{col}^{mag}) + A_{GEC} \cos(\omega t + \phi_{GEC}) \quad (5.1)$$

The variables A_{col}^{mag} and ϕ_{col}^{mag} represent the magnetospheric amplitude and phase respectively, while A_{GEC} and ϕ_{GEC} are the amplitude and phase contribution from the GEC, C_{col} is the constant offset for the column and ω the 24 hour angular frequency of interest. A_{col}^{mag} is stronger in the polar regions due to the magnetospheric current systems at high latitudes, whereas A_{GEC} , without a column subscript, is the same globally and independent of location.

For equatorial locations A_{col}^{mag} is negligible, and therefore the A_{GEC} leads to the variations detected at ground level, which allows for comparisons to the diurnal variation of the electric field when viewed in UT. Consequently the neutral wind dynamo in the ionosphere at middle and low latitudes has little influence on the local GEC potential. When conducting measurements at high latitudes, one must also take into account the perturbation due to the solar wind-magnetosphere dynamo Burns [2005]. To illustrate the relative contributions throughout the globe, the percent

change of the total potential from only the GEC potential can be computed with the following equation.

$$\% \text{Change} = 100 \frac{A_{col}^{mag}}{A_{GEC}} \cos(\phi_{col}^{mag} - \phi_{GEC}) \quad (5.2)$$

Calculating the amplitude and phase at every model point provides a way to determine the relative influence of the magnetospheric potential globally. Figure 5.1 shows that there are regions where the amplitude of the magnetospheric perturbation is up to 50% that of the GEC, and that there are regions where these amplitudes will constructively and destructively interfere. The red shading indicates constructive interference with the diurnal variation of the electric field, while the blue shading indicates areas that destructively interfere. The 50% perturbation is during quiet geomagnetic activity. This effect could be much larger and compete with the GEC variations for certain locations in more geomagnetically active situations.

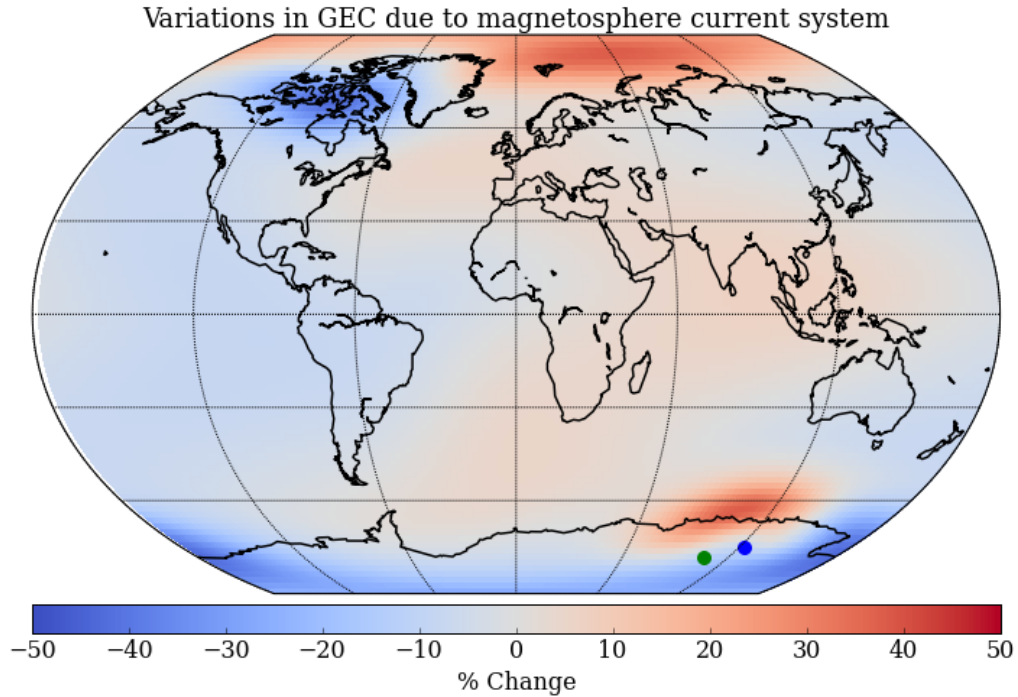


Figure 5.1: The percent change due to magnetospheric potential variations relative to the changes imposed by the diurnal variation of the GEC sources. The blue dot represents the Concordia station and the green dot represents the Vostok station.

5.2 Antarctica Observations and Magnetospheric Influences

Section 5.1 provided an illustrative means to demonstrate the global influence of the magnetosphere current system on GEC properties. Of course, the model is also able to provide a more quantitative assessment for any given location on the globe. To analyze the effect of magnetospheric perturbations and compare with high-latitude observations, data from two Antarctic Stations are utilized, Vostok (106.8E, 78.5S) (green dot) and Concordia (123.3E, 75.1S) (blue dot). Vostok and Concordia, while not ideal locations for detecting large magnetospheric influences, are the only long-term data sets available in the polar regions. Observations of this kind in the polar regions

are sparse and the data sets from these Antarctic sites have been investigated and published by G. B. Burns in several papers, e.g. Burns et al. [2012] and Burns [2005].

These stations are at similar latitudes, but different longitudes, which will generate different phase relationships between the GEC and external ionospheric contributions to the potential, and consequently the vertical electric field. This can be seen in figure 5.2, which shows the relative electric field variation from WACCM-GEC over Vostok and Concordia for one day.

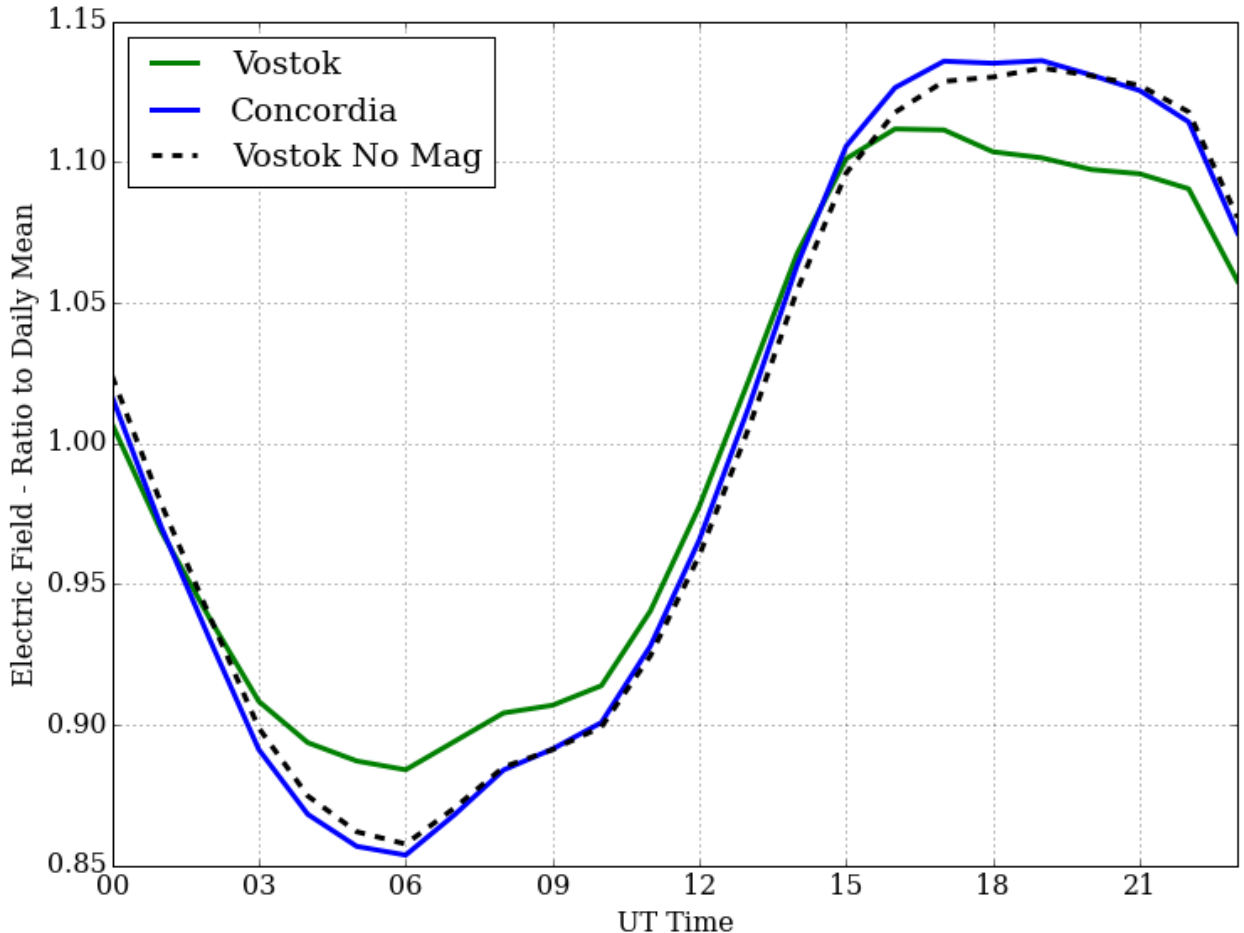


Figure 5.2: Model produced diurnal variation of electric field over a single day at two Antarctic stations, Vostok (green) and Concordia (blue), as well as Vostok without any magnetospheric potential component (dashed-black).

Analyzing the model output, one can tell that the potential pattern over Vostok (green curve) rises and falls sooner than the model output for Concordia (blue curve). Thus, Concordia

measurements would more closely resemble the typical diurnal variation near equatorial sites as it experiences little influence from UT variations in the cross cap potential because it is near the geomagnetic pole. Utilizing WACCM-GEC to analyze these results, one can separate out the influences in the data from magnetospheric contributions and GEC current contributions. The black dashed line in figure 5.2 shows the effective GEC source contribution to the local measurements at Vostok, which we have calculated by removing the magnetospheric component. With this decoupling of the magnetospheric system and GEC system, the influence of the magnetosphere contribution tends to shift the phase of the diurnal variation of the electric field to earlier times. Other high-latitude locations will experience different influences depending on their location relative to the geomagnetic pole and the magnetospheric potential pattern, a fact recognized but not fully described in previous publications.

Thus far, only stations where data sets are also concurrently available have been analyzed. To determine the largest influence the magnetosphere can have during a solar quiet day, figure 5.1 was used to find an area that is in-phase (197.5E, 80.5N) and also one that is out-of-phase (77.5E, 80.5S) with the GEC current sources. Figure 5.3 demonstrates the different readings one could get at different areas around the globe, simply based on measuring ground level electric fields. The baseline electric field variation in figure 5.3 is the daily mean diurnal variation determined from WACCM-GEC at a low-latitude location (0E, 0N). However, at the high latitude locations, the electric field perturbation with UT can be significantly magnified or suppressed due to the influence of the magnetospheric potential [Burns, 2005; Reddell et al., 2004; Corney et al., 2003]. The mapping of this horizontal potential to the surface has been discussed by Park [1976] where it was demonstrated that horizontal potential structure greater than about 200 km will experience little attenuation in reaching the surface. Thus, the magnetosphere potential serves as a source of variability in the surface electric fields independent of thunderstorm activity.

To display the relative influence in more absolute terms, figure 5.4 shows the separate upper boundary potential values due to the GEC and magnetospheric sources for the two regions identified in figure 5.3. This figure demonstrates the phase relationship of the magnetosphere to the GEC for

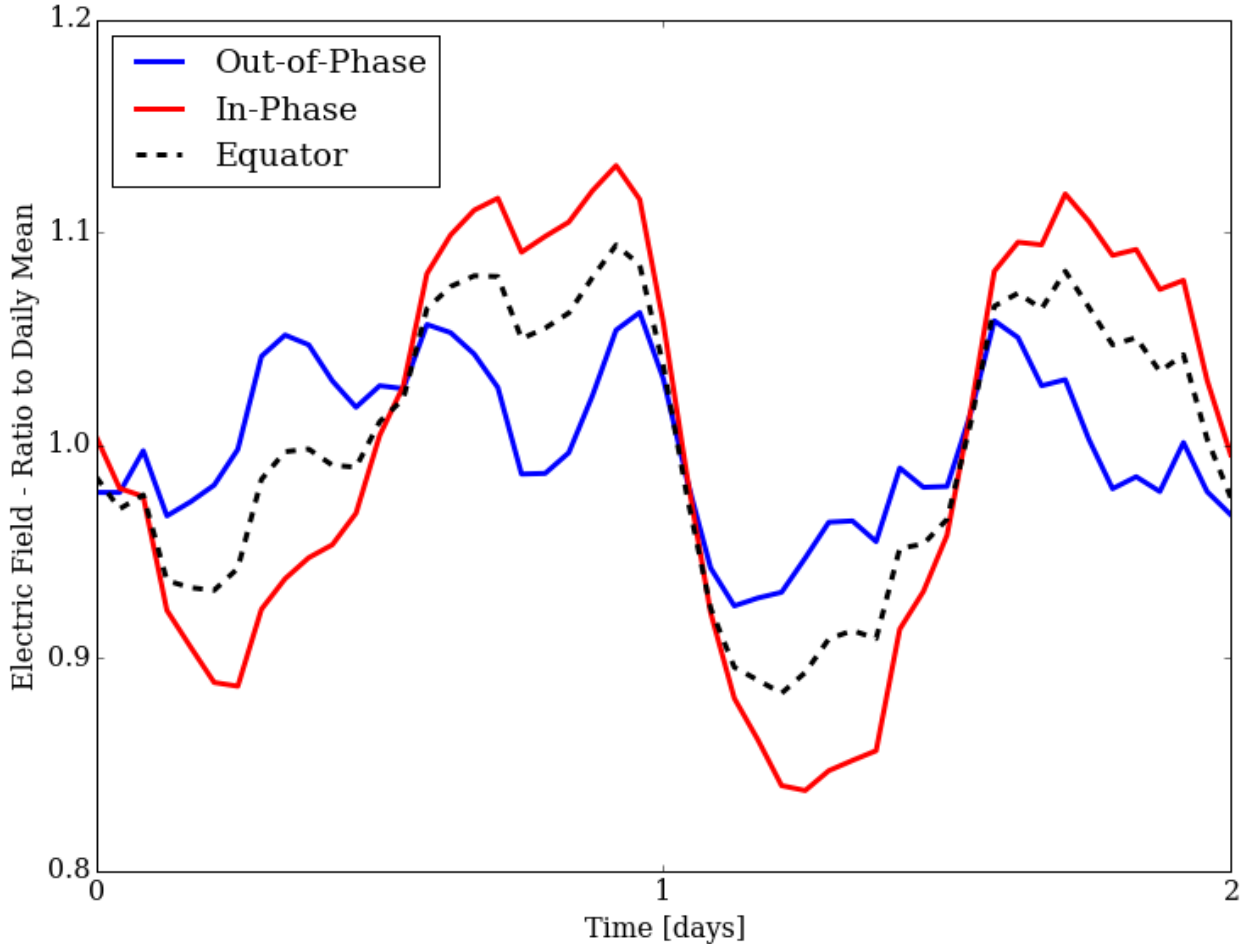


Figure 5.3: Model produced diurnal variation in electric field from two days showing the influence that in-phase (197.5E, 80.5N) (red) and out-of-phase (77.5E, 80.5S) (blue) magnetospheric potentials have on the electric fields detected at the different locations.

these specific locations. The red and blue curves constructively and destructively contribute to the GEC potential, respectively. The GEC potential varies throughout the two days due to day-to-day variability in the model's convective activity. The magnetospheric potential is also varying over the two-day period as it is a function of the geomagnetic indices throughout the two days. The geomagnetic activity conditions imposed in this simulation are considered to be quiet with a total horizontal cross-cap potential difference of about 60 kV. Under more active geomagnetic conditions, the cross-cap potential could exceed 200 kV and rival the GEC potential in certain locations at high

latitudes. Combined with dynamic conductivity behavior in the polar regions, unique conditions could setup that result in very strong or very weak regional currents.

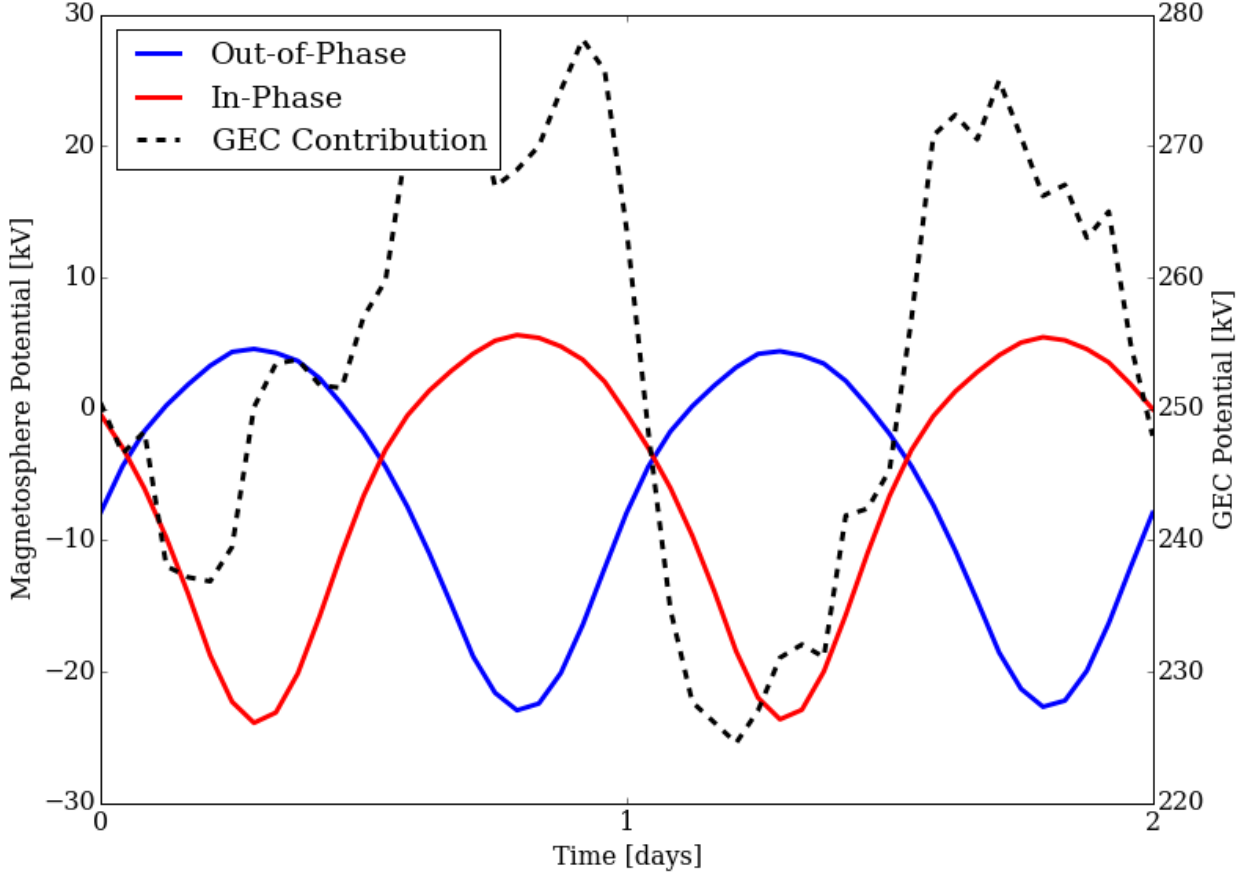


Figure 5.4: The overhead magnetospheric potential at an in-phase (197.5E, 80.5N) (red) and out-of-phase (77.5E, 80.5S) (blue) location plotted on the left axis, with the GEC current source potential (dashed-black) plotted on the right axis.

5.3 WACCM-GEC Evaluation

To determine the consistency and accuracy of WACCM-GEC, observational electric field data sets for Vostok and Concordia were obtained during common observing periods. The observational data sets used are described in more detail within section 2.2.1. WACCM-GEC was then run for this same observing period to evaluate the results under similar conditions. Within WACCM-GEC, the electric fields are represented by grid sizes that are much larger than the observations. Also, local

disturbances that influence the electric field measurements such as wind speed, clouds, temperature and humidity are not able to be resolved in the model due to the large grid sizes. However, general trends and correlations can be investigated to evaluate the model.

Data sets for each location were collected over the three month span of January-March for three overlapping years of 2009-2011 to obtain enough fair weather days for analysis. In the data sets obtained from Vostok and Concordia, the electric field was sampled at 10 second intervals. Occasionally the data would have large fluctuations due to local disturbances, and these fluctuations were filtered out to only leave fair-weather times for the analysis, as described in Burns [2005]. The data at each site was averaged over 30 minute time intervals, and a 24-hour mean was determined and centered on the time calculated. The value divided by the 24-hour mean then gave the electric field deviations for that period. WACCM-GEC was run for 30 days beginning January 1, 2010 to produce the output electric fields and currents which were then divided by the model daily mean to obtain the deviations. The mean perturbation for each 30-minute time interval was then determined and is presented in figure 5.5.

Comparing the differences between the model output and data in figure 5.5, one can see that the phase relationship of Vostok to Concordia is similar between the model and the data. This indicates that the magnetospheric potential imposed within the model agrees well with the data at those locations. One noticeable difference between the model and the data is the relative amplitude of the peaks. The model predicts a maximum of about 10-13% while the data suggests this value is closer to 20-23%. This deviation from the data suggests that the source term within the model requires further refinements, as that is the major diurnal driver for variation of the ground level electric fields. Developing a better model for source term strength from electrified clouds that includes a more detailed analysis of the ice and water pathways and other parameters within the clouds would improve the WACCM-GEC simulation and be of great value to the community. The lack of detailed meteorological and electrical measurements of clouds makes global source quantities difficult to obtain. However, the results presented are very encouraging and the broad range of

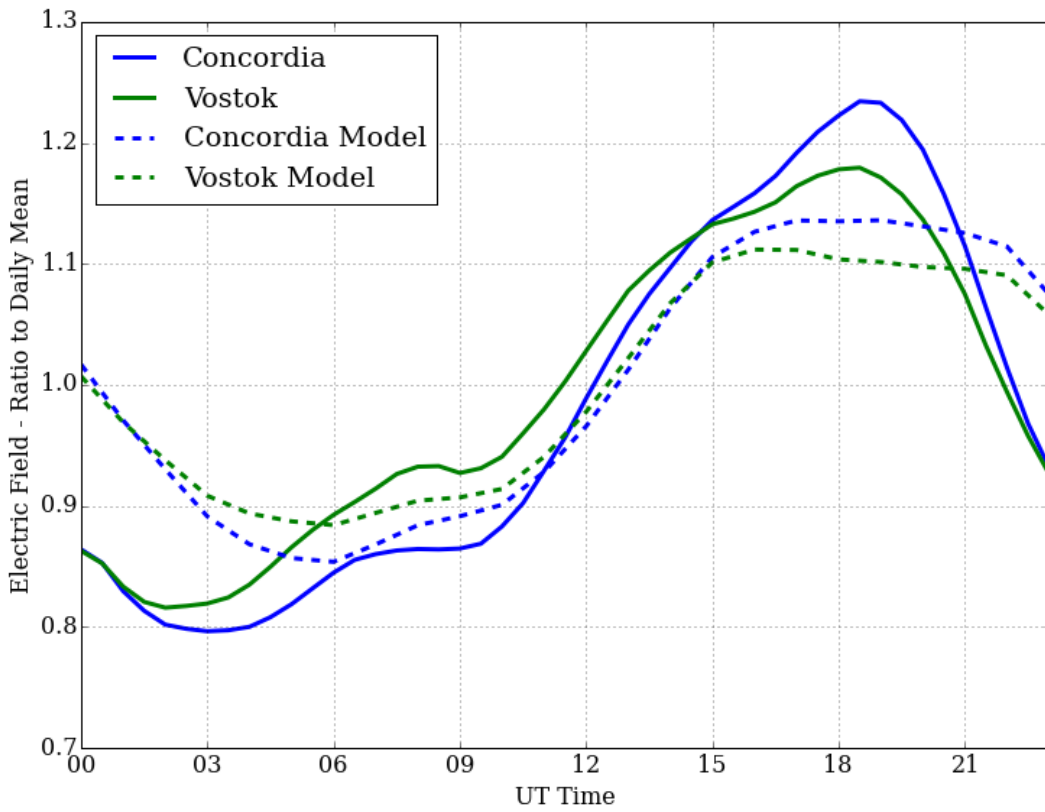


Figure 5.5: The mean diurnal variation of electric field at Vostok (green) and Concordia (blue) during January, February, March of 2009-2011. Solid lines represent the data [Burns et al., 2012] while the dashed lines represent the model output.

capability of WACCM-GEC opens a new way to study the GEC by allowing new atmospheric and electric parameterizations to be incorporated within the same consistent modeling framework.

5.4 Solar Cycle Influences on the GEC

Throughout the literature there are theories on how the sun influences climate. These are generally through direct mechanisms like solar heating influencing atmospheric dynamics. However, there are other theories on indirect mechanisms affecting climate. These indirect mechanisms involve atmospheric electric fields influencing cloud properties and attachment rates [Tinsley and Yu, 2004; Tinsley, 1996].

Measurements of the ionospheric potential have been undertaken for many decades and provide a long-term dataset of how the solar cycle influences the GEC. Previous work in the early 70s showed that the potential varies in-phase with the solar cycle [Markson, 1978; Markson and Muir, 1980]. These works relied upon measurements in the 1960s when above ground nuclear testing was going on. Recent compilations of the ionospheric potential along with the stratospheric burden of nuclear testing shows the complications that could have arisen during these measurements [Markson, 2007].

These previous theories have all been investigated with parameterizations and estimations of the electric fields within the atmosphere. With the development of the model in chapter 4, the electric fields in the atmosphere are generated in a physically consistent way. This provides a method to test how the solar cycle influences the electric fields within the atmosphere.

The energy from the solar spectrum ionizes the upper atmosphere and creates the ionosphere. These photons do not contribute significantly to ionization lower in the atmosphere, which is primarily caused by galactic cosmic rays (GCRs), discussed in detail within section 3.1.1.1. GCRs are thought to originate from supernovae within the galaxy. The GCRs are modulated by the sun's interplanetary magnetic field strength and therefore vary in opposition to the solar cycle. Figure 3.2 showed the variation of ionization rates is anti-correlated with the solar cycle.

This anti-correlation of ionization rates to the solar cycle is seen in figure 5.6. The red curve corresponds to solar maximum conditions (GCR minimum) and the blue curve corresponds

to solar minimum conditions (GCR maximum). The atmosphere is more conductive in the lower atmosphere during solar minimum.

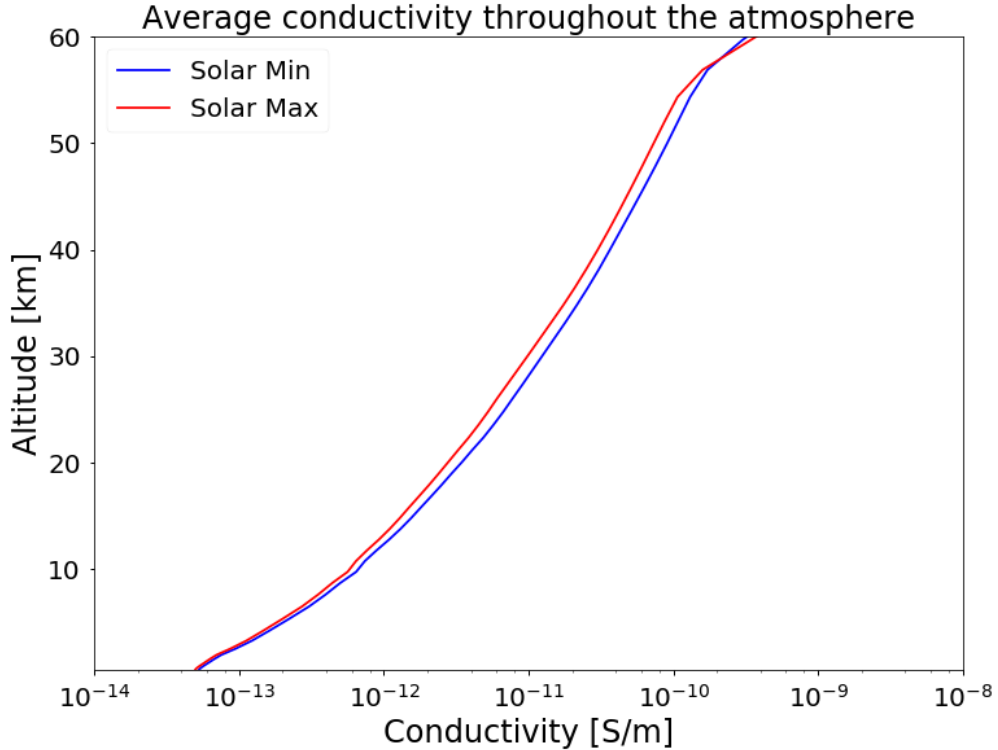


Figure 5.6: Average conductivity throughout the atmosphere for solar minimum (GCR maximum) in blue and solar maximum (GCR minimum) in red. The lower atmosphere is more conductive during solar minimum conditions.

Although the conductivity profiles in figure 5.6 do not appear that much different, the integrated effect of the small deviations over the globe leads to a reduced total resistance during solar minimum. The total resistance of the atmosphere for solar minimum and maximum is shown in figure 5.7. The seasonal trend is similar but there is an offset of 20Ω between solar minimum and maximum. With the total resistance being around 200Ω that leads to roughly a 10% variation in total resistance over the course of a solar cycle.

The current variation over the course of a year is shown in figure 5.8. There is much larger daily variations in the total current than the total resistance and therefore a 15-day rolling mean was applied for figure 5.8. There is more current production in 1997 (solar minimum) than 1991

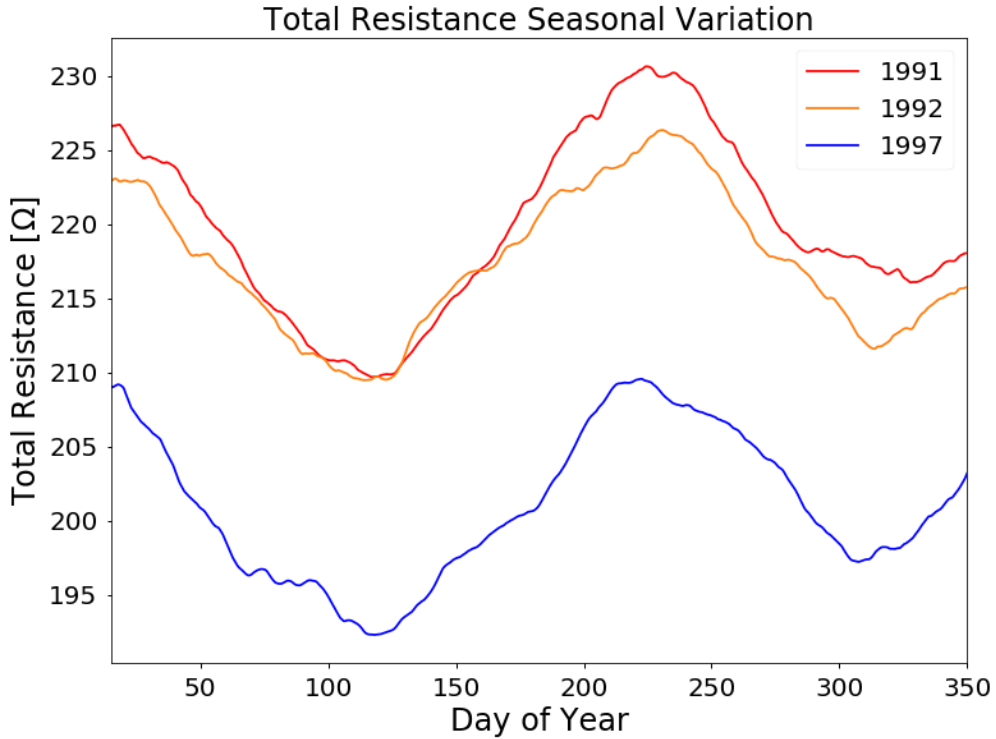


Figure 5.7: Total resistance over the course of a year for solar maximum (GCR minimum) conditions in red/orange and solar minimum conditions (GCR maximum) in blue. The seasonal cycle of total resistance is similar, but the total resistance is about 20Ω lower during solar minimum. The resistance is plotted with a 15-day rolling mean.

(solar maximum), which is the opposite variation of the total resistance. The source production is so variable during this time that it is hard to draw a direct conclusion on the impact of the GCRs on source strength.

Comparing the variations over multiple years is complicated by the inter-annual variability of all the model variables. To reduce this complexity, the model variables can be isolated to determine the impact from a single variable. To investigate the impact of different GCR ionization rates on the GEC, the model run from 1997 (solar minimum) is utilized as the base state. Without modifying any of the microphysical variables, the GCR ionization rate is changed with the 1991 (solar max) ionization rates. The new ionization rate, q , for modeling solar maximum conditions during the solar minimum run of 1997 is

$$q = q_{1997} - q_{1997\text{ GCR}} + q_{1991\text{ GCR}}, \quad (5.3)$$

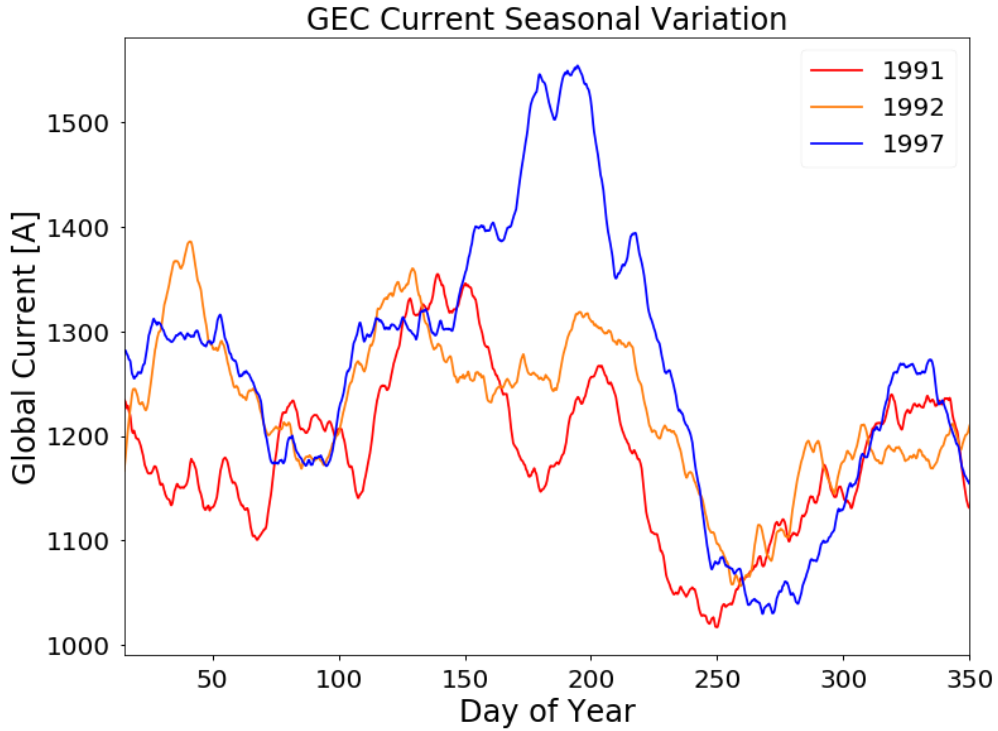


Figure 5.8: 15-day running mean of the total current within the GEC over the course of a year for the 1991/1992 solar maximum (GCR minimum) conditions in red/orange and the 1997 solar minimum conditions (GCR maximum) in blue. There is more total current production during 1997 compared to 1991/1992.

where q_{1997} is the total ionization rate from 1997, $q_{1997 GCR}$ is the ionization rate from GCRs in 1997 and $q_{1991 GCR}$ is the ionization rate from GCRs in 1991. After changing the GCR flux, all of the conductivity, source current, and potentials are recomputed.

The impact of a direct change in ionization rate can now be investigated. Through Ohm's law, the 10% variation in total resistance seen in figure 5.7 will lead to a variation in potential of the ionosphere of 10% if applied directly. However, the use of a coupled global model and the derivations within section 3.2.2 show that the column resistance within the source columns also modifies the amount of current that is produced within the GEC. The variations of both the current and resistance need to be investigated together to determine the influence on the circuit.

Figure 5.9 shows the percent change in the GEC current, potential, and resistance from going to solar max conditions from solar min. The resistance is changed by around 9% that was seen

in figure 5.7 as well. However, now that the GCR change is isolated, the source currents have decreased by 1%. This leads to the potential being increased by 8% during solar max conditions relative to solar min conditions.

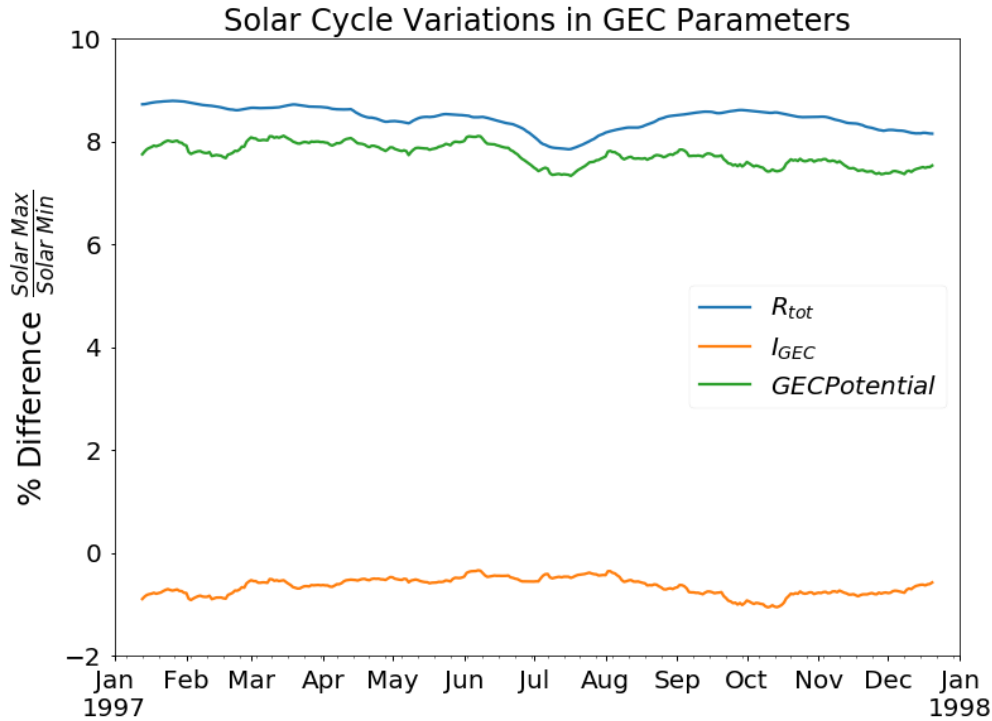


Figure 5.9: 15-day running mean of the percent change in GEC parameters over the course of a year going from 1997 solar minimum conditions to 1991 solar maximum conditions. The only parameters changed within the model is the ionization rate from GCRs. This causes a change of 8% in the GEC potential.

The predictions of variations of the GEC with solar-cycle at first glance appear to be intuitive by looking at the total resistance variations caused by the GCR flux variations in figure 5.7 which showed a lower total resistance during solar minimum. Looking at the variations of all GEC parameters in figure 5.9 showed that the resistance and potential increase during solar maximum while the GEC current decreases during solar maximum.

The current variations shown in figure 5.8 are highly variable inter-annually. The inter-annual variation leads to difficult interpretations relative to the total resistance which is more stable and has a distinct variation with the solar cycle. To remove the inter-annual variability confusion, the

ionization rate due to GCRs were changed from solar min to solar max conditions with the same background meteorology. Isolating the GCR flux identified an 8% change in potential from solar minimum to solar maximum. The variation in potential is correlated with the solar cycle which disagrees with the work of Slyunyaev et al. [2015] who found that there is only a minimal 5% variation in the potential anti-correlated with the solar cycle. This work also showed that there is a lot of inter-annual variability in the current sources that dominates the changes caused by the solar cycle. This is likely the reason for the confusion within the literature on the interpretation of solar cycle dependencies within the GEC.

5.5 Volcanic Eruptions Influences on the GEC

When volcanoes erupt there are plumes of ash that can be injected all the way into the stratosphere. There is a wide size distribution of aerosols within the ash plume and the smaller aerosols can be relatively long-lived, lasting months in the stratosphere and getting spread across the globe. These ultra-fine, long-lived aerosol particles are expected to increase the atmospheric resistance due to attachment to ions [Tinsley et al., 1994]. Timmreck [2012] discuss how the ultra-fine aerosol concentrations are overestimated in models due to underestimation of coagulation. WACCM has recently been updated to provide realistic aerosol distributions from historic volcanic eruptions [Mills et al., 2016; Neely III et al., 2016]. To determine the impact of volcanic eruptions on the GEC, an investigation into the Pinatubo eruption of June 1991 is performed.

The Pinatubo eruption was a significant modern explosive volcanic eruption that ejected ash into the stratosphere. The volcano is located at low latitudes in the Philippines. Because of the explosive nature of the volcano, some of the aerosols released in the eruption made it into the stratosphere and were distributed globally. WACCM-GEC was initialized and run for the year of the Pinatubo eruption, 1991. After the model had established a baseline state, two separate scenarios were initialized on June 1st, 1991. The first scenario contained the explosive eruption from Pinatubo. The second scenario did not contain the Pinatubo eruption. The eruption on June 15th caused a significant change in the aerosol attachment rate shown in figure 5.10. This figure

illustrates the difference between the run with Pinatubo erupting and the run without Pinatubo. There is an increase in the globally averaged aerosol attachment rate of around 1 mHz at a 15 km altitude. The aerosol attachment rate above 10 km stays elevated compared to the no volcanoes run even months after the eruption.

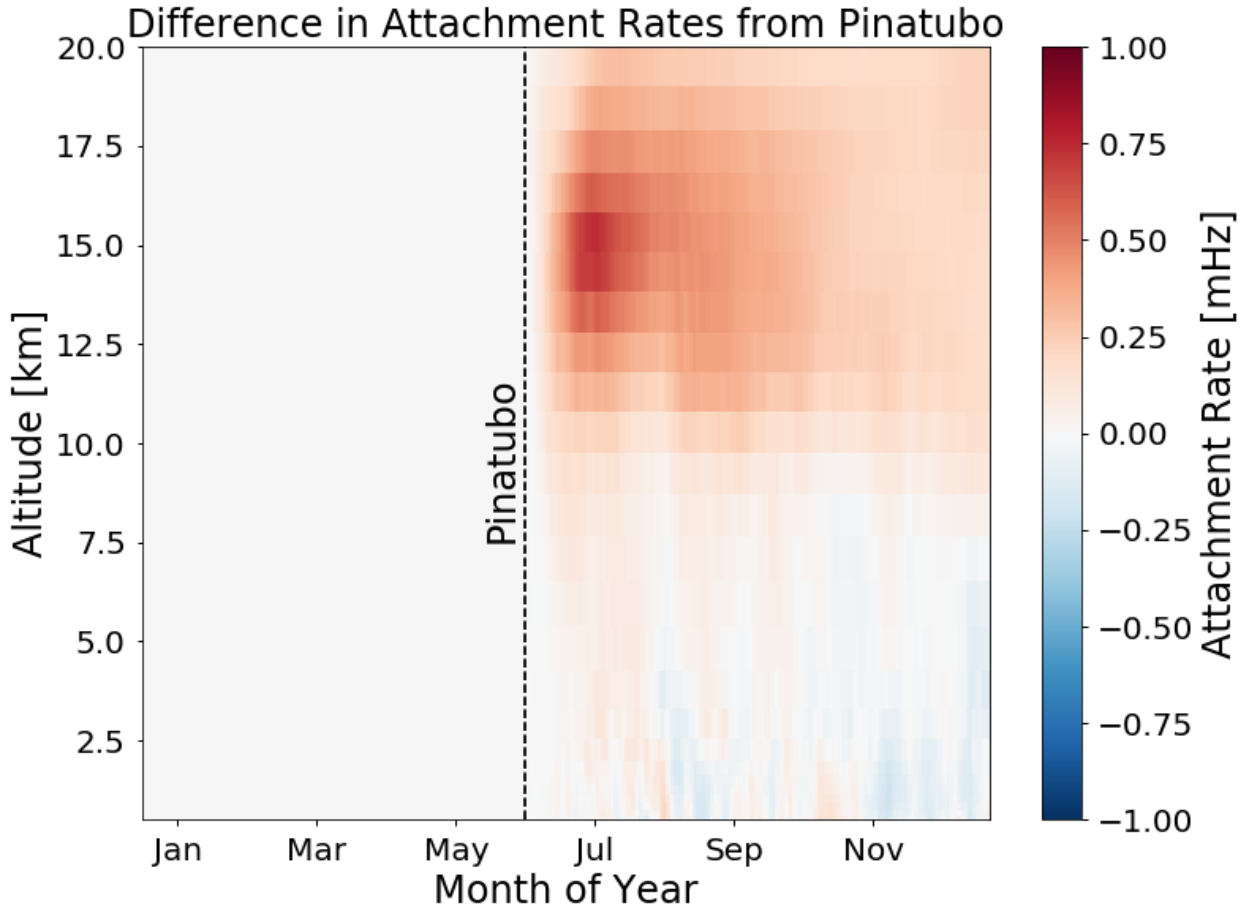


Figure 5.10: Difference in attachment rate between Pinatubo and no volcanoes. The Pinatubo eruption causes an increase in the ion-aerosol attachment rate that extends up to 20 km.

The initial eruption causes local increases in the attachment rates which takes months to spread to higher latitudes. Figure 5.11 shows the spread of these aerosols to higher latitudes as an average of the attachment rate over longitude and altitude. This is evidence of the circulation patterns that redistribute the aerosols to higher latitudes.

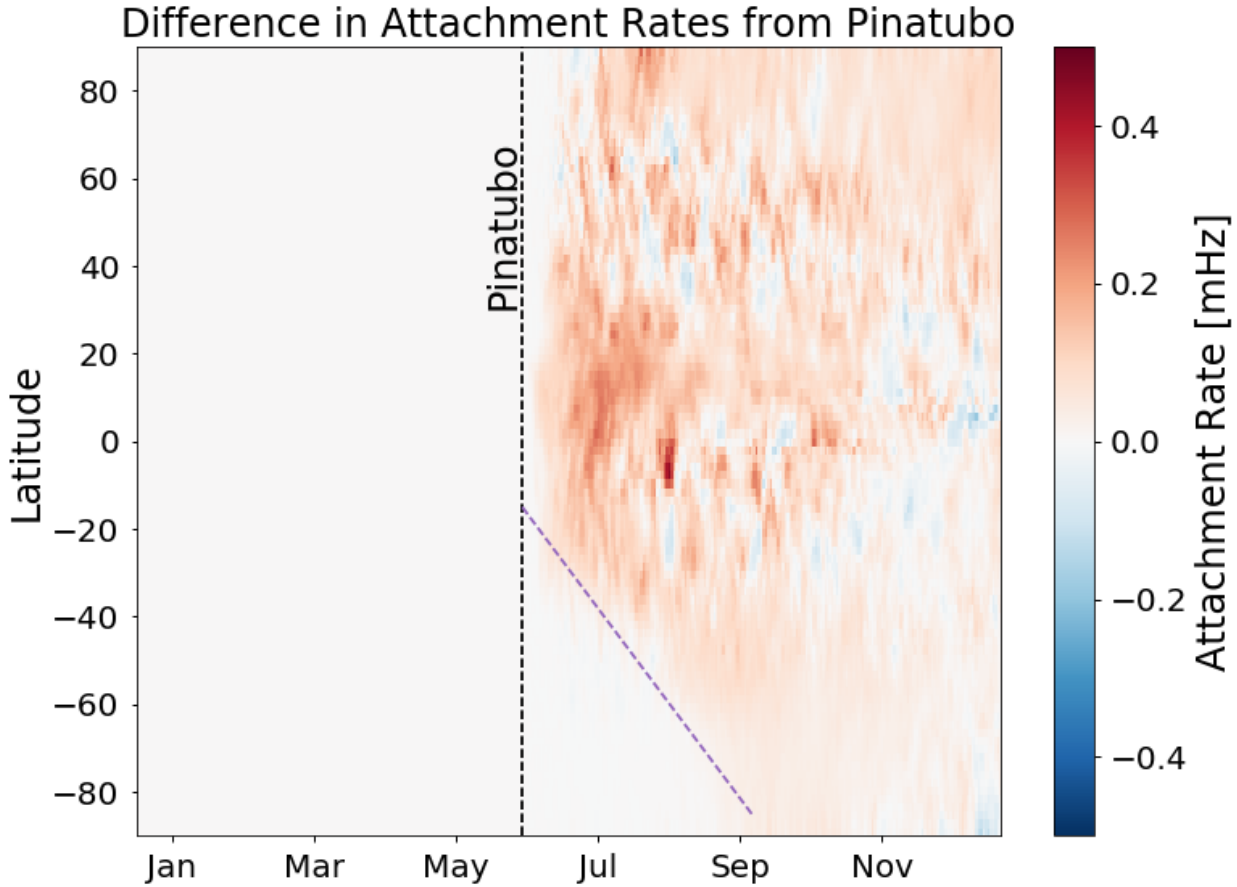


Figure 5.11: Difference in attachment rate between Pinatubo and no volcanoes. The Pinatubo eruption causes an increase in the ion-aerosol attachment rate locally. The aerosols are then transported in the model to higher latitudes over time as shown by the purple dashed lines.

The previous figures showed changes in the aerosol attachment rates caused by the Pinatubo eruption. The attachment rates discussed in section 3.1.2.2 act to remove ions from the atmosphere making it more resistive. In addition to making the atmosphere more resistive, the source current to the GEC is modified by this changing resistance. If the resistance between the dipoles is increased the storms will become more efficient and contribute more current globally. Figure 5.12 shows the differences in the total resistance between the Pinatubo eruption case (blue) and the no volcanoes case (orange). There is a relatively small impact on the total resistance of the atmosphere even though there are changes in the aerosol attachment rates. This is explained by the attachment rates being changed in the stratosphere where the contribution to the total column resistance is

small. The most noticeable difference caused by Pinatubo is the earlier increase in total resistance of the atmosphere.

The total resistance shows little change even with one of the most significant eruptions of the modern era. Total resistance is the most obvious way to impact the GEC from aerosols but it is not the only method. Another aspect of the GEC is the source contribution to the total potential that was discussed in section 3.2. With the implementation of the resistance ratio discussed in section 3.2.2, the source contribution current can be modified if the resistance is changed in the atmospheric column where storms are occurring. The resistance modification can be between the dipoles or above/below the storm. The total source contribution current from the two scenarios is shown in figure 5.13. The influence of aerosols on the source contribution current also appears to shift the current earlier in time similar to the total resistance in figure 5.12.

The timing of the peak total resistance obtained from the different model simulations is an interesting result from using the climate model. If the aerosols only influenced the attachment rates in the electric circuit then there would only be a change in the magnitude of the curves, rather than the phase shift. The climate model includes aerosol feedbacks on the cloud microphysics. This feedback mechanism modifies the timing of clouds and other parameters within the model. This is one of the major advantages of utilizing a climate model.

With the complicated nature of the climate model it is difficult to determine what the impact from aerosols are on the parameters of the GEC. The isolation of the electric circuit components are accomplished by using the no volcanoes run as a base state. This run is then modified by the aerosol attachment rates from the Pinatubo run, but all of the microphysics and dynamics within the simulations remain the same. The ion aerosol attachment rate is modified to create a new ion-aerosol attachment coefficient that was discussed in section 3.1.2.2.

$$\beta_{aerosols} = (\beta_{Pinatubo} - \beta_{no\ volc}) M + \beta_{no\ volc} \quad (5.4)$$

In this equation, the base state, $\beta_{no\ volc}$, is used to get the background aerosol concentration and then the aerosol attachment rate from Pinatubo, $\beta_{Pinatubo}$, is added in to get the new attachment

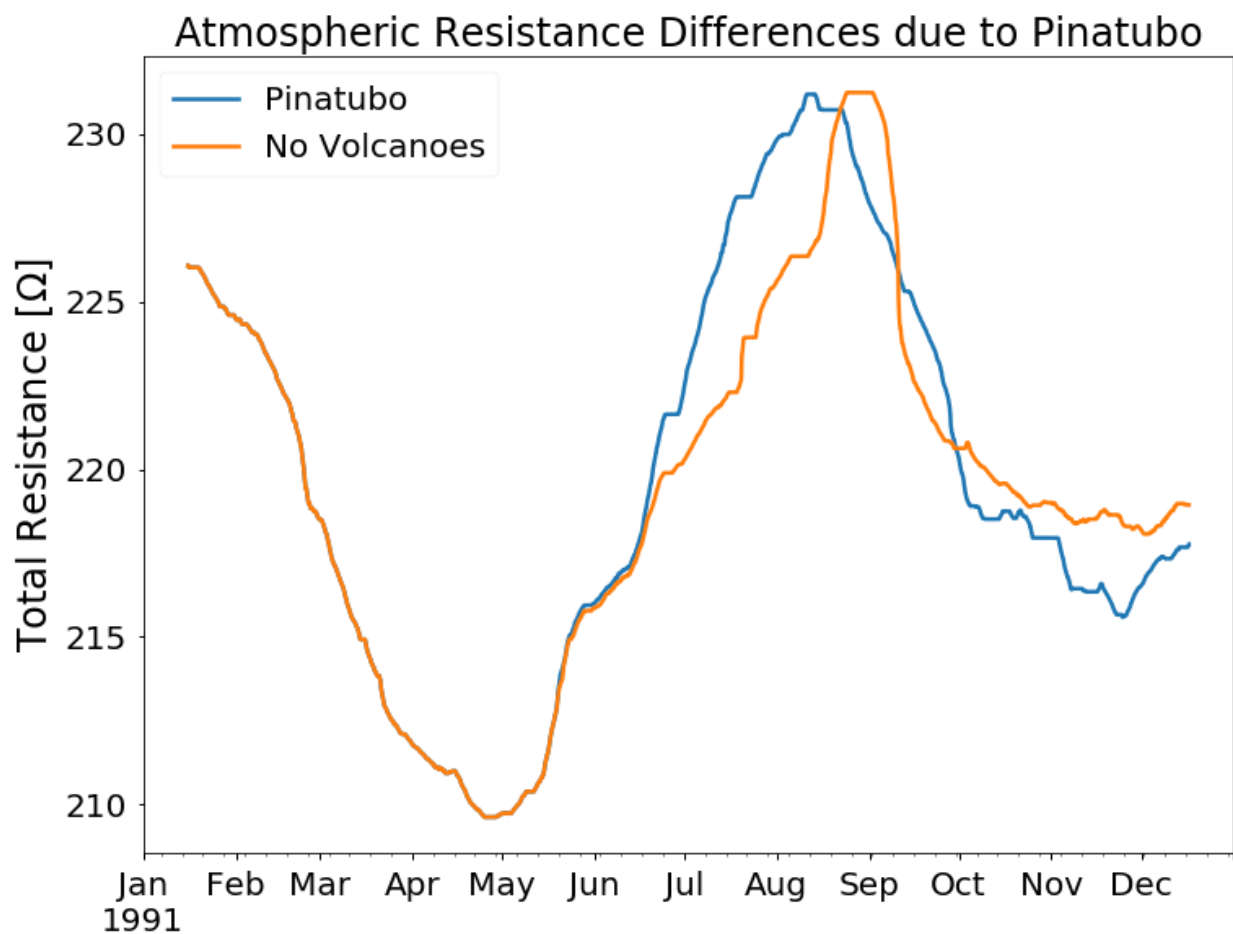


Figure 5.12: Difference in total resistance between Pinatubo (blue) and no volcanoes (orange). The resistance increases sooner when Pinatubo occurs, but does not increase the overall magnitude of total resistance over the course of the year.

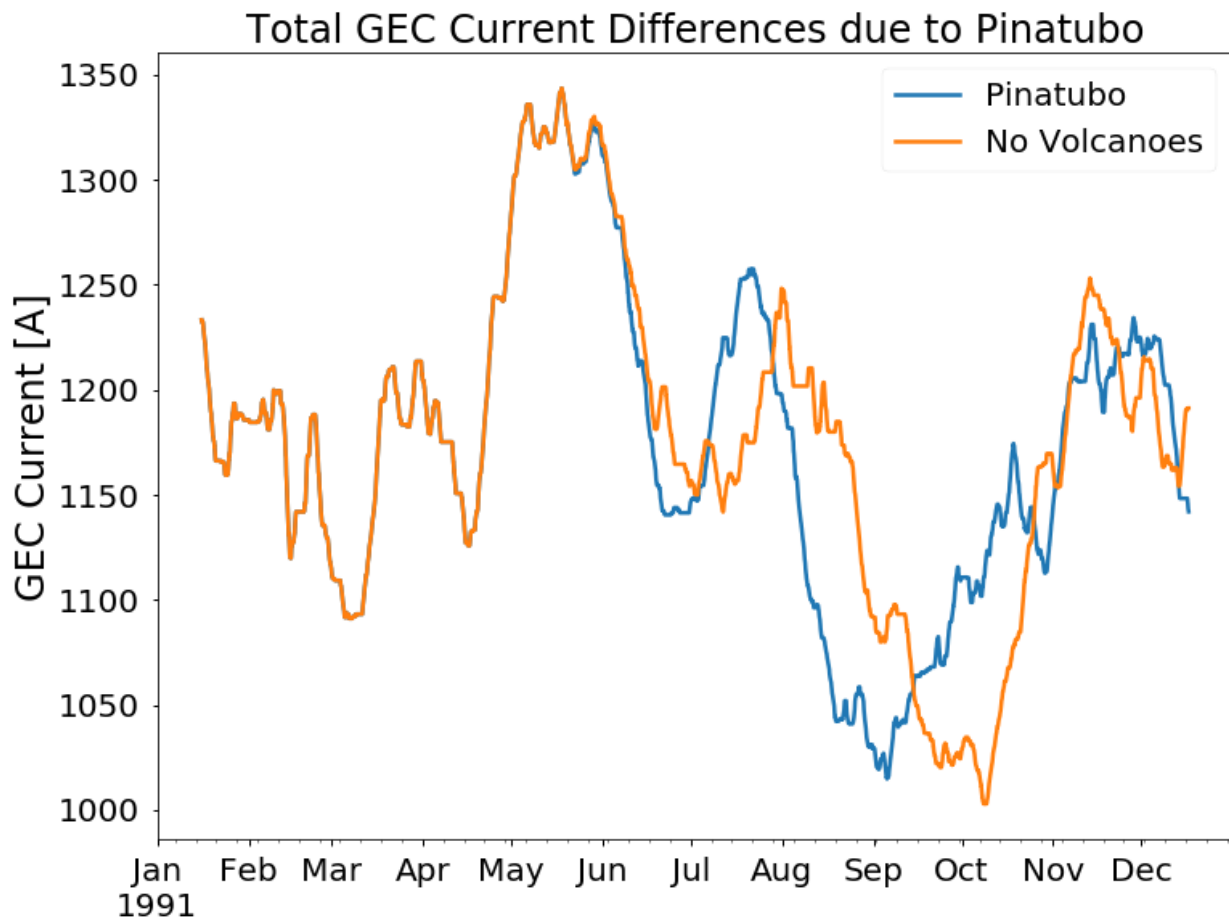


Figure 5.13: Difference in the GEC contribution current between Pinatubo (blue) and no volcanoes (orange). The Pinatubo eruption causes the source currents to shift earlier than in the no volcanoes case, but has little impact on the overall strength of the current sources.

rate, $\beta_{aerosols}$. In the equation M is a multiplier to increase the aerosol attachment rate to simulate larger volcanic eruptions, it is equal to 1 in the normal Pinatubo run. The use of this aerosol modification simulates the influence of aerosols without any microphysics coupling in the model. The influence of several aerosol concentrations on the total resistance of the GEC from the volcanic aerosols is shown in figure 5.14. The Pinatubo size eruptions do not significantly change the total resistance which was also shown in figure 5.12. In this figure, the multiplier M from equation (5.4) is set to 10 and 50 to simulate larger volcanic eruptions as well. With the 50x greater aerosol concentration the total resistance of the atmosphere is increased by 80%.

The aerosol attachment rate is changed throughout the domain with addition of the volcanic aerosols. This in turn modifies the conductivity and resistance of the atmosphere. Depending on where these aerosols are in altitude relative to the storms dictates whether the storm is going to contribute more or less current to the global circuit. This is accounted for in the model with the use of a ratio of resistances between the storms dipole centers and the resistance of the total column, called the resistance ratio, R_{ratio} , in section 3.2.2. Figure 5.15 shows that the GEC current decreases by 30% in the 50x volcano simulation. Modification of the conductivity and resistances directly was done without considering any feedback mechanisms from the aerosols on the microphysics and dynamics of the atmosphere.

The Community Earth System Model (CESM) is a sophisticated climate model that incorporates aerosol interactions with the microphysics. More detail on the complex interactions between aerosols and clouds and a description of the feedback mechanisms that are included can be found in Gettelman et al. [2013] and Gettelman et al. [2014]. Incorporating the microphysics feedback from aerosols (red curve) has a major impact on the current production. There are significant variations in the total current production, showing periods of both increased and decreased current relative to the no volcanoes case. This shows that WACCM-GEC is tightly coupled to the variables within the climate model, and that the impact of the aerosols on the microphysics and dynamics modifies the properties within the GEC more than just accounting for the aerosol impact on the electrical properties of the circuit.

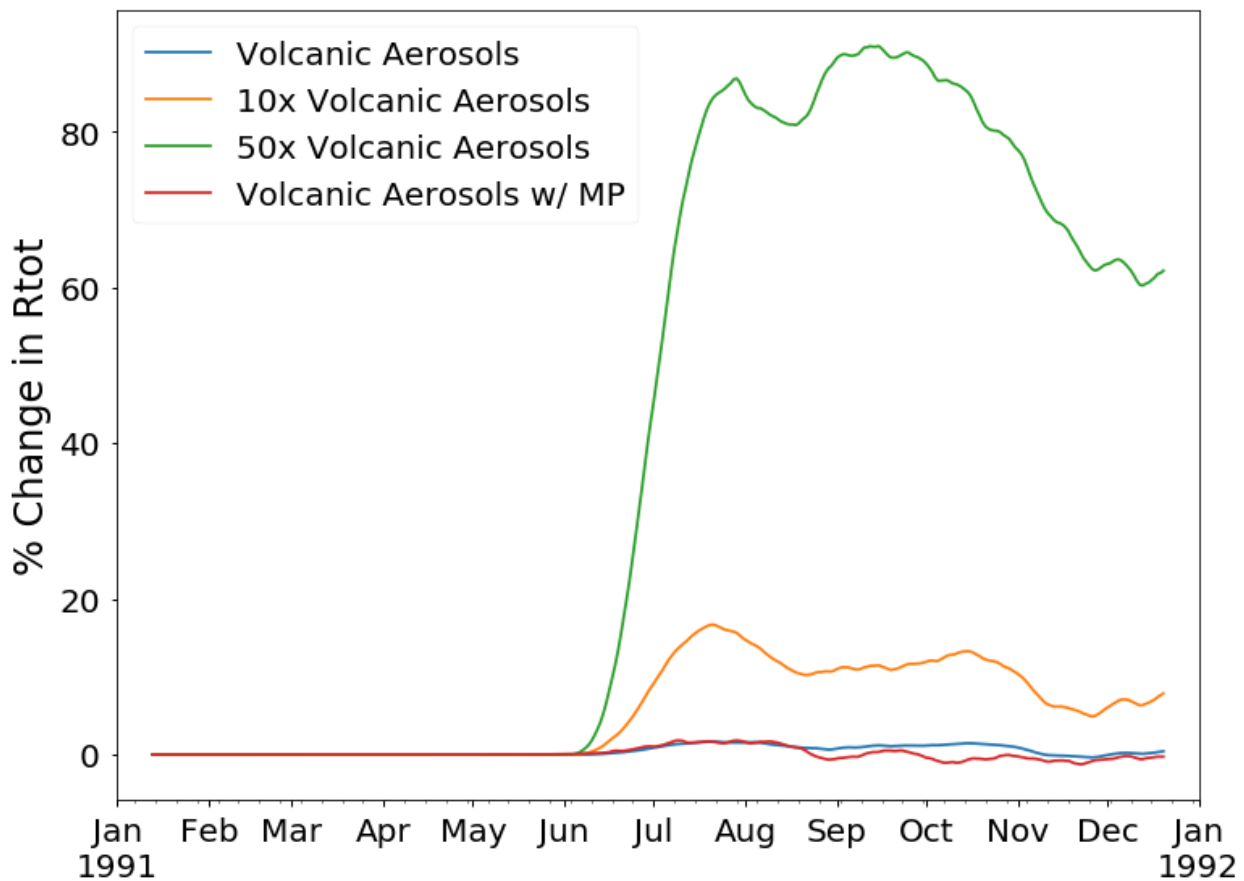


Figure 5.14: Changes in total atmospheric resistance from different volcanic aerosol amounts. The volcanic aerosols are from Pinatubo with no aerosol microphysics feedback going on. These aerosols are increased by a factor of 10 and 50 to determine the impact of larger volcanoes on the GEC. Turning the aerosol microphysics feedback on (red curve) changes the timing of the resistance, but the magnitude from a Pinatubo sized eruption is minimal.

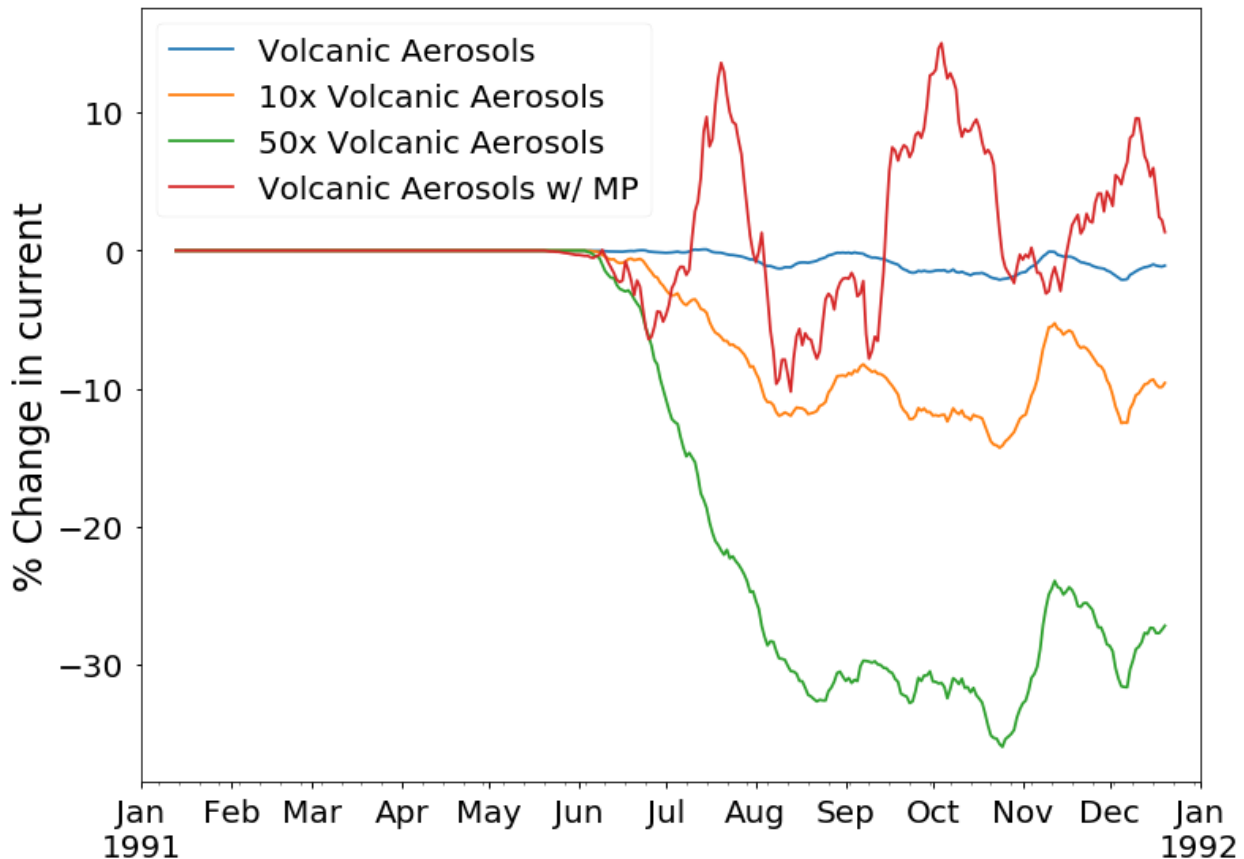


Figure 5.15: Changes in total GEC current from different volcanic aerosol amounts. The volcanic aerosols are from Pinatubo with no aerosol microphysics feedback going on. These aerosols are increased by a factor of 10 and 50 to determine the impact of larger volcanoes on the GEC. Turning the aerosol microphysics feedback on (red curve) changes the timing and magnitude of the source currents.

The current and resistance within the circuit are both modified by the volcanic aerosols within the circuit. Investigating the impact of these two parameters on the total potential of the ionosphere determines how much return current will flow through the circuit. Incorporating the change in current and resistance together with Ohm's law gives the change in potential shown in figure 5.16. The GEC potential is increased by up to 40% with a volcano 50 times bigger than Pinatubo, but not significantly changed for a Pinatubo size eruption unless microphysical feedbacks are accounted for. Incorporating the feedbacks from microphysics leads to a varying potential after the eruption of up to 10%.

These runs are the first to realistically model the influence of a volcano on the GEC. The impact of Pinatubo on the GEC is relatively minor when investigating the change in total resistance and potential of the GEC. There are even more significant volcanic eruptions in historical times that could produce a much more significant impact on the GEC, as shown with the 10 and 50 time Pinatubo runs. Incorporating the large volcanic aerosols into the model neglected the microphysical feedbacks of such large aerosol loads in the atmosphere. Future work could be done to investigate the impact of these large volcanic eruptions on cloud formation and dynamical mechanisms using the same methodology as the normal sized Pinatubo eruption with microphysics feedbacks. This indirectly leads to changes in the properties of the GEC rather than the direct impact of changing ion-aerosol attachment rates that was done in this study. Incorporating the microphysics feedbacks requires new simulations to be run, which are computationally expensive, whereas the simplified equivalent circuit impacts require no additional computation time.

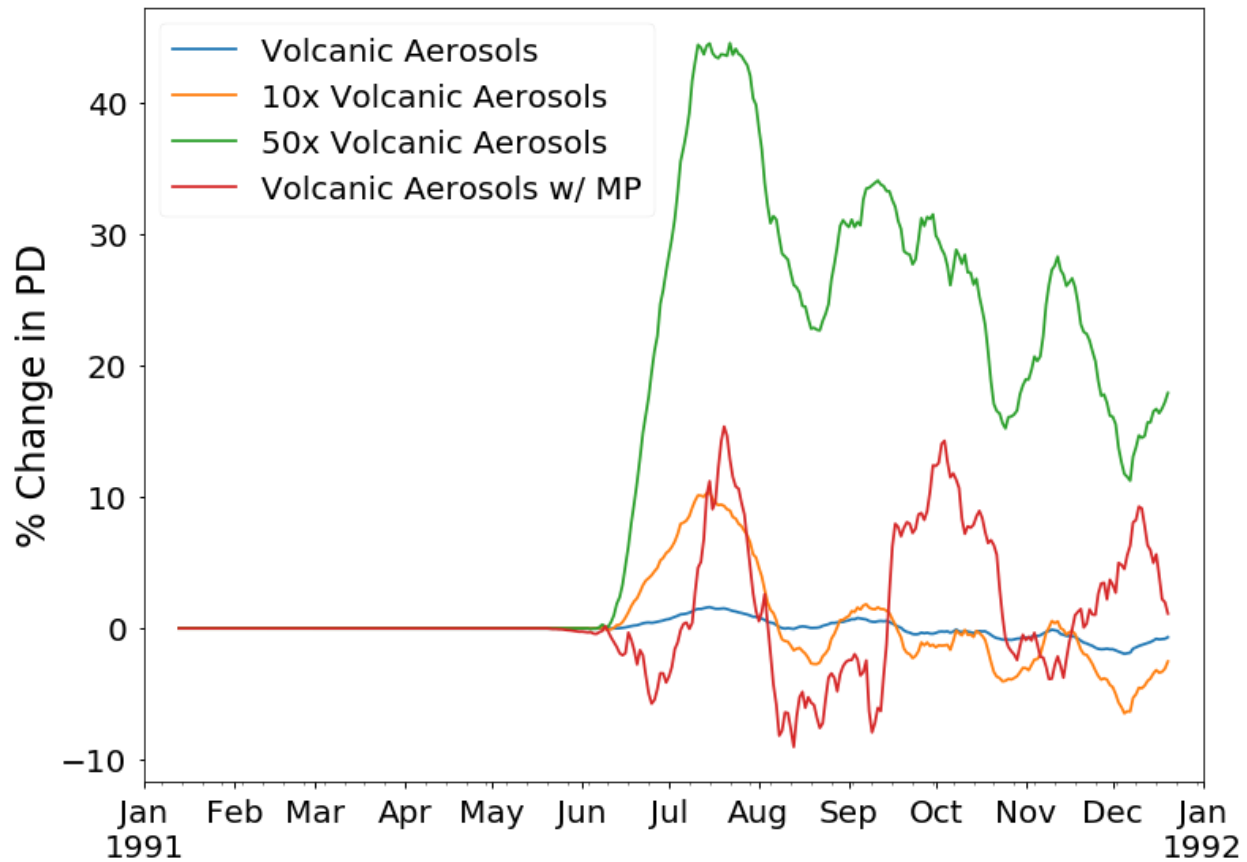


Figure 5.16: Changes in the GEC potential from different volcanic aerosol amounts. The volcanic aerosols are from Pinatubo with no aerosol microphysics feedback going on. These aerosols are increased by a factor of 10 and 50 to determine the impact of larger volcanoes on the GEC. Turning the aerosol microphysics feedback on (red curve) changes the timing and magnitude of the change in GEC potential.

5.6 Seasonal Variations

In addition to the diurnal and solar cycle variations there have been investigations into seasonal variations [Burns et al., 2012; Burns, 2005; Blakeslee et al., 2012; Lucas et al., 2017] with different trends seen at different locations. The global model provides a method to analyze whether the seasonal variations are due to seasonal changes in local meteorology that manifest themselves in the local electric field, or some seasonal trend in the GEC variables.

To investigate the seasonal variations, a free running simulation of WACCM-GEC was run for 1991-1992 and 1997. This run produced the currents, electric fields and resistances globally at every model time step and grid point. As discussed in section 5.4, the resistance is the most stable measurement over the course of time with relatively little variation on the day-day timescales. The mean variation in column resistance over latitude and time is shown in figure 5.17. There is a very distinct dependence on the latitude as to what seasonal cycle is seen. The northern high latitudes have more resistance in the northern hemisphere summer and less resistance in the winter, while the southern latitudes are the opposite with lower resistances during northern hemisphere summer and higher resistances during northern hemisphere winter.

The column resistance dependence on latitude indicates that there will also be seasonal variations in the current density in fair-weather regions. The current density, J_z , within each column is a function of the total potential over that column, PD , divided by the column resistance, R_{col} as defined in equation (4.5). The current density within each column will be a combination of the seasonal variations in potential and column resistance. Figure 5.18 shows an inverse relationship to the column resistance in figure 5.17 and less defined structure compared to column resistance due to the incorporation of the potential which is more variable in time.

The current density has been measured and removes local influences from the measurements, but more data is available from electric field mills. Therefore the seasonal variations in electric field need to be investigated. The electric field is related to the current density divided by the local conductivity through equation (4.6). Due to the coupling of all the different seasonal trends in the

Column Resistance Variations

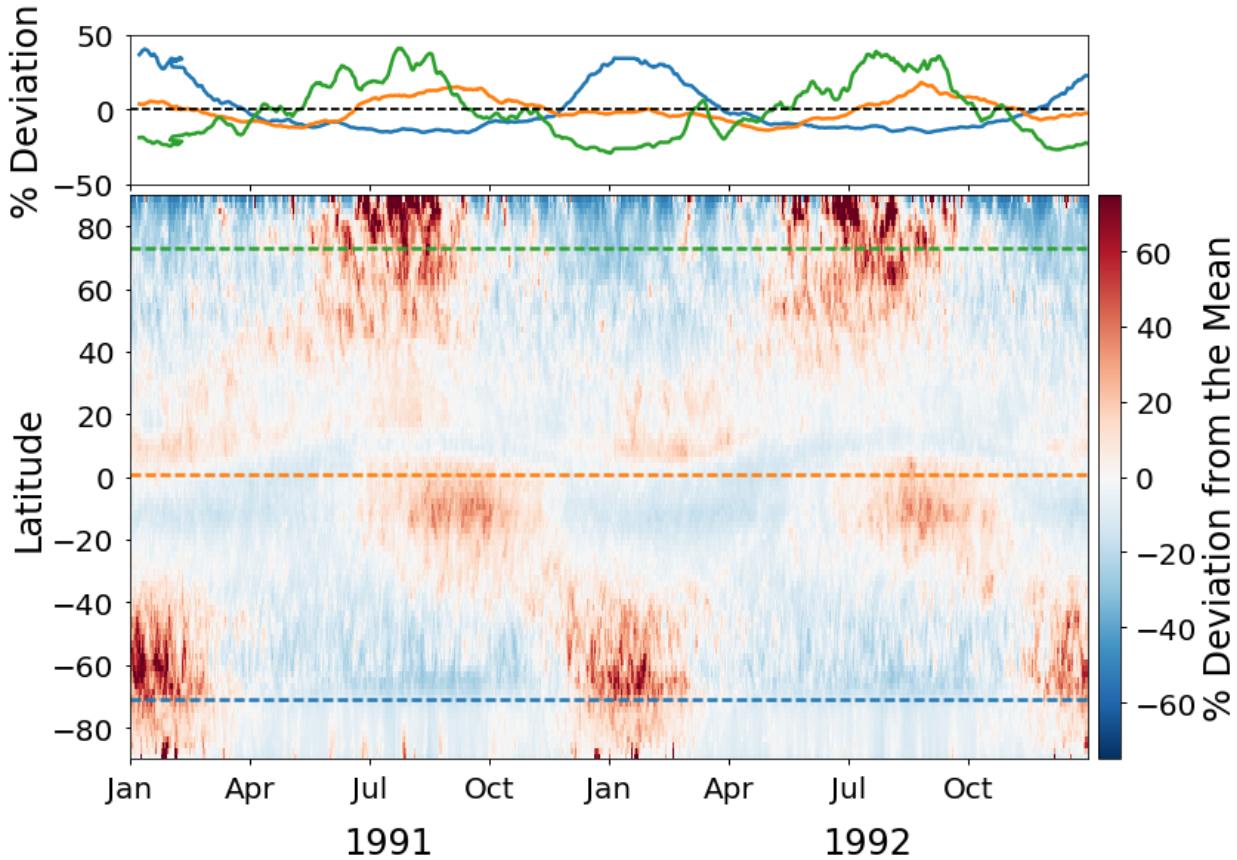


Figure 5.17: Column resistance deviations from the mean over 1991 and 1992. There is a distinct seasonal trend that is opposite in the northern hemisphere and southern hemisphere. The northern hemisphere has more resistance in the summer and lower resistances during the winter. The green, orange, and blue dashed lines correspond to the curves in the top plot.

variables there is more spatial variability associated with the surface electric fields. Most of the variations seen in figure 5.19 is reduced compared to the variations seen in the current density and column resistance, except at high northern latitudes. This reduction in seasonal variation can be explained through the destructive interference of the signals from the current density and the local conductivity which is involved in the calculation of the column resistance.

The years 1991-1992 had influences on the GEC due to the eruption of Pinatubo in 1991 as discussed in section 5.5. Due to the volcanic aerosols having unknown microphysical influences

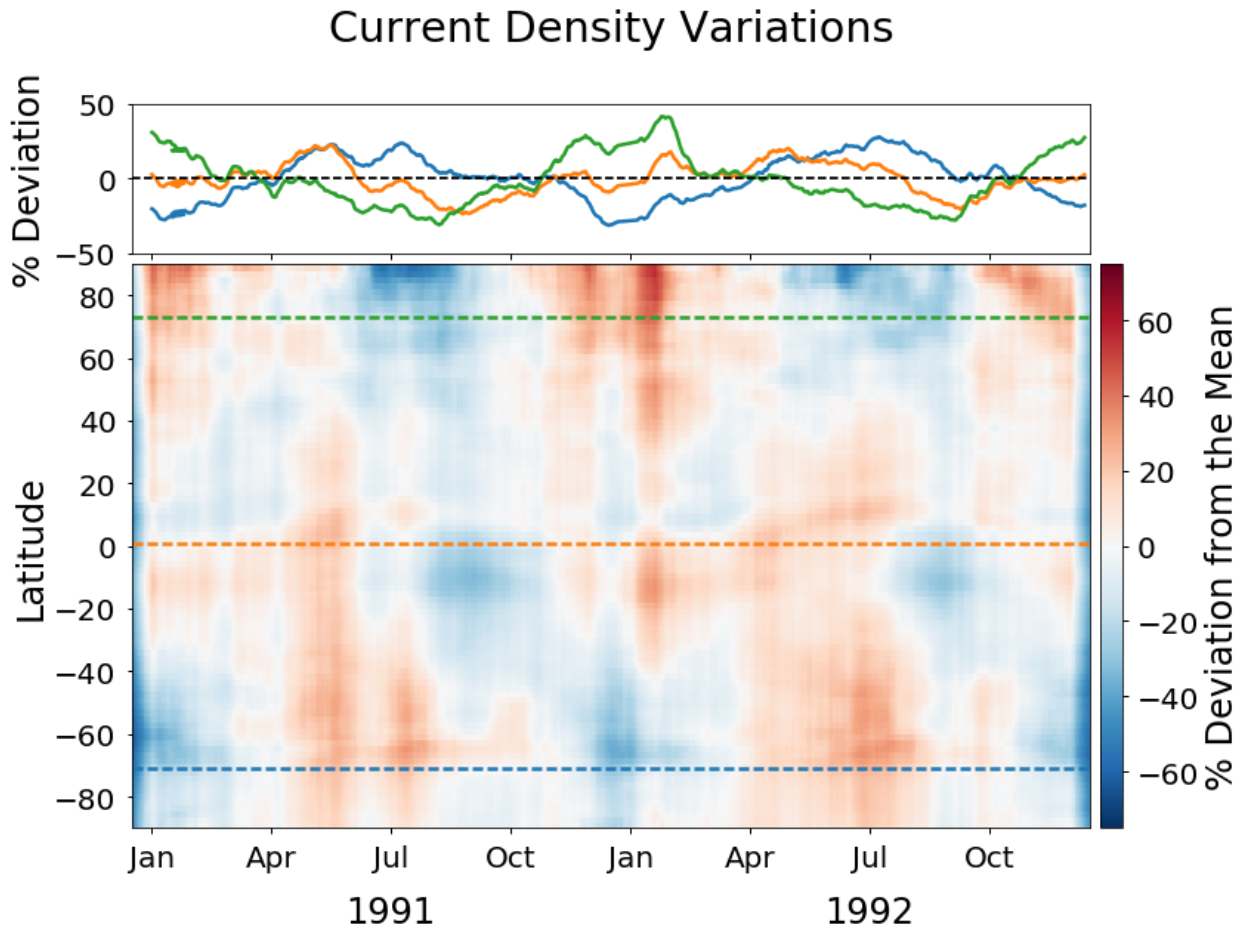


Figure 5.18: Current density deviations from the mean over 1991 and 1992. There is a distinct seasonal trend that is opposite in the northern hemisphere and southern hemisphere. The current density signal has an inverse signal to the column resistance and also has a seasonal variation from the potential are also incorporated. The green, orange, and blue dashed lines correspond to the curves in the top plot.

on the properties of the model runs, a run was performed for 1997 as well to determine what the seasonal variations would be when aerosols are less prevalent.

The column resistance shown in figure 5.20 has the same general trend as figure 5.17 with more resistance in northern hemisphere summer and less resistance in northern hemisphere winter.

The current density in figure 5.21 is more structured than figure 5.18 having an opposite trend to the column resistance.

Surface Electric Field Variations

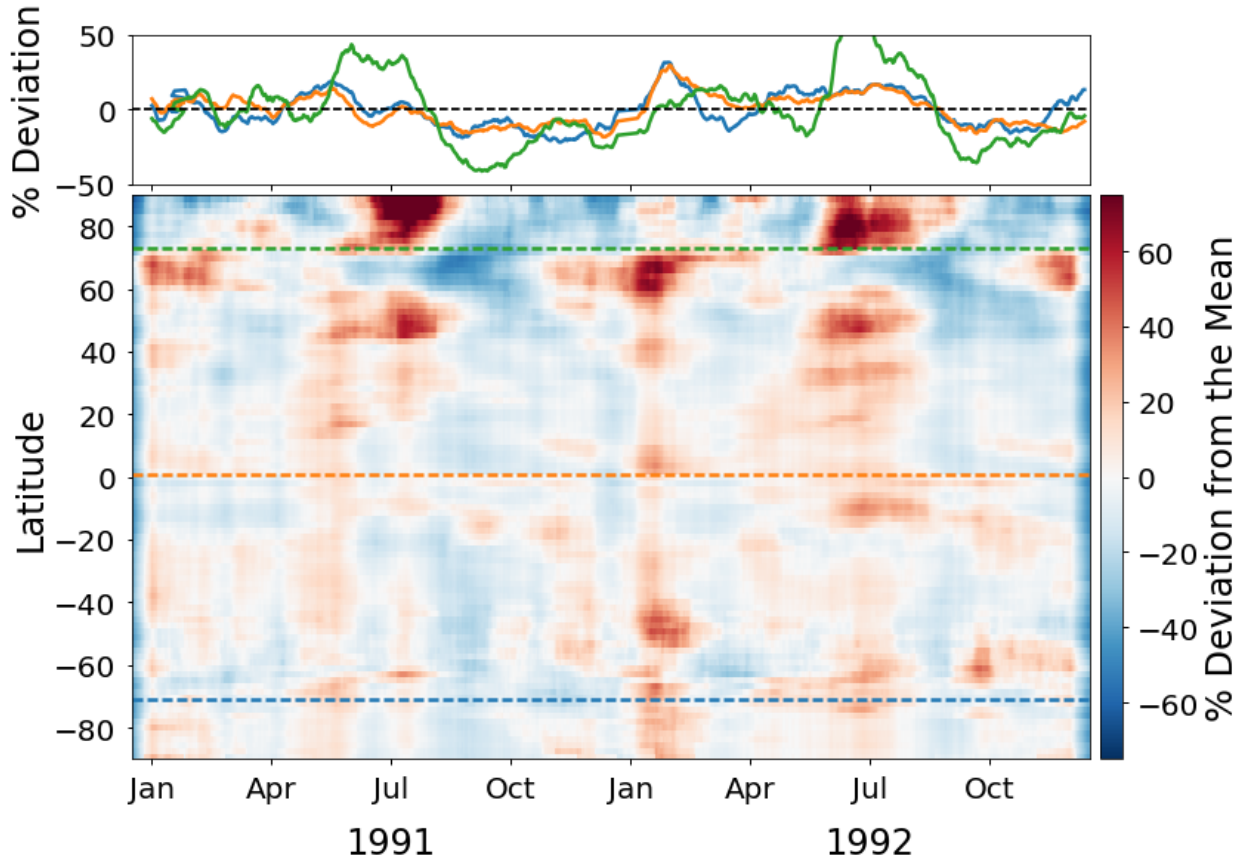


Figure 5.19: Surface electric field deviations from the mean over 1991 and 1992. There is more variability in the surface electric field measurements than the current density or column resistance due to the coupling of many different processes. The green, orange, and blue dashed lines correspond to the curves in the top plot.

The surface electric field in figure 5.22 has a similar seasonal trend for all latitudes. This trend shows that there are two peaks in the electric field intensity, one peak around January and another in July with reduction in the electric field strength around the equinoxes. This is caused by the significant increase in GEC current during the summer months of 1997. The increased current causes an increased potential and created a well defined seasonal variation in the potential that is mapped into the surface electric field.

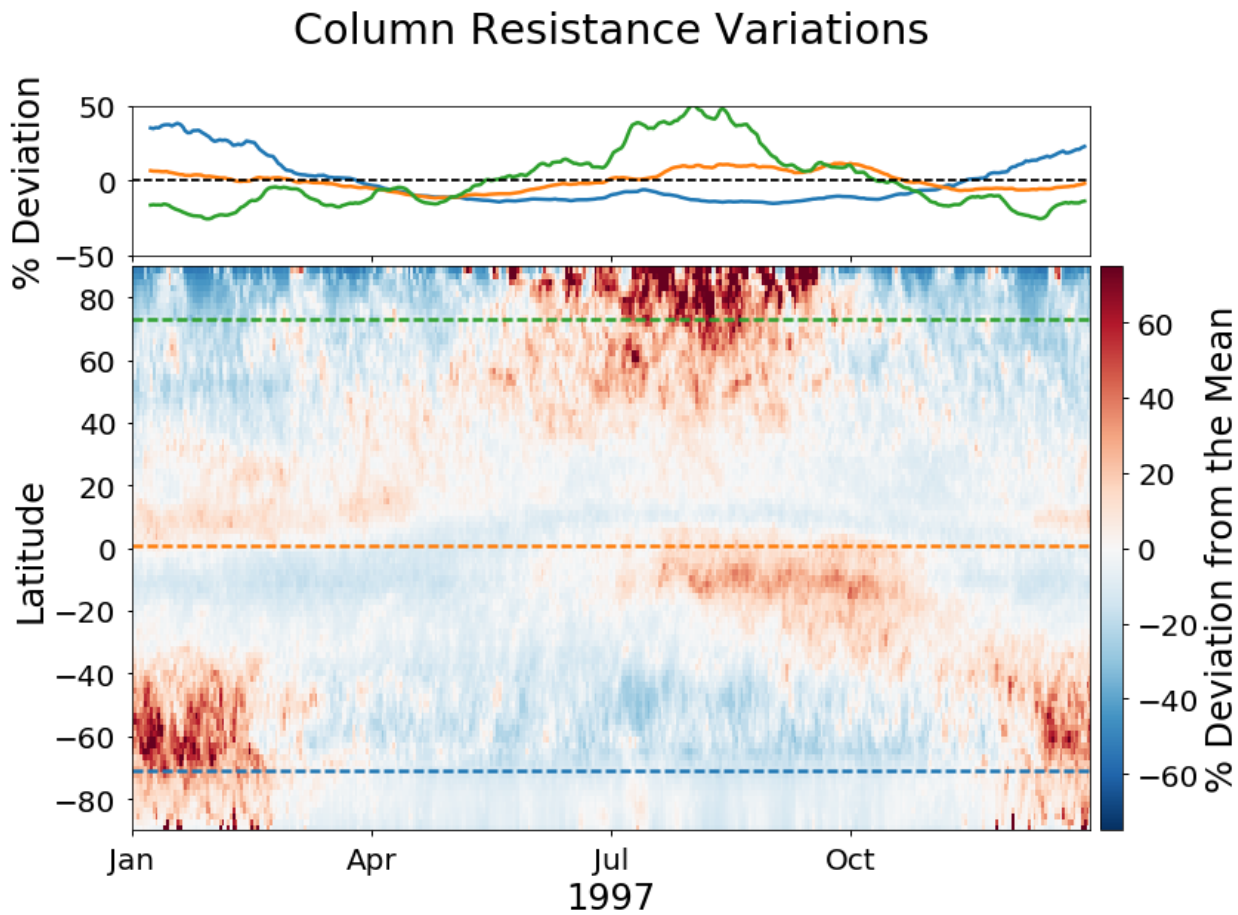


Figure 5.20: Column resistance deviations from the mean over 1997. There is a distinct seasonal trend that is opposite in the northern hemisphere and southern hemisphere. The northern hemisphere has more resistance in the northern hemisphere summer and lower resistances during the northern hemisphere winter. The green, orange, and blue dashed lines correspond to the curves in the top plot.

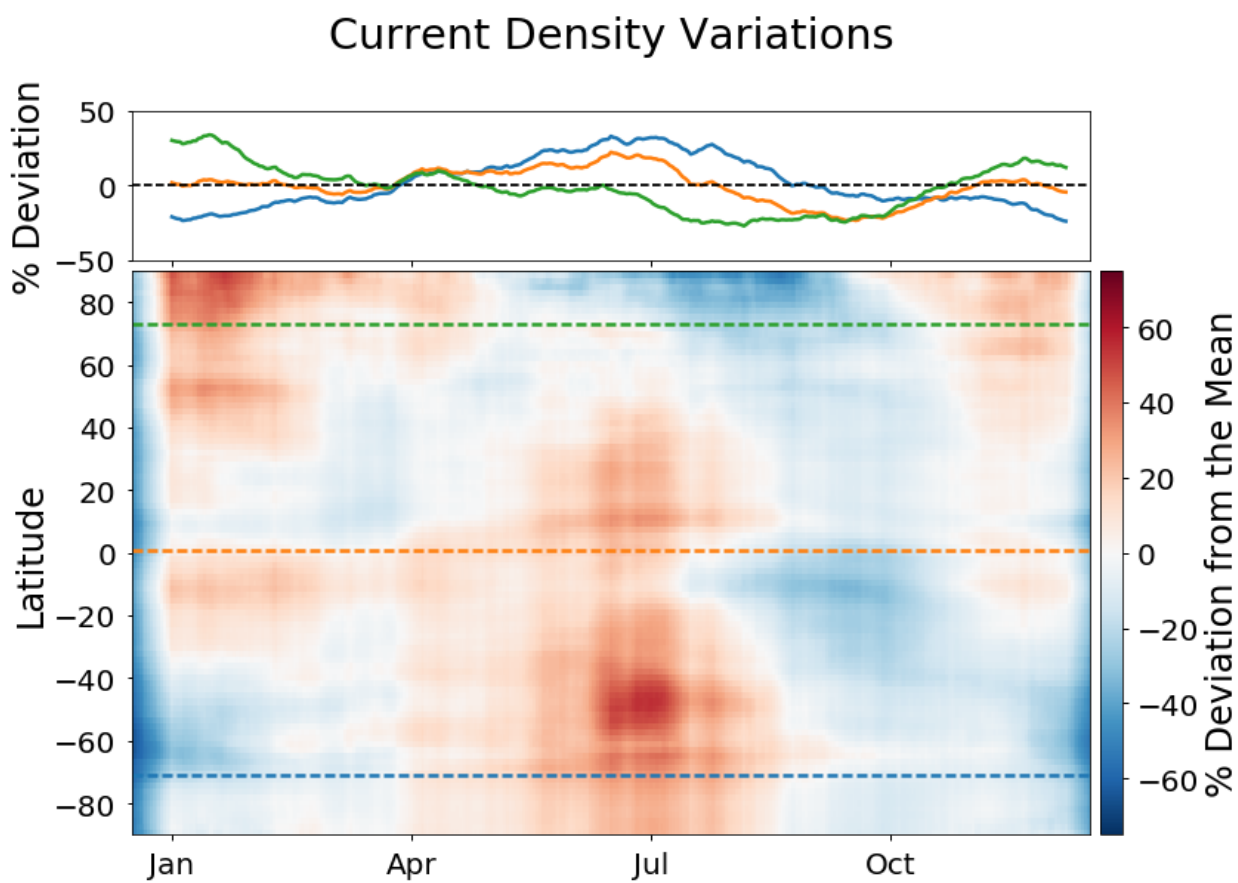


Figure 5.21: Current density deviations from the mean over 1997. There is a distinct seasonal trend that is opposite in the northern hemisphere and southern hemisphere. The current density signal has an inverse signal to the column resistance and also has a seasonal variation from the potential. The green, orange, and blue dashed lines correspond to the curves in the top plot.

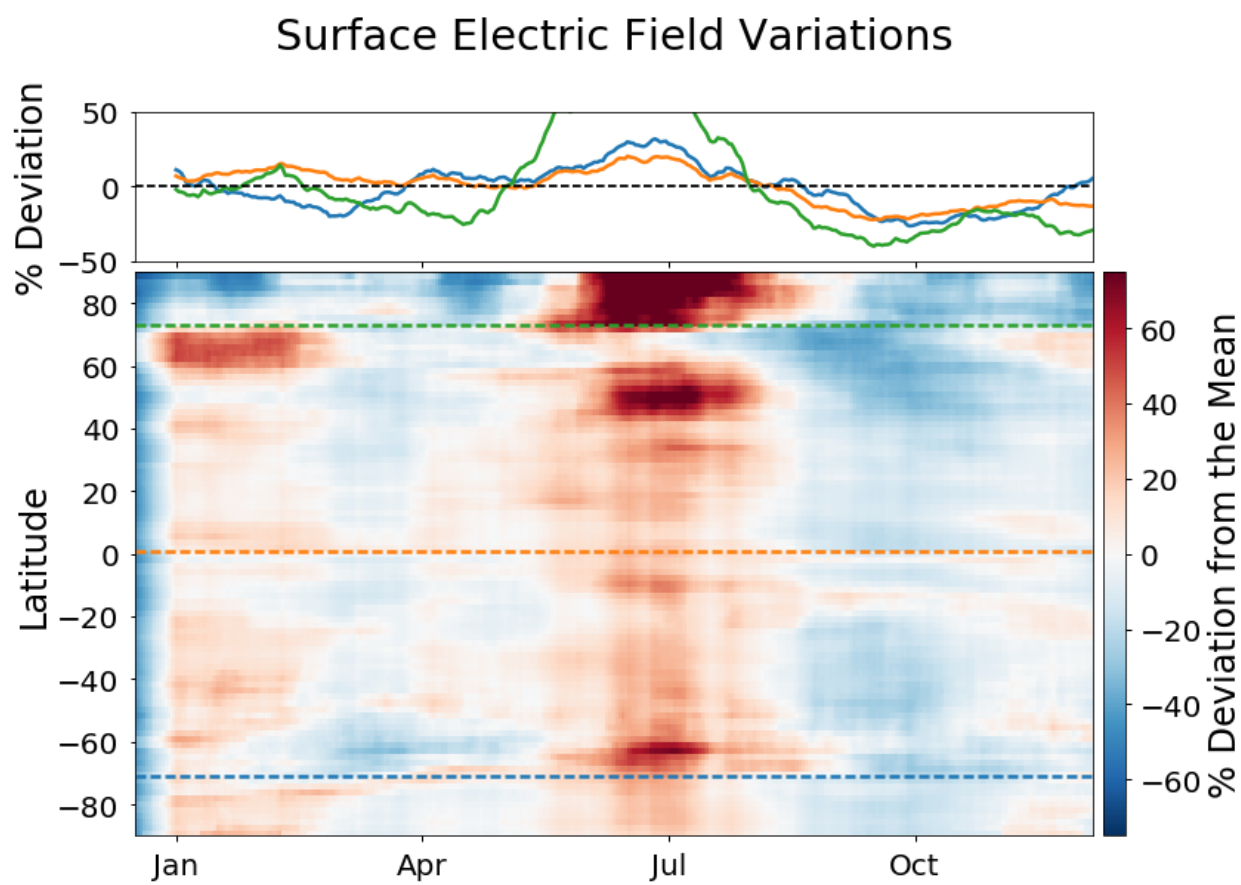


Figure 5.22: Surface electric field deviations from the mean over 1997. There is a strong peak around July at all latitudes, and also another smaller peak in January, with minimums near the equinoxes. The green, orange, and blue dashed lines correspond to the curves in the top plot.

5.7 Summary

Previous chapters described the underlying physics that is incorporated into the newly developed model, WACCM-GEC. This chapter exercised WACCM-GEC to investigate different scenarios within a consistent modeling framework. The incorporation of the magnetospheric current system as a boundary condition that modifies the potential over individual columns was shown to cause a phase-shift in the surface electric fields at high latitude Antarctic stations that agreed with measurements.

The potential within the global electric circuit was shown to vary in-phase with the solar cycle, caused primarily by the increased total resistance within the GEC during solar maximum. Use of a consistent atmospheric model provides a new way to investigate volcanic eruptions. The eruption of Pinatubo was shown to have little influence on the GEC, while a major volcanic eruption 50-times the size of Pinatubo would cause a doubling of total atmospheric resistance. However, these calculations were based on a simple equivalent circuit assumption for determination of variations in the GEC. The use of a sophisticated climate model that incorporates aerosol feedbacks on the dynamics and microphysics in the atmosphere was shown to have a significant impact on GEC properties indirectly by changing the timing of source currents in the atmosphere. This indicates that a physics-based climate model of the atmosphere must be used in future studies to determine what impact different perturbations have on the GEC.

Chapter 6

Conclusions

This thesis investigated the physical understanding of processes in the atmosphere that establish the global electric circuit (GEC). The extensive work within this thesis enhances the community's understanding of both measurements and modeling of atmospheric electric fields. From an observational standpoint, new methods were developed to investigate and utilize an array of electric fields mills. From the modeling standpoint, a comprehensive global electric circuit model was implemented in a community based global climate model that future researchers will be able to utilize and build upon. With the use of these new tools, several unique science findings were discovered and published during the course of the thesis. The thesis addressed the hypothesis by showing that **utilizing an atmospheric physics and dynamics model to represent electric fields and currents within the atmosphere enhances the understanding of electric field measurements.** To address the hypothesis, four specific questions were answered within the thesis.

- (1) **What impact do local meteorological processes have on the measurement of the fair-weather atmospheric electric field?**
- (2) **How does the global conductivity and source distribution influence the local atmospheric electric field measurements?**
- (3) **How does the magnetospheric current system influence atmospheric electric fields in the global electric circuit?**

- (4) What impact do strong conductivity perturbations have on the global electric circuit?

6.1 Major Findings

To address the first question, chapter 2 utilized measurements of the electric field from Kennedy Space Center (KSC) and Antarctica to investigate local electric field measurements. KSC was particularly useful due to the array of field mills within a relatively small region in Florida that has been operating for over 20 years. The data from the array of field mills showed that local meteorology can impact the interpretation of the measurements of electric fields in the lower atmosphere.

When the wind is blowing from the ocean the measured surface electric field is enhanced at field mills close to the coast, while field mills further inland are largely unaffected. Combining the long-term electric field data with METARs observations of cloud cover provided a statistical way of determining the conductivity drop within clouds to be less than a factor of 10. Finally, trends in the data were analyzed with a wavelet analysis to identify a strong diurnal trend, but only a relatively weak annual trend. While investigating the trends within the data, a unique local sunrise feature was identified to strongly correlate with low wind speed and high relative humidity. The work with measurements of atmospheric electric fields showed a strong dependence on local meteorological conditions that were imprinted on the global electric field signatures. With long enough data sets, the local signatures get averaged out and the signature caused by globally generated electric field and currents becomes apparent.

The major advancement of this thesis is the creation of a new physics-based model for the global electric circuit (WACCM-GEC), which addresses the hypothesis and second major question. This model was incorporated into the model framework of the Community Earth System Model. The model computes the 3-D global distribution of electric fields and currents at each model time step of 30 minutes, at a typical grid resolution of 2.5° in longitude by 1.9° in latitude, with 70 vertical levels distributed in modified pressure coordinates.

To calculate the electric fields and currents, WACCM-GEC calculates the evolution of global conductivity at all grid points. Chapter 3 describes in detail the contributions to conductivity and source currents. The conductivity calculations include the generation and loss of ions in the atmosphere. The generation of ions includes galactic cosmic rays, radon, and solar proton events. The loss of ions includes the immediate recombination of ions and attachment to aerosols and cloud droplets. These processes are all represented in the code in a physically consistent manner. The generation of global source currents is described in section 3.2. In the work on incorporating source currents into the model, a significant deviation in the present understanding of source current generation was created. This involved the investigation of the latitudinal distribution of resistance ratios. The long-held assumption of most global current generation occurring near the equator was challenged by their efficiency to make current available to the ionosphere. The model simulations identified stronger storms near the equator were less efficient at producing global currents than storms at higher latitudes. This coupling mechanism spreads the distribution of GEC currents more poleward while remaining peaked at the equator.

With the electrical processes incorporated into the model, the fundamental equations behind the generation of currents and electric fields throughout the atmosphere were developed in chapter 4. The generation of the currents and electric fields across the globe are used to gain an understanding of climatologies and long-term trends. The exact measurement of the fair-weather electric field from surface measurements is very difficult due to local meteorological influences that were described in chapter 2.

The creation of the model enabled the third and fourth questions to be investigated. Detailed descriptions of the findings include magnetospheric coupling into the GEC, volcanic eruptions and solar cycle influences on the GEC, and the seasonal variation of the GEC.

WACCM-GEC reproduced the expected behavior in potential and electric field with UT, as described by the diurnal variation of electric field around the globe. Some discrepancies exist between the relative amplitude of the model's electric field to observations but this is expected to improve as the source current modeling improves over time. At high latitudes, the influence

of the external current systems was demonstrated and significant regional perturbations can be introduced to the GEC potential distribution depending on the magnitude of the geomagnetic activity and the relative phase of the externally and internally generated potentials with UT. The high-latitude influence of magnetospheric potentials was evaluated against two separate Antarctic sites (Vostok and Concordia) where electric field mills have been deployed and extensively utilized and scrutinized. WACCM-GEC was able to generate a diurnal curve of the relative electric field variation at these locations that was in good qualitative agreement with the data. To determine the validity of the magnetospheric potential pattern, electric field data from Vostok were shown to have a phase shift relative to Concordia, and the model was able to reproduce this phase shift. More data sets at high-latitude locations are needed to discern the influence of the magnetospheric potential on the GEC potential.

Volcanic eruptions were investigated with the modeling of the Pinatubo eruption in June 1991. Section 5.5 showed how the explosive eruption emits aerosols into the stratosphere that last for months and are transported with the circulation patterns inherently present in the global climate model. The incorporation of aerosols in the stratosphere was shown to have an insignificant affect on the magnitude of the total resistance but did appear to make the total resistance peak earlier than without the volcano present. The lack of effect on the total resistance is due to the aerosols being concentrated in the stratosphere where there is less than a 10% contribution to the total atmospheric resistance.

The contribution current to the GEC was investigated after volcanic eruptions and found to be peak earlier after the volcanic eruption as well. This led to a slightly higher GEC potential after the eruption that peaked earlier in time than without the eruption. With larger volcanic aerosol loading in the atmosphere the magnitude of changes would be larger and more evident relative to the background variations. There are complications on the interpretation of the aerosol loading causing these influences as the aerosols also impact the microphysical properties of the atmosphere and cloud development processes that also indirectly influence the GEC.

The GEC has been proposed as a mechanism for measuring solar influences on climate. The GEC has been theorized to vary both in-phase and out-of-phase with the solar cycle by previous authors. The ambiguity is due to the unique coupling of total resistance variations and source current production, which are anti-correlated with each other. WACCM-GEC was run over years of solar maximum and minimum which showed a 20Ω variation in the total resistance. Over the same runs the current had significant seasonal variability that was stronger than any variations from the solar cycle. The ambiguity caused by the source currents differing during the two years were eliminated by investigating a single year and only modifying the GCR ionization rate between solar minimum and maximum. This showed that the GEC varies in-phase with the solar cycle, with variations of the ionospheric potential of around 10% between solar minimum and maximum conditions.

Finally, the seasonal variations of the GEC were investigated in section 5.6. There were again many discussions found on different variations of the measured GEC properties with season. The model was able to investigate the seasonal variations and provide explanations for the discrepancies between the different observations. The model showed that there is a significant seasonal variation in the column resistance. Furthermore, this seasonal variation is dependent on the measurement's latitude. Southern and northern latitudes were found to vary out of phase with one another. This meant that observers measuring GEC properties in high northern latitudes would see a different seasonal cycle than observers in the southern hemisphere due to the seasonal variation in overhead column resistance.

6.2 Future Advancements

These results represent fundamental advances in the understanding of the physical representation of electric fields in the atmosphere. The model was developed with the community in mind and the hope that future researchers will utilize it for their investigations into other electric phenomena in the atmosphere. Another major utility of this work is the ability to evaluate the performance of new atmospheric physics schemes by contrasting the model outcomes of GEC prop-

erties with expected GEC behavior. This was elucidated when investigating the convective mass flux parametrization for source currents and observing the diurnal variation in the GEC electric field was peaking too early. This is attributed to a known limitation in CESM(WACCM) and its convection scheme, where convection starts too early. To determine whether a new convection scheme is an improvement, one could compare the GEC electric-field UT response of the two different schemes.

There are presently no feedback mechanisms implemented in WACCM-GEC to determine how the electric fields in the atmosphere could impact climate variables. Many feedback mechanisms between the electrical properties of the atmosphere and cloud microphysics have been proposed, and this model could be used to investigate some of these relationships self-consistently.

The source currents appear to be the limiting factor for obtaining realistic representations of the currents and electric fields. Further investigation into the microphysical details of convection and charge separation would lead to better representations within the models. Currently, most observations focus on measurements of lightning and highly electrified clouds. The incorporation of an efficiency factor for calculating the contribution current to the GEC was found to shift the distribution of GEC currents towards higher latitudes. This warrants further investigation of the differences between the strengths of storms and the amount of current that gets distributed globally.

Bibliography

Ackermann, M., Ajello, M., Allafort, A., Baldini, L., Ballet, J., Barbiellini, G., Baring, M. G., Bastieri, D., Bechtol, K., Bellazzini, R., Blandford, R. D., Bloom, E. D., Bonamente, E., Borgland, A. W., Bottacini, E., Brandt, T. J., Bregeon, J., Brigida, M., Bruel, P., Buehler, R., Busetto, G., Buson, S., Caliandro, G. A., Cameron, R. A., Caraveo, P. A., Casandjian, J. M., Cecchi, C., Celik, O., Charles, E., Chaty, S., Chaves, R. C. G., Chekhtman, A., Cheung, C. C., Chiang, J., Chiaro, G., Cillis, A. N., Ciprini, S., Claus, R., Cohen-Tanugi, J., Cominsky, L. R., Conrad, J., Corbel, S., Cutini, S., D'Ammando, F., de Angelis, A., de Palma, F., Dermer, C. D., do Couto e Silva, E., Drell, P. S., Drlica-Wagner, A., Falletti, L., Favuzzi, C., Ferrara, E. C., Franckowiak, A., Fukazawa, Y., Funk, S., Fusco, P., Gargano, F., Germani, S., Giglietto, N., Giommi, P., Giordano, F., Giroletti, M., Glanzman, T., Godfrey, G., Grenier, I. A., Grondin, M.-H., Grove, J. E., Guiriec, S., Hadasch, D., Hanabata, Y., Harding, A. K., Hayashida, M., Hayashi, K., Hays, E., Hewitt, J. W., Hill, A. B., Hughes, R. E., Jackson, M. S., Jogler, T., Jóhannesson, G., Johnson, A. S., Kamae, T., Kataoka, J., Katsuta, J., Knöldlseder, J., Kuss, M., Lande, J., Larsson, S., Latronico, L., Lemoine-Goumard, M., Longo, F., Loparco, F., Lovellette, M. N., Lubrano, P., Madejski, G. M., Massaro, F., Mayer, M., Mazziotta, M. N., McEnery, J. E., Mehault, J., Michelson, P. F., Mignani, R. P., Mitthumsiri, W., Mizuno, T., Moiseev, A. A., Monzani, M. E., Morselli, A., Moskalenko, I. V., Murgia, S., Nakamori, T., Nemmen, R., Nuss, E., Ohno, M., Ohsugi, T., Omodei, N., Orienti, M., Orlando, E., Ormes, J. F., Paneque, D., Perkins, J. S., Pesce-Rollins, M., Piron, F., Pivato, G., Rainò, S., Rando, R., Razzano, M., Razzaque, S., Reimer, A., Reimer, O., Ritz, S., Romoli, C., Sánchez-Conde, M., Schulz, A., Sgrò, C., Simeon, P. E., Siskind, E. J., Smith, D. A., Spandre, G., Spinelli, P., Stecker, F. W., Strong, A. W., Suson, D. J., Tajima, H., Takahashi, H., Takahashi, T., Tanaka, T., Thayer, J. G., Thayer, J. B., Thompson, D. J., Thorsett, S. E., Tibaldo, L., Tibolla, O., Tinivella, M., Troja, E., Uchiyama, Y., Usher, T. L., Vandenbroucke, J., Vasileiou, V., Vianello, G., Vitale, V., Waite, A. P., Werner, M., Winer, B. L., Wood, K. S., Wood, M., Yamazaki, R., Yang, Z., and Zimmer, S. (2013). Detection of the Characteristic Pion-Decay Signature in Supernova Remnants. *Science*, 339:807–811.

Bates, D. R. (1982). Ion-ion recombination in an ambient ion gas. *Journal of Physics B: Atomic and Molecular Physics*, 15(20):L755.

Baumgaertner, A. J. G., Lucas, G. M., Thayer, J. P., and Mallios, S. A. (2014). On the role of clouds in the fair weather part of the global electric circuit. *Atmos. Chem. Phys.*, 14(16):8599–8610.

Baumgaertner, A. J. G., Thayer, J. P., Neely, R. R., and Lucas, G. (2013). Toward a comprehensive global electric circuit model: Atmospheric conductivity and its variability in CESM1(WACCM) model simulations. *J. Geophys. Res.*, 118(16):9221–9232.

- Bayona, V., Flyer, N., Lucas, G. M., and Baumgaertner, A. J. G. (2015). A 3-D RBF-FD solver for modeling the atmospheric global electric circuit with topography (GEC-RBFFD v1.0). *Geosci. Model Dev.*, 8(10):3007–3020.
- Bazilevskaya, G. A., Usoskin, I. G., Flückiger, E. O., Harrison, R. G., Desorgher, L., Bütkofer, R., Krainev, M. B., Makhmutov, V. S., Stozhkov, Y. I., Svirzhevskaya, A. K., Svirzhevsky, N. S., and Kovaltsov, G. A. (2008). Cosmic Ray Induced Ion Production in the Atmosphere. *Space Science Reviews*, 137(1-4):149–173.
- Bennett, A. J. and Harrison, R. G. (2009). Evidence for global circuit current flow through water droplet layers. *Journal of Atmospheric and Solar-Terrestrial Physics*, 71(12):1219–1221.
- Blakeslee, R. J. and Krider, E. P. (1992). Ground level measurements of air conductivities under Florida thunderstorms. *Journal of Geophysical Research: Atmospheres*, 97(D12):12947–12951.
- Blakeslee, R. J., Mach, D. M., Bateman, M. G., and Bailey, J. C. (2012). Seasonal variations in the lightning diurnal cycle and implications for the global electric circuit. *Atmos. Res.*, 72(0):376–381.
- Blakeslee, R. J., Mach, D. M., Bateman, M. G., and Bailey, J. C. (2014). Seasonal variations in the lightning diurnal cycle and implications for the global electric circuit. *Atmospheric Research*, 135–136:228–243.
- Blanchard, D. C. (1966). Positive Space Charge from the Sea. *Journal of the Atmospheric Sciences*, 23(5):507–515.
- Burns, G. B. (2005). Interannual consistency of bi-monthly differences in diurnal variations of the ground-level, vertical electric field. *Journal of Geophysical Research*, 110(D10).
- Burns, G. B., Tinsley, B. A., Frank-Kamenetsky, A. V., Troshichev, O. A., French, W. J. R., and Klekociuk, A. R. (2012). Monthly Diurnal Global Atmospheric Circuit Estimates Derived from Vostok Electric Field Measurements Adjusted for Local Meteorological and Solar Wind Influences. *Journal of the Atmospheric Sciences*, 69(6):2061–2082.
- Burns, G. B., Tinsley, B. A., French, W. J. R., Troshichev, O. A., and Frank-Kamenetsky, A. V. (2008). Atmospheric circuit influences on ground-level pressure in the Antarctic and Arctic. *Journal of Geophysical Research*, 113(D15).
- Chalmers, J. A. (1957). *Atmospheric Electricity*. Pergamon Press. Google-Books-ID: sZV6AAAAIAAJ.
- Conen, F. and Robertson, L. B. (2002). Latitudinal distribution of radon-222 flux from continents. *Tellus B*, 54(2):127–133.
- Corney, R. C., Burns, G. B., Michael, K., Frank-Kamenetsky, A. V., Troshichev, O. A., Bering, E. A., Papitashvili, V. O., Breed, A. M., and Duldig, M. L. (2003). The influence of polar-cap convection on the geoelectric field at Vostok, Antarctica. *J. Atmos. Sol-Terr. Phys.*, 65:345–354.
- Crozier, W. D. (1969). Direct measurement of radon-220 (thoron) exhalation from the ground. *Journal of Geophysical Research*, 74(17):4199–4205.
- Dejnakintra, M. and Park, C. G. (1974). Lightning-induced electric fields in the ionosphere. *Journal of Geophysical Research*, 79(13):1903–1910.

- Funke, B., Baumgaertner, A., Calisto, M., Egorova, T., Jackman, C. H., Kieser, J., Krivolutsky, A., López-Puertas, M., Marsh, D. R., Reddmann, T., Rozanov, E., Salmi, S.-M., Sinnhuber, M., Stiller, G. P., Verronen, P. T., Versick, S., von Clarmann, T., Vyushkova, T. Y., Wieters, N., and Wissing, J. M. (2011). Composition changes after the "Halloween" solar proton event: The High Energy Particle Precipitation in the Atmosphere (HEPPA) model versus MIPAS data intercomparison study. *Atmos. Chem. Phys.*, 11:9089–9139.
- Gathman, S. G. and Hoppel, W. A. (1970). Electrification processes over Lake Superior. *Journal of Geophysical Research*, 75(6):1041–1048.
- Gettelman, A., Morrison, H., Santos, S., Bogenschutz, P., and Caldwell, P. M. (2014). Advanced Two-Moment Bulk Microphysics for Global Models. Part II: Global Model Solutions and Aerosol–Cloud Interactions. *Journal of Climate*, 28(3):1288–1307.
- Gettelman, A., Morrison, H., Terai, C. R., and Wood, R. (2013). Microphysical process rates and global aerosol–cloud interactions. *Atmos. Chem. Phys.*, 13(19):9855–9867.
- Harrison, R. G. (2003). Ion-aerosol-cloud processes in the lower atmosphere. *Reviews of Geophysics*, 41(3).
- Harrison, R. G. (2013). The Carnegie Curve. *Surveys in Geophysics*, 34(2):209–232.
- Hays, P. B. and Roble, R. G. (1979). A quasi-static model of global atmospheric electricity. I - The lower atmosphere. *J. Geophys. Res.*, 84:3291–3305.
- Herbst, K., Kopp, A., and Heber, B. (2013). Influence of the terrestrial magnetic field geometry on the cutoff rigidity of cosmic ray particles. *Ann. Geophys.*, 31(10):1637–1643.
- Hoppel, W. A. (1985). Ion-aerosol attachment coefficients, ion depletion, and the charge distribution on aerosols. *Journal of Geophysical Research: Atmospheres (1984–2012)*, 90(D4):5917–5923.
- Hoppel, W. A., Anderson, R. V., and Willett, J. C. (1986). Atmospheric electricity in the planetary boundary layer. In *The Earth's Electrical Environment*. Natl. Acad. Press, Washington, D. C.
- Hoppel, W. A. and Gathman, S. G. (1971). Determination of eddy diffusion coefficients from atmospheric electrical measurements. *Journal of Geophysical Research*, 76(6):1467–1477.
- Israël, H. (1970). *Atmospheric electricity: (Atmosphärische Elektrizität)*. Number v. 29 in Probleme der kosmischen Physik. Israel Program for Scientific Translations [available from the U.S. Dept. of Commerce, National Technical Information Service, Springfield, Va.], Jerusalem.
- Jackman, C. H., Marsh, D. R., Vitt, F. M., Garcia, R. R., Fleming, E. L., Labow, G. J., Randall, C. E., López-Puertas, M., Funke, B., von Clarmann, T., and Stiller, G. P. (2008). Short- and medium-term atmospheric constituent effects of very large solar proton events. *Atmos. Chem. Phys.*, 8:765–785.
- Jackman, C. H. and McPeters, R. D. (2004). Solar Variability and its Effects on Climate. *Geophysical Monograph*, 141:305–319.
- Kalb, C., Deierling, W., Baumgaertner, A., Peterson, M., Liu, C., and Mach, D. (2016). Parameterizing total storm conduction currents in the Community Earth System Model. *Journal of Geophysical Research: Atmospheres*, 121(22):2016JD025376.

- Kalinin, A. V., Slyunyaev, N. N., Mareev, E. A., and Zhidkov, A. A. (2014). Stationary and nonstationary models of the global electric circuit: Well-posedness, analytical relations, and numerical implementation. *Izvestiya, Atmospheric and Oceanic Physics*, 50(3):314–322.
- Kraakevik, J. H. (1961). Measurements of current density in the fair weather atmosphere. *Journal of Geophysical Research*, 66(11):3735–3748.
- Liu, C., Williams, E. R., Zipser, E. J., and Burns, G. (2010a). Diurnal Variations of Global Thunderstorms and Electrified Shower Clouds and Their Contribution to the Global Electrical Circuit. *Journal of the Atmospheric Sciences*, 67(2):309–323.
- Liu, H.-L., Foster, B. T., Hagan, M. E., McInerney, J. M., Maute, A., Qian, L., Richmond, A. D., Roble, R. G., Solomon, S. C., Garcia, R. R., Kinnison, D., Marsh, D. R., Smith, A. K., Richter, J., Sassi, F., and Oberheide, J. (2010b). Thermosphere extension of the Whole Atmosphere Community Climate Model. *J. Geophys. Res.*, 115(a14):A12302.
- Liu, X., Ma, P.-L., Wang, H., Tilmes, S., Singh, B., Easter, R. C., Ghan, S. J., and Rasch, P. J. (2016). Description and evaluation of a new four-mode version of the Modal Aerosol Module (MAM4) within version 5.3 of the Community Atmosphere Model. *Geosci. Model Dev.*, 9(2):505–522.
- Liu, Y., San Liang, X., and Weisberg, R. H. (2007). Rectification of the Bias in the Wavelet Power Spectrum. *Journal of Atmospheric and Oceanic Technology*, 24(12):2093–2102.
- Logg, A., Mardal, K.-A., Wells, G. N., and others (2012). *Automated Solution of Differential Equations by the Finite Element Method*. Springer.
- Lucas, G. M., Baumgaertner, A. J. G., and Thayer, J. P. (2015). A global electric circuit model within a community climate model. *Journal of Geophysical Research: Atmospheres*, page 2015JD023562.
- Lucas, G. M., Thayer, J. P., and Deierling, W. (2017). Statistical analysis of spatial and temporal variations in atmospheric electric fields from a regional array of field mills. *Journal of Geophysical Research: Atmospheres*, page 2016JD025944.
- MacGorman, D. R. and Rust, W. D. (1998). *The Electrical Nature of Storms*. Oxford University Press, New York.
- Mach, D. M., Blakeslee, R. J., and Bateman, M. G. (2011). Global electric circuit implications of combined aircraft storm electric current measurements and satellite-based diurnal lightning statistics. *Journal of Geophysical Research*, 116(D5).
- Mach, D. M., Blakeslee, R. J., Bateman, M. G., and Bailey, J. C. (2009). Electric fields, conductivity, and estimated currents from aircraft overflights of electrified clouds. *Journal of Geophysical Research*, 114(D10).
- Mach, D. M., Blakeslee, R. J., Bateman, M. G., and Bailey, J. C. (2010). Comparisons of total currents based on storm location, polarity, and flash rates derived from high-altitude aircraft overflights. *Journal of Geophysical Research*, 115(D3).
- Mareev, E. A. and Volodin, E. M. (2014). Variation of the global electric circuit and Ionospheric potential in a general circulation model. *Geophysical Research Letters*, 41(24):2014GL062352.

- Markson, R. (1975). Atmospheric Electrical Detection of Organized Convection. *Science*, 188(4194):1171–1177.
- Markson, R. (1978). Solar modulation of atmospheric electrification and possible implications for the Sun-weather relationship. *Nature*, 273:103–109.
- Markson, R. (2007). The Global Circuit Intensity: Its Measurement and Variation over the Last 50 Years. *Bulletin of the American Meteorological Society*, 88(2):223–241.
- Markson, R. and Muir, M. (1980). Solar wind control of the Earth's electric field. *Science*, 208(4447):979–990.
- Markson, R., Sedláček, J., and Fairall, C. W. (1981). Turbulent transport of electric charge in the marine atmospheric boundary layer. *Journal of Geophysical Research: Oceans*, 86(C12):12115–12121.
- Marshall, T. C., Rust, W. D., Stolzenburg, M., Roeder, W. P., and Krehbiel, P. R. (1999). A study of enhanced fair-weather electric fields occurring soon after sunrise. *Journal of Geophysical Research: Atmospheres*, 104(D20):24455–24469.
- Martin, G. M., Johnson, D. W., and Spice (1994). The Measurement and Parameterization of Effective Radius of Droplets in Warm Stratocumulus Clouds. *Journal of the Atmospheric Sciences*, 51(13):1823–1842.
- Matthes, K., Funke, B., Anderson, M. E., Barnard, L., Beer, J., Charbonneau, P., Clilverd, M. A., Dudok de Wit, T., Haberreiter, M., Hendry, A., Jackman, C. H., Kretschmar, M., Kruschke, T., Kunze, M., Langematz, U., Marsh, D. R., Maycock, A., Misios, S., Rodger, C. J., Scaife, A. A., Seppälä, A., Shangguan, M., Sinnhuber, M., Tourpali, K., Usoskin, I., van de Kamp, M., Verronen, P. T., and Versick, S. (2016). Solar Forcing for CMIP6 (v3.1). *Geosci. Model Dev. Discuss.*, 2016:1–82.
- Mills, M. J., Schmidt, A., Easter, R., Solomon, S., Kinnison, D. E., Ghan, S. J., Neely, R. R., Marsh, D. R., Conley, A., Bardeen, C. G., and Gettelman, A. (2016). Global volcanic aerosol properties derived from emissions, 1990–2014, using CESM1(WACCM). *Journal of Geophysical Research: Atmospheres*, 121(5):2015JD024290.
- Morrison, H. and Gettelman, A. (2008). A New Two-Moment Bulk Stratiform Cloud Microphysics Scheme in the Community Atmosphere Model, Version 3 (CAM3). Part I: Description and Numerical Tests. *J. Climate*, 21:3642.
- Neely III, R. R., Conley, A. J., Vitt, F., and Lamarque, J.-F. (2016). A consistent prescription of stratospheric aerosol for both radiation and chemistry in the Community Earth System Model (CESM1). *Geosci. Model Dev.*, 9(7):2459–2470.
- Nicoll, K. A. (2012). Measurements of Atmospheric Electricity Aloft. *Surveys in Geophysics*, 33(5):991–1057.
- Nicoll, K. A. and Harrison, R. G. (2010). Experimental determination of layer cloud edge charging from cosmic ray ionisation: DETERMINATION OF CLOUD EDGE CHARGING. *Geophysical Research Letters*, 37(13):n/a–n/a.

- Nicoll, K. A. and Harrison, R. G. (2016). Stratiform cloud electrification: Comparison of theory with multiple in-cloud measurements. *Quarterly Journal of the Royal Meteorological Society*, 142(700):2679–2691.
- Odzimek, A., Lester, M., and Kubicki, M. (2010). EGATEC: A new high-resolution engineering model of the global atmospheric electric circuit—Currents in the lower atmosphere. *Journal of Geophysical Research*, 115(D18).
- Park, C. G. (1976). Downward mapping of high-latitude ionospheric electric fields to the ground. *Journal of Geophysical Research*, 81(1):168–174.
- Pruppacher, H. R. and Klett, J. D. (1997). *Microphysics of Clouds and Precipitation*. Kluwer, 2nd edition.
- Reddell, B. D., Benbrook, J. R., Bering, E. A., Cleary, E. N., and Few, A. A. (2004). Seasonal variations of atmospheric electricity measured at Amundsen-Scott South Pole Station. *Journal of Geophysical Research: Space Physics*, 109(A9):A09308.
- Richmond, A. D. (1995). Ionospheric Electrodynamics Using Magnetic Apex Coordinates. *Journal of geomagnetism and geoelectricity*, 47(2):191–212.
- Richmond, A. D., Blanc, M., Emery, B. A., Wand, R. H., Fejer, B. G., Woodman, R. F., Ganguly, S., Amayenc, P., Behnke, R. A., Calderon, C., and Evans, J. V. (1980). An empirical model of quiet-day ionospheric electric fields at middle and low latitudes. *Journal of Geophysical Research: Space Physics*, 85(A9):4658–4664.
- Roble, R. G. and Hays, P. B. (1979a). Electrical Coupling Between the Upper and Lower Atmosphere. In McCormac, B. M. and Seliga, T. A., editors, *Solar-Terrestrial Influences on Weather and Climate*, page 233.
- Roble, R. G. and Hays, P. B. (1979b). A quasi-static model of global atmospheric electricity. II - Electrical coupling between the upper and lower atmosphere. *J. Geophys. Res.*, 84:7247–7256.
- Rycroft, M. J., Harrison, R. G., Nicoll, K. A., and Mareev, E. A. (2008). An Overview of Earth's Global Electric Circuit and Atmospheric Conductivity. *Space Science Reviews*, 137(1-4):83–105.
- Saunders, C. (2008). Charge Separation Mechanisms in Clouds. *Space Science Reviews*, 137(1-4):335–353.
- Schery, S. D. and Wasiolek, M. A. (1998). Modelling radon flux from the earth's surface. In: Radon and Thoron in the Human Environment. *World Scientific Publishing*.
- Silva, H. G., Conceição, R., Wright, M. D., Matthews, J. C., Pereira, S. N., and Shallcross, D. E. (2015). Aerosol Hygroscopic growth and the dependence of atmospheric electric field measurements with relative Humidity. *Journal of Aerosol Science*.
- Slyunyaev, N. N., Mareev, E. A., and Zhidkov, A. A. (2015). On the variation of the ionospheric potential due to large-scale radioactivity enhancement and solar activity. *Journal of Geophysical Research: Space Physics*, 120(8):2015JA021039.
- Takahashi, T. and Miyawaki, K. (2002). Reexamination of Rimming Electrification in a Wind Tunnel. *Journal of the Atmospheric Sciences*, 59(5):1018–1025.

- Timmreck, C. (2012). Modeling the climatic effects of large explosive volcanic eruptions. *Wiley Interdisciplinary Reviews: Climate Change*, 3(6):545–564.
- Tinsley, B. A. (1996). Correlations of atmospheric dynamics with solar wind-induced changes of air-Earth current density into cloud tops. *J. Geophys. Res.*, 101:29701.
- Tinsley, B. A. (2010). Electric charge modulation of aerosol scavenging in clouds: Rate coefficients with Monte Carlo simulation of diffusion. *J. Geophys. Res.*, 115(D14):23211.
- Tinsley, B. A., Hoeksema, J. T., and Baker, D. N. (1994). Stratospheric volcanic aerosols and changes in air-earth current density at solar wind magnetic sector boundaries as conditions for the Wilcox tropospheric vorticity effect. *J. Geophys. Res.*, 99:16805.
- Tinsley, B. A. and Yu, F. (2004). Atmospheric Ionization and Clouds as Links Between Solar Activity and Climate. In Pap, J. M., Fox, P., Frohlich, C., Hudson, H. S., Kuhn, J., McCormack, J., North, G., Sprigg, W., and Wu, S. T., editors, *Solar Variability and Its Effects on Climate. Geophysical Monograph 141*, volume 141 of *Washington DC American Geophysical Union Geophysical Monograph Series*, page 321.
- Tinsley, B. A. and Zhou, L. (2006). Initial results of a global circuit model with variable stratospheric and tropospheric aerosols. *J. Geophys. Res.*, 111(D10):16205.
- Toon, O. B., Turco, R. P., Hamill, P., Kiang, C. S., and Whitten, R. C. (1979). A One-Dimensional Model Describing Aerosol Formation and Evolution in the Stratosphere: II. Sensitivity Studies and Comparison with Observations. *J. Atmos. Sci.*, 36:718–736.
- Toon, O. B., Turco, R. P., Westphal, D., Malone, R., and Liu, M. S. (1988). A multidimensional model for aerosols - Description of computational analogs. *J. Atmos. Sci.*, 45:2123–2143.
- Torrence, C. and Compo, G. P. (1998). A Practical Guide to Wavelet Analysis. *Bulletin of the American Meteorological Society*, 79:61–78.
- Turco, R. P., Hamill, P., Toon, O. B., Whitten, R. C., and Kiang, C. S. (1979). A One-Dimensional Model Describing Aerosol Formation and Evolution in the Stratosphere: I. Physical Processes and Mathematical Analogs. *J. Atmos. Sci.*, 36:699–717.
- Tzur, I. and Roble, R. G. (1985). The interaction of a dipolar thunderstorm with its global electrical environment. *J. Geophys. Res.*, 90:5989–5999.
- Usoskin, I. G., Alanko-Huotari, K., Kovaltsov, G. A., and Mursula, K. (2005). Heliospheric modulation of cosmic rays: Monthly reconstruction for 1951-2004. *J. Geophys. Res.*, 110(a9):12108.
- Weimer, D. R. (1995). Models of high-latitude electric potentials derived with a least error fit of spherical harmonic coefficients. *Journal of Geophysical Research: Space Physics*, 100(A10):19595–19607.
- Whipple, F. J. W. (1938). Modern views on atmospheric electricity. *Quarterly Journal of the Royal Meteorological Society*, 64(275):199–222.
- Willett, J. (1985). Atmospheric-electrical implications of ^{222}Rn daughter deposition on vegetated ground. *Journal of Geophysical Research: Atmospheres*, 90(D4):5901–5908.

- Williams, E. and Mareev, E. (2014). Recent progress on the global electrical circuit. *Atmospheric Research*, 135–136:208–227.
- Wilson, C. T. R. (1921). Investigations on Lightning Discharges and on the Electric Field of Thunderstorms. *Philosophical Transactions of the Royal Society of London A: Mathematical, Physical and Engineering Sciences*, 221(582-593):73–115.
- Wissing, J. M. and Kallenrode, M.-B. (2009). Atmospheric Ionization Module Osnabrück (AIMOS): A 3-D model to determine atmospheric ionization by energetic charged particles from different populations. *J. Geophys. Res.*, 114(a13):6104.
- Yaniv, R., Yair, Y., Price, C., and Katz, S. (2016). Local and global impacts on the fair-weather electric field in Israel. *Atmospheric Research*, 172–173:119–125.
- Zhang (1995). Sensitivity of climate simulations to the parameterization of cumulus convection in the Canadian climate centre general circulation model. *Atmosphere-Ocean*, 33:407–446.
- Zhou, L. and Tinsley, B. A. (2010). Global Circuit Model with Clouds. *J. Atmos. Sci.*, 67:1143–1156.